

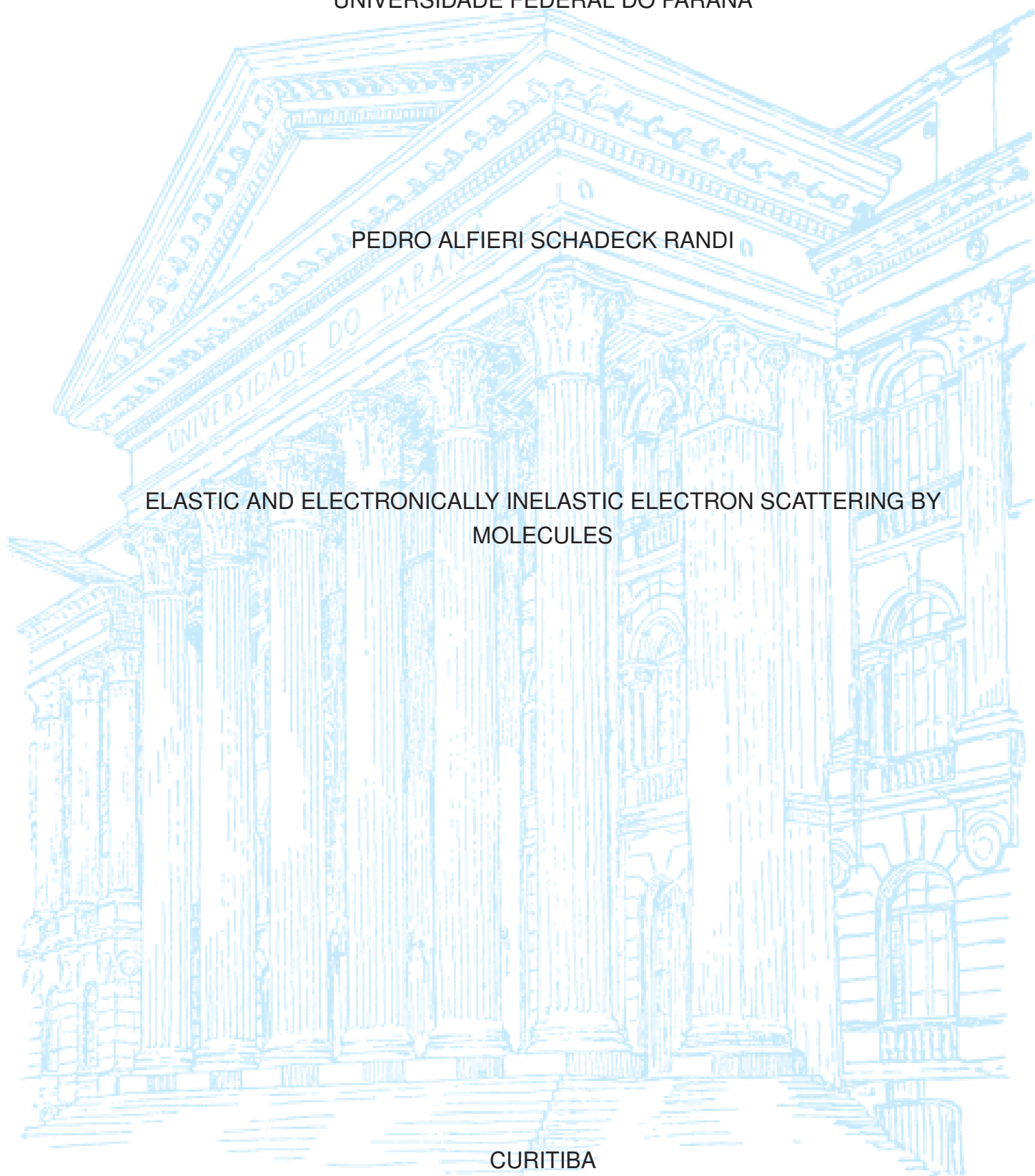
UNIVERSIDADE FEDERAL DO PARANÁ

PEDRO ALFIERI SCHADECK RANDI

ELASTIC AND ELECTRONICALLY INELASTIC ELECTRON SCATTERING BY
MOLECULES

CURITIBA

2024



PEDRO ALFIERI SCHADECK RANDI

ELASTIC AND ELECTRONICALLY INELASTIC ELECTRON SCATTERING BY
MOLECULES

Dissertação apresentada ao Programa de Pós-Graduação em Física do Setor de Ciências Exatas da Universidade Federal do Paraná como requisito parcial para a obtenção de título de Mestre em Física.

Supervisor: Professor Doutor Márcio Henrique Franco Bettega.

CURITIBA

2024

DADOS INTERNACIONAIS DE CATALOGAÇÃO NA PUBLICAÇÃO (CIP)
UNIVERSIDADE FEDERAL DO PARANÁ
SISTEMA DE BIBLIOTECAS – BIBLIOTECA DE CIÊNCIA E TECNOLOGIA

Randi, Pedro Alfieri Schadeck

Elastic and electronically inelastic electron scattering by molecules / Pedro Alfieri Schadeck Randi. – Curitiba, 2024.

1 recurso on-line : PDF.

Dissertação (Mestrado) - Universidade Federal do Paraná, Setor de Ciências Exatas, Programa de Pós-Graduação em Física.

Orientador: Márcio Henrique Franco Bettega

1. Elétrons – Espalhamento. 2. Excitação eletrônica. 3. Seção de choque.
I. Universidade Federal do Paraná. II. Programa de Pós-Graduação em Física. III. Bettega, Márcio Henrique Franco. IV. Título.

TERMO DE APROVAÇÃO

Os membros da Banca Examinadora designada pelo Colegiado do Programa de Pós-Graduação FÍSICA da Universidade Federal do Paraná foram convocados para realizar a arguição da Dissertação de Mestrado de **PEDRO ALFIERI SCHADECK RANDI** intitulada: "**Elastic and electronically inelastic electron scattering by molecules**", sob orientação do Prof. Dr. MARCIO HENRIQUE FRANCO BETTEGA, que após terem inquirido o aluno e realizada a avaliação do trabalho, são de parecer pela sua APROVAÇÃO no rito de defesa.

A outorga do título de mestre está sujeita à homologação pelo colegiado, ao atendimento de todas as indicações e correções solicitadas pela banca e ao pleno atendimento das demandas regimentais do Programa de Pós-Graduação.

CURITIBA, 22 de Fevereiro de 2024.

Assinatura Eletrônica

22/02/2024 19:07:58.0

MARCIO HENRIQUE FRANCO BETTEGA

Presidente da Banca Examinadora

Assinatura Eletrônica

22/02/2024 18:20:57.0

ALESSANDRA DE SOUZA BARBOSA

Avaliador Interno (UNIVERSIDADE FEDERAL DO PARANÁ)

Assinatura Eletrônica

23/02/2024 17:43:21.0

PAULO MANUEL ASSIS LOUREIRO LIMÃO-VIEIRA

Avaliador Externo (UNIVERSIDADE NOVA DE LISBOA)

Agradecimentos

- Ao meu orientador, Professor Dr. Márcio Henrique Franco Bettega. Você foi a pessoa que teve o maior impacto na minha formação, desde a graduação quando era aluno de IC, até agora no final do meu mestrado. Sem você essa dissertação não existiria. Muito obrigado por todos os ensinamentos, oportunidades, amizade e inspiração ao longo de todos esses anos.
- À Professora Dr. Giseli Maria Moreira, que conheci quando era Msc. Giseli Maria Moreira. Desde minha IC você atua como uma pseudo-coorientadora e foi responsável por grande parte da minha formação como cientista. Obrigado pelos ensinamentos, pela inspiração e pela amizade ao longo de todos esses anos.
- À minha família, meu pai Marco, minha mãe Ruth, e meu irmão João, pelo incentivo e apoio por toda a minha vida. Sem vocês, eu -literalmente- não existiria, nem entenderia o porquê vale a pena viver e lutar pelos meus sonhos. Muito obrigado por me criarem para ser quem sou e por me inspirarem a ser sempre melhor do que eu era.
- À minha namorada/esposa/companheira, Paolla Muzillo. Muito obrigado por todo o amor, apoio e companheirismo pelos anos. Seja em momentos felizes, seja em momentos tristes, aprendi muito com você. Obrigado por me completar. Te amo.
- Aos demais professores do grupo de física atômica e molecular, Professora Dra. Alessandra de Souza Barbosa, Professor Dr. Sergio d'Almeida Sanchez e Professor Dr. Thiago Corrêa de Freitas, por toda a amizade e ensinamentos desde a minha época de IC.

- Aos outros professores com os quais tive o prazer de trabalhar durante meu mestrado, Professora Dra. Romarly Fernandes da Costa e Professor Dr. Paulo Limão-Vieira. Obrigado por todos os ensinamentos e oportunidades.
- A todos os demais colaboradores envolvidos em minhas empreitadas científicas.
- Aos membros da banca da defesa, Professora Dra. Alessandra de Souza Barbosa, Professor Dr. Paulo Limão-Vieira, Professor Dr. Márcio Teixeira do Nascimento Varella, e Professor Dr. Rodrigo José Ochekoski Mossanek.
- Aos membros da banca de pré-defesa, Professor Dr. Sergio d'Almeida Sanchez, Professor Dr. Rodrigo José Ochekoski Mossanek, e Professora Dra. Alessandra de Souza Barbosa.
- Aos alunos e ex-alunos do grupo de física atômica e molecular: Vitorino, Ed, Francisco, Murilo, Letícia, Rafael, Diego, Alan, Raul, Cesar, Valéria, Sidnei, Pietra e Barbara, por tudo que aprendi com e junto de vocês.
- A todos os meus amigos. Em especial, ao Vinicius, ao Daniel e ao Thales, por toda a amizade e companheirismo durante praticamente toda a minha existência. Obrigado por crescerem comigo e tornarem minha vida mais leve e alegre.
- Aos meus amigos da época da graduação, em especial Matheus, Giovanni, Kátia, Anderson, Kethelin, André, Mirelle e Carol. Sem o apoio e amizade de vocês, jamais teria concluído a graduação. Muito obrigado.
- Aos meus amigos e colegas da pós-graduação, que juntos trilhamos caminhos por muitas vezes tortuosos em prol de um objetivo maior.
- Ao Professor Dr. Carlos de Carvalho pelo suporte computacional, tanto na hoggar quanto no LCPAD.
- Ao Programa de Pós-graduação em Física (PPGF), ao Departamento de Física e ao Setor de Ciências Exatas da UFPR, por todo suporte nos últimos dois anos.
- À CAPES pelo suporte financeiro.
- À UFPR pela infraestrutura.

"There is a theory which states that if ever anyone discovers exactly what the Universe is for and why it is here, it will instantly disappear and be replaced by something even more bizarre and inexplicable.

There is another theory which states that this has already happened"

Douglas Adams

RESUMO

Nesse trabalho estudamos o espalhamento de elétrons de baixa energia por formamida e metano. Utilizamos o método Schwinger multicanal implementado com pseudopotenciais de norma conservada (SMCPP) dentro da estratégia da base mínima de orbitais para interação de configurações simples (MOB-SCI) para calcular as seções de choque integral e diferencial elásticas e eletronicamente inelásticas. Em todas as seções de choque observamos o efeito do acoplamento multicanal. Embora fenômenos físicos emergentes do espalhamento elástico foram estudados, a sensibilidade das seções de choque eletronicamente inelásticas à pseudoresonâncias e efeitos de threshold nos impede de explorar mais a fundo fenômenos associados à excitação eletrônica. Discutimos as dificuldades e desafios enfrentados durante esse estudo. Além disso, através do modelo *binary-encounter-Bethe* calculamos a seção de choque de ionização total para a formamida e o metano, e a seção de choque total foi estimada para esses sistemas.

Palavras chave: espalhamento de elétrons; seção de choque; excitação eletrônica.

ABSTRACT

In this study, we investigated the scattering of low-energy electrons by formamide and methane. The Schwinger Multichannel method implemented with *norm-conserving* pseudopotentials (SMCPP) was used with the minimal orbital basis for single-configuration interaction (MOB-SCI) approach to calculate the elastic and electronically inelastic integral and differential electron scattering cross sections. In all cross sections, we observed the influence of the multichannel coupling effect. While physical phenomena related to the elastic scattering were explored, the sensitivity of the electronically inelastic cross sections to pseudoresonances and threshold effects inhibit our ability to study phenomena related to the electronic excitation of these molecules. These difficulties and challenges were discussed. Furthermore, the binary-encounter-Bethe model was employed to obtain the total ionization cross section for formamide and methane; and the total cross sections for these systems were estimated.

Key-words: electron scattering; cross section; electronic excitation.

List of Figures

- FIGURE 1.1 (a) Pictorial representation of the plasma-enhanced chemical vapor deposition (PECVD) technique: Precursor molecules are introduced in a reaction chamber where a plasma (represented in pink) is generated. This plasma is rich in low-energy electrons, also depicted in the figure. The reactions promoted by the plasma dissociates the molecules, leaving a deposit in the substrate and the waste is pumped out of the reaction chamber. (b) Figure adapted from Thorman *et al.* [7] depicting the focused electron beam induced deposition (FEBID) technique. A high-energy primary beam of electrons dissociated precursor molecules that are adsorbed on the substrate, manufacturing the deposit. This primary beam also ionizes the molecules of the substrate and the deposit itself, producing secondary low-energy electrons that may dissociated the precursor molecules outside the region of the primary beam. 23
- FIGURE 1.2 Figure taken from Shulenberger *et al.* [10] depicting the production of low-energy electrons in the interstellar medium due to the interaction between an incident high-energy ionizing radiation and matter and the subsequently chemical reactions promoted by the low-energy electrons produced. 24
- FIGURE 1.3 (a) Pictorial representation of the interaction between a primary high-energy radiation (yellow arrow) with the biological medium. These interactions produce a vast quantity of secondary low-energy electrons that may interact with molecules in the environment (Adapted from Ref. [12]). (b) Measurements of double strand-breaks of DNA due to the impact of low-energy electrons are given in **A**; single strand-breaks of DNA in **B**; and the loss of supercoiled character of DNA in **C** (Taken from Ref. [13]). 24
- FIGURE 1.4 Schematic representation of different types of resonant states. The energy of the ground and an electronically excited state of the neutral molecule are represented in the left. In the right three possible resonances are shown. The shape resonance has the ground state of the neutral molecule as a parent state, while the Feshbach and core excited resonances have the electronically excited state of the molecule as a parent state. 25

FIGURE 1.5	Schematic representation of the dissociation dynamics started by low-energy electrons. (a) Dissociative electron attachment: An incident electron is captured by the molecular target forming an anion of σ^* or π^* character, that may dissociate directly or indirectly, respectively. (b) Neutral dissociation through catalytic electron: the target molecule is electronically excited by the incoming electron, which after autodetachment leaves the molecule in an electronically excited state. In turn, this electronically excited state may dissociate forming neutral fragments. (Figure adapted from Lozano <i>et al.</i> [19])	26
FIGURE 1.6	Schematic representation of the chemical structure of formamide (generated with MacMolPlt [35]).	28
FIGURE 1.7	Schematic representation of the chemical structure of methane (generated with MacMolPlt [35]).	29
FIGURE 2.1	An incident beam of particles "A" being scattered by a target composed of scattering centers "B". The scattered particles are detected outside the range of the interaction potential. Figure taken from Ref. [76].	31
FIGURE 2.2	(a) Schematic representation of vertical excitation energies of the electronically excited states of a fictitious molecule AB obtained through a MOB-SCI calculation. (b) Possible multichannel coupling strategy used in the scattering calculations. For more details, see the text.	48
FIGURE 2.3	Procedure to obtain the final MC cross sections for the fictitious molecule AB. Firstly, the ICSs are calculated with the different levels of multichannel coupling, as established in the strategy depicted in Fig. 2.2 (Left panel). Then, the ICS calculated with the highest amount of open channels is selected in each energy regime (Middle panel). Finally, the MC ICS is obtained concatenating the ICSs selected in the previous step (Right panel). A low-energy resonance and the multichannel coupling effect are also depicted in the figure.	50
FIGURE 2.4	Pictorial representation of the formation of a resonance. The effective potential felt by the incoming electron (from the right) is composed of an attractive square well and a angular momentum barrier. While an incident electron with energy E_1 is scattered back to the continuum, the effective well traps an electron with incident energy E_2	53

FIGURE 2.5	Pictorial representation of the multichannel coupling effect in the flow of water in a pipe system. Firstly, only one pipe is open, thus all the water flows only through this accessible channel (a). Then, more pipes are opened, allowing the water to flow through them, which reduces the flux that flows through the original channel (b).	57
FIGURE 3.1	Schematic representation of formamide's chemical structure (generated with MacMolPlt [35]).	59
FIGURE 3.2	Schematic representation of the vertical excitation energies (in eV) of the 178 electronically excited states of formamide obtained with the MOB-SCI calculation and the different multichannel coupling strategies employed in the scattering calculations. The dashed red line corresponds to the threshold of the 3ch scattering calculation; dashed green line, 4ch; dashed brown line, 6ch; dashed olive line, 22ch; dotted orange line, 57ch; dash-dot-dot pink line, 103ch; long-dashed purple line, 135ch; double-dotted cyan line, 154ch; dash-dot orange line, 167ch; dotted red line, 177ch. The 179ch threshold is also indicated.	64
FIGURE 3.3	Elastic DCSs for the scattering of electrons by formamide calculated with different multichannel coupling schemes. Dash-dotted blue line, 1ch; dashed red line, 3ch; dashed green line, 4ch; dashed brown line, 6ch; dashed olive line, 22ch; dotted orange line, 57ch; dash-dot-dot pink line, 103ch; long-dashed purple line, 135ch; double-dotted cyan line, 154ch; dashed orange line, 167ch; dotted red line, 177ch and full black line, 179ch.	66
FIGURE 3.4	Elastic DCSs for the impact energies of 2 and 4 eV. Dash-dot blue line, present 1ch; short-dashed red line, results from Wang and Tian (R-Matrix) [43]; dash-double-dotted olive line, results from Vinodkumar <i>et al.</i> (R-Matrix) [46]; dotted purple line, results from Homem <i>et al.</i> (SCE+Padé) [45]; dashed orange line, results from Silva <i>et al.</i> (SMCPP) [47].	67
FIGURE 3.5	Elastic DCSs for the impact energies of 6, 8, 10, 12 and 14 eV. Dash-dot blue line, present 1ch; full black line, present results obtained with the highest multichannel coupling (MC) scheme in each impact energy (3ch at 6 eV, 6ch at 8 eV, 22ch at 10 eV and 12 eV and 57ch at 14 eV); short-dashed red line, results from Wang and Tian (R-Matrix) [43]; dotted purple line, results from Homem <i>et al.</i> (SCE+Padé) [45]; dash-double-dotted olive line, results from Vinodkumar <i>et al.</i> (R-Matrix) [46]; dashed orange line, results from Silva <i>et al.</i> (SMCPP) [47].	67

FIGURE 3.6	Elastic ICS calculated using different multichannel coupling schemes. The lines in color follow the caption of Fig. 3.3.	68
FIGURE 3.7	Upper panel: Elastic ICS without the Born-closure procedure for the scattering of electrons by formamide. Lower panel: Elastic ICS with the Born-closure procedure. Full black line, present MC results; dashed green line, results from Bettega (SMCPP) [42]; dashed red line, SEP results from Wang and Tian (R-Matrix) [43]; dotted red line, CC results from Wang and Tian (R-Matrix) [43]; dashed orange line, results from Silva <i>et al.</i> (SMCPP) [47]; and dotted purple line, results from Homem <i>et al.</i> (SCE+Padé) [45]. The position of the resonances from Seydou <i>et al.</i> (Experimental) [39] and Goumans <i>et al.</i> (Theory) [49] are also presented as a vertical blue line and vertical dashed pink lines; respectively.	70
FIGURE 3.8	DCSs for the electronic excitation of the $1^3A'$ (5.572 eV) state of formamide. The color code follows Fig. 3.2: Dashed red line, 3ch; dashed green line, 4ch; dashed brown line, 6ch; dashed olive line, 22ch; dotted orange line, 57ch; dash-dot-dot pink line, 103ch; long-dashed purple line, 135ch; double-dotted cyan line, 154ch; dot-dashed orange line, 167ch; dotted red line, 177ch; solid black line, 179ch.	71
FIGURE 3.9	Same as in Fig. 3.8, but for the $1^3A''$ (5.841 eV) state	72
FIGURE 3.10	Same as in Fig. 3.8, but for the $1^1A''$ (6.416 eV) state	72
FIGURE 3.11	Same as in Fig. 3.8, but for the $2^3A''$ (7.540 eV) state	73
FIGURE 3.12	ICSs for the excitation of formamide to the $1^3A'$ (5.572 eV), $1^3A''$ (5.841 eV), $1^1A''$ (6.416 eV) and $2^3A''$ (7.450 eV) states. Full black line, present MC results; dashed red line, results from Wang and Tian (R-Matrix) [43]; dash-double-dotted olive line, results from Vinodkumar <i>et al.</i> (R-Matrix) [46].	74
FIGURE 3.13	TECS for the electron scattering by formamide. This cross section was obtained summing all the electronically inelastic ICSs.	74
FIGURE 3.14	Full black line, present TICS; dashed orange line, TICS from Gupta <i>et al.</i> (BEB) [44]; and dashed purple line, TACS from Homem <i>et al.</i> (SCE+Padé) [45].	76
FIGURE 3.15	TCS for the electron scattering by formamide. Full black line, present TCS; dashed purple line, TCS from Homem <i>et al.</i> (SCE+Padé) [45]; dash-double-dotted olive line, TCS from Vinodkumar <i>et al.</i> (R-Matrix) [46]; dashed-dotted blue line, elastic ICS calculated without the Born-Closure procedure.	76

FIGURE 4.1	Schematic representation of the chemical structure of methane (generated with MacMolPlt [35]).	78
FIGURE 4.2	Schematic representation of the vertical excitation energies (in eV) of the 180 electronically excited states (according to the C_{2v} point group) of methane obtained with the MOB-SCI calculation and the different multichannel coupling strategies employed in the scattering calculations. The lines in color indicate the best level of channel coupling at the energy shown in parenthesis. The dashed red line corresponds to the threshold of the 4ch scattering calculation; dotted blue line, 7ch; dash-dotted green line, 8ch; dash-dot-dotted orange line, 24ch; small-dash-dotted cyan line, 61ch; dashed magenta line, 97ch; double-dashed purple line, 129ch; small-dashed olive line, 132ch; dashed pink line, 153ch; triple-dotted brown line, 175ch; and dotted black line, 181ch.	85
FIGURE 4.3	Elastic integral cross section for electron scattering by methane. Dashed red line, 1ch result; dotted blue line, 1ch-FSCI; full black line, MC cross section.	87
FIGURE 4.4	Elastic integral cross section for electron scattering by methane compared with theoretical (upper panel) and experimental (lower panel) results. Upper panel: dotted blue line, 1ch-FSCI result; full black line, MC result; long-dash-dotted cyan line, Lengsfeld <i>et al.</i> (CKVM) [61]; dot-dash-dotted yellow line, Nestmann <i>et al.</i> (R-Matrix) [62]; dashed pink line, Althorpe <i>et al.</i> (SCE) [64]; dash-dot-dotted green line, Bettega <i>et al.</i> (SMCPP) [65]; double-dotted purple line, Cho <i>et al.</i> (ISVM + COP) [33]; dot-dot-dotted olive line, Vinodkumar <i>et al.</i> (R-Matrix) [66]; and dotted orange line, Ziólkowski <i>et al.</i> (R-Matrix) [75]. Lower panel: dotted blue line, 1ch-FSCI; full black line, MC results; green crosses, Fuss <i>et al.</i> (recommended) [57]; blue squares, Song <i>et al.</i> (recommended) [58]; brown crosses (x), Sohn <i>et al.</i> (Experimental) [67]; red triangles, Shyn and Cravens [68]; orange circles, Boesten and Tanaka (Experimental) [69]; open dotted purple dots, Cho <i>et al.</i> (Experimental) [33]; and dark-green diamonds, Vuškovic and Trajmar (Experimental) [70].	88

FIGURE 4.5	Elastic integral cross section for energies below 1 eV calculated at the 1ch-FSCI approximation, dotted blue line; and MC level, full black line; alongside results from the literature: dot-dash-dotted yellow line, Nestmann <i>et al.</i> (R-Matrix) [62]; dashed pink line, Althorpe <i>et al.</i> (SCE) [64]; dot-dot-dotted olive line, Vinodkumar <i>et al.</i> (R-Matrix) [66]; dotted orange line, Ziólkowski <i>et al.</i> (R-Matrix) [75]; green crosses (+), Fuss <i>et al.</i> (recommended) [57]; blue squares, Song <i>et al.</i> (recommended) [58]; and brown crosses (x), Sohn <i>et al.</i> (Experimental) [67].	89
FIGURE 4.6	Left panel: full black line, MC ICS; dashed black line, <i>s</i> -wave MC cross section; dotted black line, <i>p</i> -wave MC cross section; dotted blue line, <i>s</i> -wave 1ch-FSCI; cyan squares, Lengsfeld <i>et al.</i> (R-Matrix) [61]. Right panel: <i>s</i> -wave MC eigenphase; and dotted blue line, <i>s</i> -wave 1ch-FSCI eigenphase. The RT-minimum of methane is seen at 0.350 eV in the MC approximation and at 0.530 eV in the 1ch-FSCI calculation.	89
FIGURE 4.7	Differential elastic cross sections for the electron scattering by methane at selected energies. The lines and points follow the same labels as in Fig. 4.4. Note that for energies below the first excitation threshold the cross sections obtained according to the 1ch and MC calculations coincide.	90
FIGURE 4.8	Differential elastic cross sections for the electron scattering by methane at selected energies. The lines and points follow the same labels as in Fig. 4.4. Note that for energies below the first excitation threshold the cross sections obtained according to the 1ch and MC calculations coincide.	91
FIGURE 4.9	Differential elastic cross sections for the electron scattering by methane at selected energies. The lines and points follow the same labels as in Fig. 4.4.	91
FIGURE 4.10	Integral cross section for the 9 first electronically inelastic channels of methane. Full black line, present MC results; dotted magenta line, Winstead <i>et al.</i> (SMC) [71]; dash-dotted dark blue line, Gil <i>et al.</i> (CKVM) [72]; dash-dot-dotted green line, Bettega <i>et al.</i> (SM-CPP) [73]; and dashed orange line, Ziólkowski <i>et al.</i> (R-Matrix) [75]. See text for a detailed discussion.	93
FIGURE 4.11	Differential cross sections for the excitation of methane from the ground state to the 1^3T_2 electronically excited state at selected impact energies. Full black line, present MC results; and dotted magenta line, Winstead <i>et al.</i> (SMC) [71].	95

FIGURE 4.12	Same as in Fig. 4.11, except that these are for the 1^1T_2 electronically excited state.	95
FIGURE 4.13	Differential cross sections for the excitation of methane. Full black line, present MC results including all accessible electronically inelastic channels under 15 eV; dashed black line, MC with only the 1^3T_2 and 1^1T_2 electronic excitation cross sections; dotted magenta line, summed 1^3T_2 and 1^1T_2 excitation differential cross sections from Winstead <i>et al.</i> (SMC + Born-closure) [71]; dark-green diamonds, Vuškovic and Trajmar (Experimental) [70]. for energy losses of 7.5 to 15 eV.	96
FIGURE 4.14	Total excitation cross section of methane. Full black line, present MC results calculated with all 180 electronically inelastic cross sections; dashed black line, MC results considering only the first 54 electronically inelastic cross sections; dash-dotted dark blue line, Gil <i>et al.</i> (CKVM) [72]; and dash-dot-dotted indigo line, Joshipura <i>et al.</i> [74].	97
FIGURE 4.15	Total ionization cross section for electron scattering by methane. Full black line, present BEB calculation; green crosses, Fuss <i>et al.</i> (recommended) [57]; blue squares, Song <i>et al.</i> (recommended) [58]; dash-dotted dark green line, Kim <i>et al.</i> (BEB) [122]; and dashed violet line, Deutsch <i>et al.</i> (DM) [123].	98
FIGURE 4.16	Total cross section for electron scattering by methane. Full black line, present results; green crosses, recommended data from Fuss <i>et al.</i> [57]; and blue squares, recommended data from Song <i>et al.</i> [58].	99
FIGURE B.1	Ball and stick model of the chemical structure of (a) dimethyl peroxide and (b) ethylene glycol (generated with MacMolPlt [35]). . .	123
FIGURE B.2	Upper panel: ICS for the electrons scattering by DMP Lower panel: MTCS for the electron scattering by DMP. For both panels: full purple line, SEP results; double-dotted purple line, SE results; dashed green line, results from Araújo <i>et al.</i> [134].	127
FIGURE B.3	Symmetry decomposition of the ICS for the electron scattering by DMP. For both panels: full purple line, SEP results; double-dotted purple line, SE results; dashed green line, results from Araújo <i>et al.</i> [134].	129
FIGURE B.4	Resonant orbitals obtained from the diagonalization of the scattering Hamiltonian in the CSF space used in the SEP calculation for DMP.	129

FIGURE B.5	Upper row: partial wave decomposition of the SEP ICS for DMP. Only the partial waves with a relevant contribution are shown. Lower row: eigenphase sum.	130
FIGURE B.6	DCSs for the electron scattering by DMP for selected energies. Full purple line, SEP results; double-dotted purple line, SE results; dashed green line, results from Araújo <i>et al.</i> [134].	131
FIGURE B.7	Upper panel: ICS for the electrons scattering by ETG. Lower panel: MTCS for the electron scattering by ETG. For both panels: full red line, SEP results; dash-dot red line, SE results; dashed green line, results from Araújo <i>et al.</i> [134].	132
FIGURE B.8	Symmetry decomposition of the ICS for the electron scattering by ETG. For both panels: full red line, SEP results; dash-dot red line, SE results; dashed green line, results from Araújo <i>et al.</i> [134]. . .	133
FIGURE B.9	Resonant orbitals obtained from the diagonalization of the scattering Hamiltonian in the CSF space used in the SEP calculation for ETG.	133
FIGURE B.10	Upper row: partial wave decomposition of the SEP ICS for ETG. Only the partial waves with a relevant contribution are shown. Lower row: eigenphase sum.	134
FIGURE B.11	DCSs for the electron scattering by ETG for selected energies. Full red line, SEP results; dash-dot red line, SE results; dashed green line, results from Araújo <i>et al.</i> [134].	135
FIGURE B.12	ICSs for electron scattering by DMP and ETG. Dotted purple line, SEP DMP; double-dotted purple line, SE DMP; full red line, SEP ETG; and dash-dot red line, SE ETG.	137
FIGURE B.13	Symmetry decomposition of the ICS of DMP and ETG. Only the resonant symmetries in the SEP approximation are presented. Dotted purple line, SEP DMP; and full red line, SEP ETG.	138
FIGURE B.14	DCS for the electron scattering by DMP and ETG. Dotted purple line, SEP DMP; double-dotted purple line, SE DMP; full red line, SEP ETG; and dash-dot red line, SE ETG.	138
FIGURE C.1	Representation of the scattering of a particle by a rigid sphere of radius R . The incident particle has an impact parameter b and is scattered in the direction defined by the angle θ	141
FIGURE C.2	Different arrangements of extra centers used in the tests presented in table C.1. The arrangement of the left was used for the $FSCI_{ce_1}$, $FSCI_{ce_2}$ and $FSCI_{ce_3}$ calculations, while the one on the right was used for the $FSCI_{ce_4}$ and $FSCI_{ce_5}$ calculations.	146

List of Tables

TABLE 3.1 – Exponents of the uncontracted basis functions for the C, N and O atoms.	62
TABLE 3.2 – Vertical excitation energies (in eV) for the first 10 excited electronic states obtained from a full single configuration interaction (FSCI), minimal orbital basis for single configuration interaction (MOB-SCI) and EOM-CCSD/aug-cc-pVDZ calculations. We compared our results with the theoretical results of Wang and Tian (CAS-Cl/cc-pVTZ) [43], Vinodkumar <i>et al.</i> (Cl/6-311G) [46], Chong (TDDFT/(SAOP)/et-pVQZ) [112] and Hirst <i>et al.</i> (MRCI/6-31+g**) [113] and also with the experimental results of ^α Gingell <i>et al.</i> (VUV and EELS) [114], ^β Staley <i>et al.</i> (ion cyclotron resonance detection) [115], and ^γ Basch <i>et al.</i> (VUV) [116].	63
TABLE 3.3 – Chosen values for l_{SMC} for the Born-Closure procedure performed in the calculations of the elastic cross sections. Energy ranges are presented in eV.	65
TABLE 3.4 – Channel coupling strategies used for each electron impact energy (in eV) interval to compute the final cross sections obtained in the multichannel coupling (MC) approximation.	69
TABLE 3.5 – Position of the shape resonance found by the present calculation and from the literature (in eV).	71
TABLE 4.1 – Relation between the irreducible representations of the T_d and C_{2v} point groups.	81
TABLE 4.2 – Exponents of the basis functions used in the C atom and extra centers.	82
TABLE 4.3 – Excitation energies (in eV) of the first few electronically excited states of methane. Results for the vertical excitation energies calculated with the FSCI, MOB-SCI and EOM-CCSD/aug-cc-pVDZ are compared to previous theoretical results from Winstead <i>et al.</i> (IVOs) [71], Gil <i>et al.</i> (IVOs) [72], Bettega <i>et al.</i> (IVOs) [73], Ziółkowski <i>et al.</i> (CASCI) [75] and Mebel <i>et al.</i> (MRCI+D) [124] and to experimental results obtained from the maximum in the structures of the measured spectra (Expt.) [125–127]. See text for a detailed discussion.	83

TABLE 4.4–Number of configurations of each symmetry according to the C_{2v} point group used in the scattering calculations. MC: configuration space constructed with 90 hole-particle pairs and all unoccupied molecular orbitals as scattering orbitals; FSCI: configuration space constructed using all occupied and unoccupied molecular orbitals as hole, particle and scattering orbitals.	84
TABLE 4.5–Channel coupling strategies used for each electron impact energy (in eV) interval to compute the final cross sections obtained in the multichannel coupling (MC) approximation.	86
TABLE B.1–Number of configuration state functions per symmetry used in the static-exchange plus polarization approximation calculation for each molecule.	126
TABLE B.2–Resonances positions for DMP and ETG obtained at the SE and SEP levels of approximation and energy eigenvalues of the resonant states of the scattering Hamiltonian (H_{N+1}). Results from Araújo <i>et al.</i> [134] are also shown for comparison. All values are in eV.	135
TABLE C.1–Vertical excitation energy of the electronically excited states of methane. See text for a detailed discussion.	145
TABLE C.2–Vertical excitation energy of methane obtained through the MOB-SCI approach. See text for details.	147
TABLE D.1–Cartesian coordinates of the atoms in the optimized geometry of dimethyl peroxide at the MP2/aug-cc-pVDZ level of theory. All units are in Bohr.	148
TABLE D.2–Cartesian coordinates of the atoms in the optimized geometry of ethylene glycol at the MP2/aug-cc-pVDZ level of theory. All units are in Bohr.	149
TABLE D.3–Cartesian coordinates of the atoms in the optimized geometry of formamide at the MP2/aug-cc-pVDZ level of theory. All units are in Bohr.	149
TABLE D.4–Parameters for the BEB model for formamide obtained through a HF/aug-cc-pVDZ calculation at the optimized geometry. All orbitals are doubly occupied. Energies are in Hartree.	149
TABLE D.5–Parameters for the BEB model for methane obtained through a HF/aug-cc-pVQZ according to the T_d point group (note that the orbital $1t_2$ is triply-degenerated). Energies are in Hartree.	150

Contents

1	INTRODUCTION	22
2	THEORY	30
2.1	Basic concepts	30
2.2	The Schwinger Multichannel Method	34
2.2.1	Scattering Amplitude	34
2.2.2	Approximation Level	40
2.2.2.1	Elastic approximation	41
2.2.2.2	Multichannel coupling approximation	44
2.3	Binary-Encounter-Bethe model	51
2.4	Electron Scattering Phenomena	52
2.4.1	Resonances	52
2.4.2	Ramsauer-Townsend Minimum	55
2.4.3	Multichannel Coupling Effect	55
3	FORMAMIDE	59
3.1	Computational Details	61
3.2	Elastic channel	65
3.3	Electronically inelastic channels	71
3.4	Total ionization cross section	75
3.5	Total cross sections	75
3.6	Conclusion	77
4	METHANE	78
4.1	Computational Details	81
4.2	Elastic Channel	86
4.3	Electronically Inelastic Channels	92
4.4	Total Ionization Cross Section	98
4.5	Total Cross Section	99
4.6	Conclusion	100
5	CONCLUSION	101
	BIBLIOGRAPHY	103
	Appendix	119
A	SCIENTIFIC CONTRIBUTIONS	120
B	DIMETHYL PEROXIDE AND ETHYLENE GLYCOL	123
B.1	Computational Details	125
B.2	Dimethyl Peroxide	126
B.3	Ethylene Glycol	131

B.4	Comparison	136
B.5	Conclusion	139
C	ADDITIONAL THEORETICAL DETAILS	140
C.1	The Born-closure procedure	140
C.2	Pseudopotentials	142
C.3	Frame transformation	143
C.4	Example of the MOB-SCI procedure	144
D	GEOMETRY AND BEB PARAMETERS	148

CHAPTER 1

Introduction

The interactions between low-energy electrons (LEEs) and molecules have interested the scientific community for many decades. LEEs have the potential to initiate many important chemical and physical reactions that take part in many environments, extending from technological applications to the biological and astrophysical media [1]. Thus, to fully understand the underlying physics and chemistry of these environments, mathematical models must take into account the interactions between LEEs and molecules [2, 3]. Furthermore, the abundance of physical phenomena that emerge from electron-molecule interactions holds great appeal from an academic standpoint, given the presence of numerous open questions. For instance, the unequivocally determination of electronic excitation cross sections is still a challenging task, as will be discussed throughout this dissertation.

The interaction between LEEs and molecules are important in industrial techniques used to manufacture microchips and semiconductors, such as in plasma-enhanced chemical vapor deposition (PECVD, Fig. 1.1 (a)) and focused electron beam induced deposition (FEBID, Fig. 1.1 (b)). In PECVD a gas composed of precursor molecules that contains atoms of interest is pumped into a reaction chamber. Then, a plasma is used to promote chemical reactions on this gas and, through these reactions, creates a deposit on a substrate [4, 5]. This plasma environment has a vast quantity of low-energy electrons that interact with the precursor molecules. In FEBID a high energy electron beam is used to dissociate the precursor molecules that are adsorbed on a substrate to create a deposit [6]. This high energy beam also ionizes the constituents of the substrate and the deposit itself, generating a vast quantity of secondary LEEs that

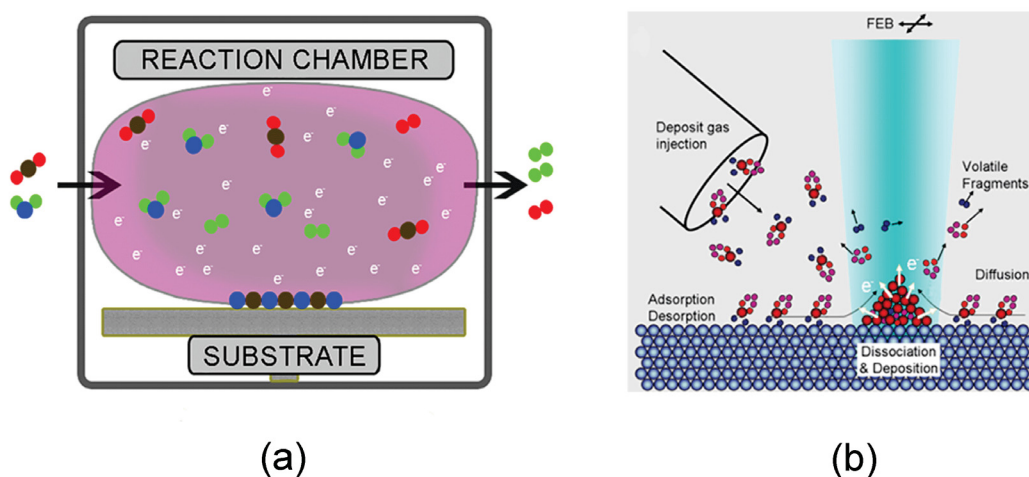


Figure 1.1 – (a) Pictorial representation of the plasma-enhanced chemical vapor deposition (PECVD) technique: Precursor molecules are introduced in a reaction chamber where a plasma (represented in pink) is generated. This plasma is rich in low-energy electrons, also depicted in the figure. The reactions promoted by the plasma dissociates the molecules, leaving a deposit in the substrate and the waste is pumped out of the reaction chamber. (b) Figure adapted from Thorman *et al.* [7] depicting the focused electron beam induced deposition (FEBID) technique. A high-energy primary beam of electrons dissociated precursor molecules that are adsorbed on the substrate, manufacturing the deposit. This primary beam also ionizes the molecules of the substrate and the deposit itself, producing secondary low-energy electrons that may dissociated the precursor molecules outside the region of the primary beam.

interact with the adsorbed molecules outside the primary beam range, possibly dissociating these molecules, creating imperfections and consequently limiting the resolution obtained through this technique [7]. Therefore, understanding how low-energy electrons interact with the precursor molecules used in these industrial techniques is fundamental to understand the nature of these processes and to improve their efficiency.

LEEs also play an important role in astrochemistry [8]. They are produced in vast quantities on the interstellar medium through the interaction between high energy radiation (*viz.*, cosmic rays, γ rays, x-rays, high energy electrons and ions) and matter. In turn, these secondary LEEs interact with the molecules present in the interstellar medium promoting physical and chemical reactions that may lead to molecular dissociation and the production of free radicals (Fig. 1.2). Therefore, LEEs may play a fundamental role in the synthesis of complex organic molecules in the interstellar medium [9, 10]. Particularly, these may be prebiotic molecules, that is, precursor molecules that are involved in the synthesis of complex organic molecules which are considered building blocks for the formation of life [11]. Thus, LEEs may be related to the origin of life itself, emphasizing the importance of including the electron-molecule interaction in mathematical models that describe these environments.

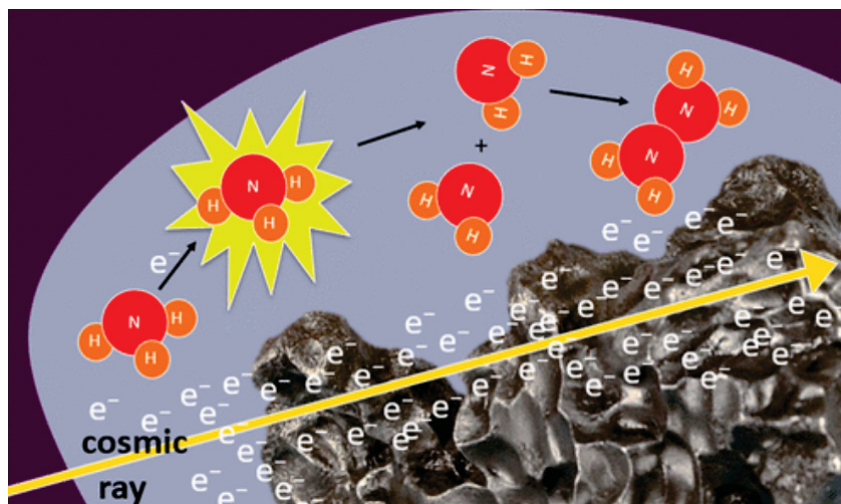


Figure 1.2 – Figure taken from Shulenberg *et al.* [10] depicting the production of low-energy electrons in the interstellar medium due to the interaction between an incident high-energy ionizing radiation and matter and the subsequently chemical reactions promoted by the low-energy electrons produced.

In the biological medium there is a vast production of LEEs due to the interaction between high-energy ionizing radiation and the biological material (Fig. 1.3 (a)). These secondary LEEs have the potential to initiate significant chemical and physical reactions. Interest in these interactions between LEEs and molecules within the biological medium has grown since Boudaïffa *et al.* published their seminal work in the early 2000's [13]. These authors showed that LEEs are capable of damaging the genetic material through single- and double-strand breaks of DNA for incident electron energies that are bel-

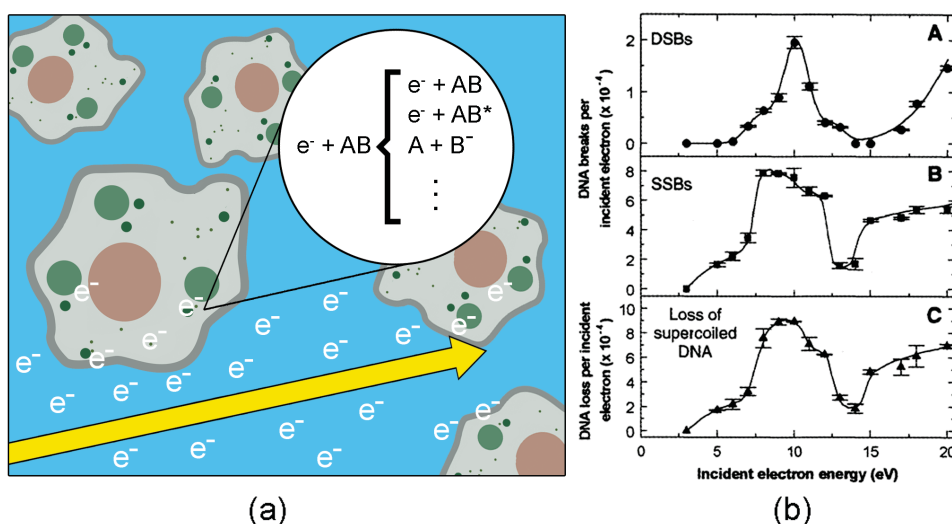


Figure 1.3 – (a) Pictorial representation of the interaction between a primary high-energy radiation (yellow arrow) with the biological medium. These interactions produce a vast quantity of secondary low-energy electrons that may interact with molecules in the environment (Adapted from Ref. [12]). (b) Measurements of double strand-breaks of DNA due to the impact of low-energy electrons are given in **A**; single strand-breaks of DNA in **B**; and the loss of supercoiled character of DNA in **C** (Taken from Ref. [13].).

low the ionization threshold of the molecules (Fig. 1.3 (b)), bringing to attention the importance of LEEs in the biological environment. As a consequence of this work, many studies regarding the interactions between bio-molecules and LEEs have been made throughout the years (See, for instance, Ref. [14] and references therein). These have a direct impact on improving the efficiency of radiotherapy treatments, since in this context a high-energy ionization radiation beam is irradiated upon the biological environment. For this to be most effective, that is, destroy the highest amount of malignant cells in the cancerous tissue while keeping the healthy tissue as undamaged as possible, it is necessary to know how the primary high-energy radiation and its by-products, i.e. LEEs, interact with bio-molecules [2]. An example of how interactions between LEEs and molecules can be beneficial to radiotherapy is illustrated by radiosensitizers. These are molecules that, upon interacting with LEEs, produce fragments capable of enhancing injury to tumor tissue by accelerating DNA damage [15–17].

Another important aspect shown by Boudaïffa *et al.* [13] is that, for incident energies below the ionization threshold, the induced damage is highly dependent on the incident electron energy (Fig. 1.3 (b)). This is due to the formation of a resonant state, that in turn may lead to molecular dissociation and ultimately to DNA damage. A resonant state is a transient negative ion (also referred to simply as resonance) formed by the capture of the incident electron by an unoccupied molecular orbital [18]. These resonances can be categorized into two types, determined by whether the

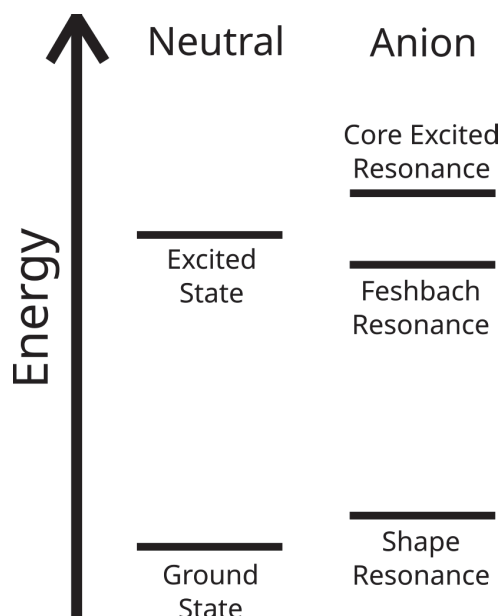


Figure 1.4 – Schematic representation of different types of resonant states. The energy of the ground and an electronically excited state of the neutral molecule are represented in the left. In the right three possible resonances are shown. The shape resonance has the ground state of the neutral molecule as a parent state, while the Feshbach and core excited resonances have the electronically excited state of the molecule as a parent state.

molecule maintains its electronic ground state throughout the scattering of the incident electron or undergoes electronic excitation (Fig. 1.4). If the molecule does remain in its electronically ground state, a shape resonance is formed. The name "shape resonance" is derived from the shape of the electron-molecule interaction potential, that will be further explained in chapter 2. The character of the orbital in which the incident electrons is temporarily trapped is what determines the character of the resonant state, namely the anti-bonding σ^* and π^* characters. Now, if during the scattering process the incident electron is captured by the molecule and simultaneously the molecule is electronically excited, the anionic state formed can either be classified as a Feshbach resonance or a core excited resonance. For Feshbach resonances, the parent state—that is, the electronically excited state to which the neutral molecule is excited during the scattering process—has an energy level above the resonant state. Conversely, the opposite occurs for core excited resonances, where the resonant states lies above the parent state.

The main mechanism responsible for the DNA damage reported by Boudaïffa *et al.* [13] is known as dissociative electron attachment (DEA) [20]. Firstly, a resonant state is formed. Then, this resonance may either decay by autodetachment, where the additional electron is emitted to the continuum leaving the molecule vibrationally excited in an electronic state, where shape resonances leave the molecule in the ground state

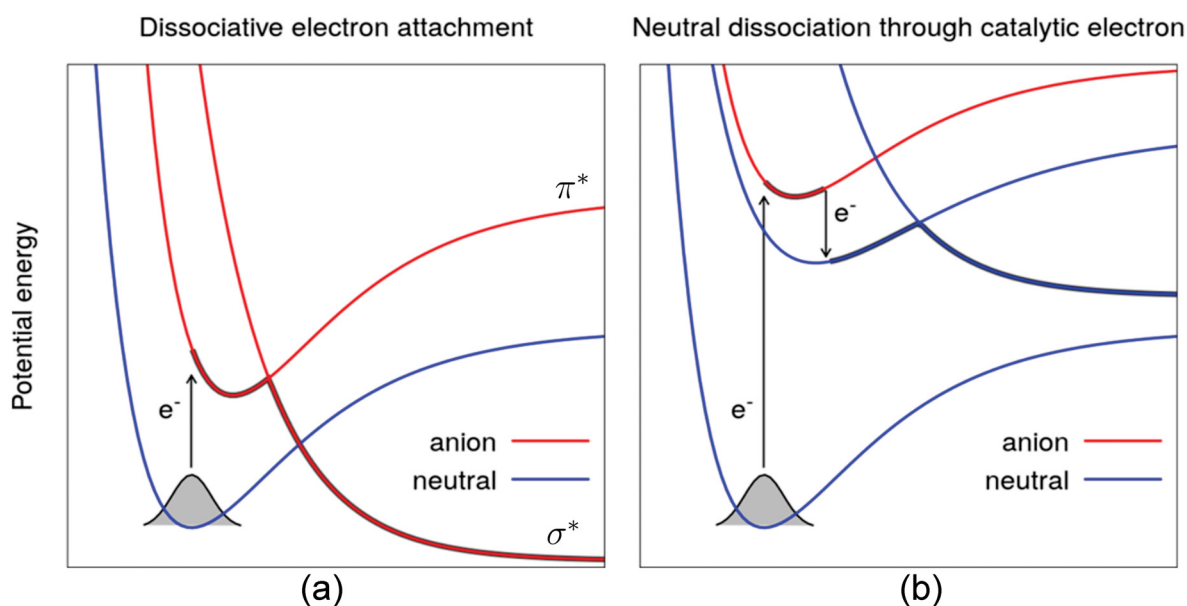


Figure 1.5 – Schematic representation of the dissociation dynamics started by low-energy electrons. (a) Dissociative electron attachment: An incident electron is captured by the molecular target forming an anion of σ^* or π^* character, that may dissociate directly or indirectly, respectively. (b) Neutral dissociation through catalytic electron: the target molecule is electronically excited by the incoming electron, which after autodetachment leaves the molecule in an electronically excited state. In turn, this electronically excited state may dissociate forming neutral fragments. (Figure adapted from Lozano *et al.* [19])

while Feshbach and core-excited resonances may leave the molecule electronically excited¹; or may dissociate into neutral and anionic fragments. The dissociation may occur in a direct or indirect pathway [21–24]. In the direct one the electron is captured by a σ^* molecular orbital and the anionic state of the molecule is dissociative [21]. On the other hand, in the indirect pathway a non dissociative anionic state is formed by the capture of the incident electron into a π^* molecular orbital and, as the nuclei relaxes due to the transition from the ground to the anionic state, the potential curve from the stable π^* anion crosses the potential curve of the dissociative σ^* anion, leading to molecular dissociation (Fig. 1.5 (a)) [22]. In the case of DNA, the incident electron is captured by one of the DNA basis, that dissociates through DEA and ultimately lead to single- and double-strand breaks in the DNA molecule itself [25–27]. Therefore, the knowledge of how these resonances form and what are their products are relevant to understand the chemical reactions that may occur in the biological environment.

As mentioned in the previous paragraph, in contrast to shape resonances, Feshbach and core excited resonances may leave the target molecule in an electronically excited state after autodetachment. Thus, not only these resonances may undergo DEA, but also produce neutral fragments through the excitation of the molecular target to a dissociative electronically excited state [19] (Fig. 1.5 (b)). Therefore, investigating the electronic excitation of molecules by electrons may promote important insights regarding possible molecular dissociation mechanisms [19, 28].

With these applied and academical motivations in mind, a handful of theoretical methods have been developed to calculate the cross sections for the scattering of electrons by molecules over the years [29–34]. The cross sections are physical quantities that characterize electron-molecule interactions, and are going to be discussed in detail in chapter 2. Although these methods have been established for many decades and provide a good description of the elastic scattering, where there is no energy exchange between the incident electron and the molecular target, the description of electronic excitation of molecular targets by electron impact is still challenging. From the theoretical point of view, the cross section calculations for such process rely on the description of the electronic excited states, a method that is capable of addressing such a collision problem and a computational facility capable of addressing such expensive calculations. There are only few *ab-initio* methods that allow these calculations, such as the R-matrix [29], the complex Kohn [30] and the Schwinger multichannel [31, 32] methods. Other theoretical approaches make use of a complex potential to take the inelastic processes into account (in this case inelastic means all that is not elastic) [33, 34], thus not being able to resolve individual excitation channels. As a consequence of these difficulties, there is a lack of cross sections in the literature regarding electronically

¹ Note that, due to energy conservation, Feshbach resonances do not decay to their parent state, but may decay to another low-lying electronically excited state of the molecule.

inelastic scattering of electrons by molecules.

In the present work, we studied the interaction between LEEs and formamide and methane. The ball and stick model of these molecules are shown in Figs. 1.6 and 1.7. Our work focused on the electronic excitation of these molecules by electron impact. With these calculations we intended not only to complement the set of cross sections available in the literature for these systems, contributing with reliable data for modeling the biological, astrophysical and technological media; but also study important aspects of the description of the scattering process itself, such as the formation of resonances, Ramsauer-Townsend minimum and multichannel coupling effects.

Formamide [HCONH_2] (Fig. 1.6) is the simplest molecule containing a peptide bond. For this reason, it is an important building block for complex organic molecules and has been used to study the low-energy electron damage on the peptide backbone of proteins [36]. Besides that, it has also been observed in the interstellar medium [37, 38] and is an important prebiotic molecule that may be associated with the origin of life itself [11]. Thus, the interactions between electrons and formamide are relevant both in the biological and interstellar environments. A few experimental studies have been published in the literature [39–41], none of which have reported cross sections. Although the electron-formamide interactions have been extensively studied theoretically [42–50], only two studies reported electronically inelastic cross sections [43, 46]. This motivated us to further study the electron interactions with formamide, focusing on the electronic excitation of the molecule [51].

Methane [CH_4] (Fig. 1.7) is one of the simplest polyatomic molecules that exist. This system has important applications in technological fields, such as in plasma enhanced chemical vapor deposition [52, 53]. It is also an important prebiotic molecule, which is widely distributed in the interstellar medium [54, 55]. Additionally, methane is a potent greenhouse gas in the Earth's atmosphere contributing to global warming [56].

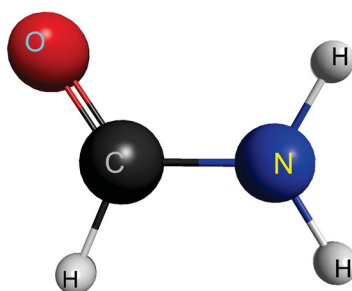


Figure 1.6 – Schematic representation of the chemical structure of formamide (generated with MacMolPlt [35]).

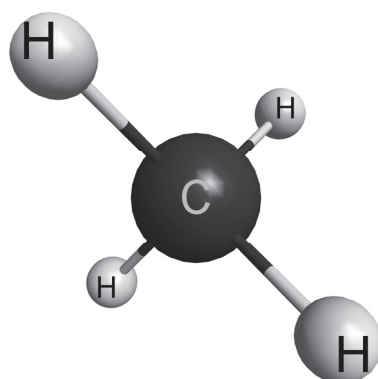


Figure 1.7 – Schematic representation of the chemical structure of methane (generated with MacMolPlt [35]).

Because of methane's simplicity and many applications, its interaction with electrons has been comprehensively investigated and a thorough survey of the literature can be found in the works of Fuss *et al.* [57], Song *et al.* [58] and Gadoum and Benyoucef [59]. The elastic scattering of electrons by methane generally shows a consensus, with most of the theoretical [60–66] and experimental [33, 67–69] data from the literature being in agreement. On the other hand, the knowledge on the electronically inelastic scattering of electrons is still not fully understood. In the literature, only a few electronically inelastic cross sections can be found [70–75]. These are mostly theoretical cross sections that due to computational constraints included only a few electronically excited states of the molecule in the calculations, and their results do not agree well among themselves [71–75]. This motivated us to revisit the scattering of electrons by methane, focusing on the electronic excitation of the molecule and in the inclusion of the multichannel coupling effects in the scattering calculations, involving a large number of electronically excited states.

This dissertation is organized as follows: In chapter 2 the theory and methods used to obtain the electron scattering cross sections are discussed. Then, the results for each molecule are going to be presented in separate chapters. The elastic, electronically inelastic, ionization and total electron scattering cross sections by formamide and methane are depicted and analyzed in chapters 3 and 4, respectively. Finally, the main conclusions derived from our results are presented in chapter 5. Additionally, appendix A contains the scientific contributions that resulted from our work, appendix B discusses the elastic electron scattering cross sections for dimethyl peroxide and ethylene glycol, appendix C presents additional details regarding the scattering calculations, and in appendix D some numerical values used in the calculations are tabulated.

CHAPTER 2

Theory

In this chapter the theory behind the scattering of electrons by molecules will be presented. In Sec. 2.1 we discuss basic concepts relevant to the study of electron scattering by molecular targets, such as the definition of cross section, the concept of scattering channels, the scattering amplitude and the scattering Hamiltonian. Then, the Schwinger multichannel (SMC) method and its characteristics will be presented in Sec. 2.2, including a thorough description of the different approximations in which the scattering calculations may be performed. This method was used to obtain the elastic and electronically inelastic electron scattering cross sections in the present dissertation. In Sec. 2.3 the binary-encounter-Bethe model, which was used to calculate the ionization cross sections, is presented. Finally, in Sec. 2.4 we explore the physical phenomena observed in the cross sections calculated in this work from a theoretically-oriented perspective. More precisely, the formation of shape resonances, the Ramsauer-Townsend minimum and the multichannel coupling effect are going to be discussed.

2.1 Basic concepts

The scattering problem consists of the collision between the particles of an incident beam and a target [76]. After this collision occurs, the scattered particles are captured by a detector outside the range of the interaction potential. In Fig. 2.1 a pictorial representation of the scattering process is presented. A beam of incident particles, labeled "A", is collimated and mono-energetic such that the incident particles have a well defined energy and do not interact amongst themselves. This beam is directed

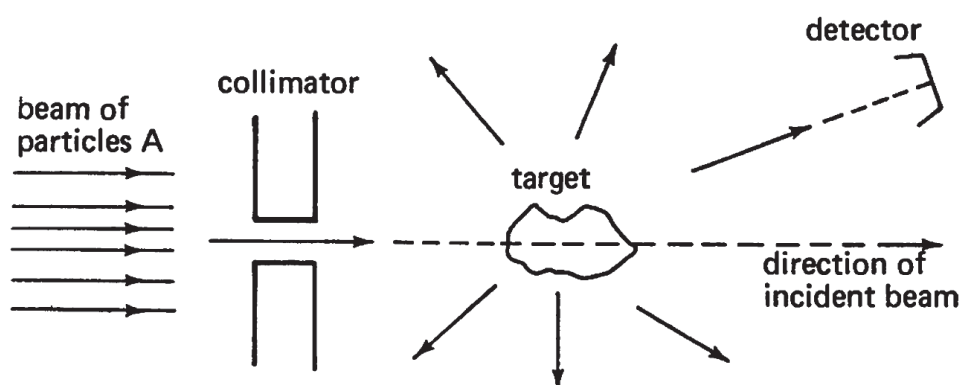


Figure 2.1 – An incident beam of particles "A" being scattered by a target composed of scattering centers "B". The scattered particles are detected outside the range of the interaction potential. Figure taken from Ref. [76].

towards a target composed of particles "B", called scattering centers. The distance between the particles "B" of the target can be taken to be larger than the de Broglie wavelength of the incident particles, such that coherence effects can be disregarded. Not only that, if the target is sufficiently thin, multiple scattering by several scattering centers can also be neglected. Thus, within these conditions that are experimentally achievable, the initial problem of a beam composed of many particles "A" being scattered by a target composed of many scattering centers "B" is reduced to the scattering of a single particle "A" by a single scattering center "B". In the present work, the incident beam "A" would be composed of electrons, while the target consists of a gas composed of molecules of interest.

The scattering process may have several distinct outcomes, each of which is denominated scattering channel. In the elastic channel, the incident particle and the target do not exchange energy during the scattering process, such that the final and initial states of the collision are equal. In the inelastic channels, the target molecule is electronically, vibrationally and/or rotationally excited by the incoming electron. These excitations can only occur if the energy conservation law, given by

$$E = E_i + \frac{k_i^2}{2} = E_f + \frac{k_f^2}{2}, \quad (2.1)$$

is respected. In the equation above E is the collision energy, $E_{i(f)}$ is the initial (final) energy of the target and $\vec{k}_{i(f)}$ is the initial (final) linear momentum of the incident particle. A channel can only be treated as open in the scattering calculation if equation (2.1) is respected, otherwise the channel is treated as closed and not accessible through the scattering process. Furthermore, the molecule may be ionized or dissociate into fragments due to the interaction with the incident electron. These channels are related to reaction scattering channels, where the species present in the initial and final states differ [76].

Each scattering channel is related to a cross section, which is the physical

quantity that contains all the information about the scattering process. Therefore, to study the interaction between electrons and molecules one needs to find the cross sections of interest. The differential cross section (DCS) for a given channel is defined as the ratio of the number of scattered particles per unit time associated with that channel (dn_f) within a solid angle ($d\Omega$), to the incident flux of particles (F_i):

$$\frac{d\sigma_f}{d\Omega}(k; \theta, \phi) = \frac{dn_f}{F_i d\Omega}. \quad (2.2)$$

Since the interaction between the incident electron and the molecule depends on the energy and the scattering angle, the DCS should also depend on the same quantities. This is reflected on the dependence of $d\sigma_f/d\Omega$ on k , θ and ϕ in the equation above. From the DCS, one can find the integral cross section (ICS) through

$$\sigma_f(k) = \int d\Omega \frac{d\sigma_f}{d\Omega}(k; \theta, \phi), \quad (2.3)$$

which gives a more general description of the scattering process since it does not carry the angular dependence of the DCS. The cross sections can be interpreted both as a relative probability of a specific interaction to occur and as an effective area of the target seen by the incident particle that participates in the scattering process [76]. Additionally, the momentum transfer cross section (MTCS)

$$\sigma_f^{\text{MTCS}}(k) = \int d\Omega (1 - \cos \theta) \frac{d\sigma_f}{d\Omega}(k; \theta, \phi) \quad (2.4)$$

gives a useful description about the momentum transferred from a particle when it collides with a target, disregarding angular dependencies. The angular information about the scattering process is used in the MTCS computation, where the term $(1 - \cos \theta)$ makes the higher scattering angles (higher momentum transferred) contributes more to the integration than the lower scattering angles (lower momentum transferred).

The interest of the present work is the interaction between electrons and molecules. Thus, our aim is to find the cross sections for the electron scattering by molecules. In a system composed of the incident electron and a molecule with N electrons and M nuclei, the time independent scattering Hamiltonian (H_{N+1}), in atomic units¹, can be written as

$$H_{N+1} = H_N + T_{N+1} + V = H_0 + V \quad (2.5)$$

where H_0 is the unperturbed Hamiltonian constructed as the sum of the electronic Hamiltonian of the target molecule within the Born-Oppenheimer approximation, H_N , and the kinetic energy operator of the incident electron, T_{N+1} . V is the interaction potential between the incident electron and the target. These operators are defined as

$$H_N = \sum_{i=1}^N -\frac{\nabla_i^2}{2} + \sum_{i=1}^N \sum_{A=1}^M -\frac{Z_A}{|\vec{r}_i - \vec{R}_A|} + \sum_{i=1}^N \sum_{j>i}^N \frac{1}{|\vec{r}_i - \vec{r}_j|}, \quad (2.6)$$

¹ $\hbar = m_e = e = 4\pi\epsilon_0 = 1$

$$T_{N+1} = -\frac{\nabla_{N+1}^2}{2} \quad (2.7)$$

and

$$V = \sum_i^N \frac{1}{|\vec{r}_{N+1} - \vec{r}_i|} - \sum_{A=1}^M \frac{Z_A}{|\vec{r}_{N+1} - \vec{R}_A|} \quad (2.8)$$

where \vec{r}_{N+1} is the position of the incident electron, Z_A and \vec{R}_A are the atomic number and position of the molecular nuclei A and \vec{r}_i is the coordinated of the i th molecular electron.

As mentioned before, in equation (2.6) the molecular Hamiltonian H_N is written within the Born-Oppenheimer approximation. In this approximation the nuclei are treated as static objects since their mass is much larger than the mass of the electrons that compose the molecule. As a consequence, the kinetic energy of the nuclei is zero and the interaction potential between nuclei is a constant that can later be summed to the electronic energy. All theoretical development from this point forward will be done assuming this approximation. The first term of the molecular electronic Hamiltonian presented in equation (2.6) is the kinetic energy of the electrons, the second term is the electron-nuclei attractive potential and the last term is the electron-electron repulsive potential. The eigenstates of this Hamiltonian are obtained through the Hartree-Fock method [77], which gives the ground state of the molecular target $\Phi_1(\vec{r}_1, \dots, \vec{r}_N)$. The potential operator that represents the interaction between the incident electron and the molecular target given in equation (2.8) is the sum of the repulsive potential between the incident electron and the molecular electrons and the attractive potential between the incident electron and the nuclei.

The stationary scattering wave function $\Psi(\vec{r}_1, \dots, \vec{r}_{N+1})$ satisfies the Schrödinger equation

$$\hat{H}\Psi(\vec{r}_1, \dots, \vec{r}_{N+1}) = 0, \quad (2.9)$$

where $\hat{H} = E - H_{N+1}$ with E being the total energy of the collision, subjected to the asymptotic boundary condition [76]

$$\Psi_{\vec{k}_i}(\vec{r}_1, \dots, \vec{r}_{N+1}) \xrightarrow{r_{N+1} \rightarrow \infty} S_{\vec{k}_i}(\vec{r}_1, \dots, \vec{r}_{N+1}) + \sum_{f=1}^{N_{open}} f(\vec{k}_f, \vec{k}_i) \Phi_f(\vec{r}_1, \dots, \vec{r}_N) \frac{e^{ik_f r_{N+1}}}{r_{N+1}} \quad (2.10)$$

where i and f indicates the initial and final states of the system, respectively. Each final state is associated with a different scattering channel, and the sum on the second term of the equation above runs over the N_{open} possible accessible channels. Note that these N_{open} channels have to respect equation (2.1) and that this boundary condition is only valid outside the range of the interaction potential ($r_{N+1} \rightarrow \infty$).

The first term in equation (2.10), $S_{\vec{k}_i}(\vec{r}_1, \dots, \vec{r}_{N+1})$, is written as a product of a molecular state $\Phi_i(\vec{r}_1, \dots, \vec{r}_N)$ and a plane wave $e^{i\vec{k}_i \cdot \vec{r}_{N+1}}$

$$S_{\vec{k}_i}(\vec{r}_1, \dots, \vec{r}_{N+1}) = \Phi_i(\vec{r}_1, \dots, \vec{r}_N) e^{i\vec{k}_i \cdot \vec{r}_{N+1}} \quad (2.11)$$

which is the solution of the unperturbed Hamiltonian H_0 ($V = 0$ on equation (2.5))

$$H_0 S_{\vec{k}_i}(\vec{r}_1, \dots, \vec{r}_{N+1}) = \left[E_i + \frac{k_i^2}{2} \right] S_{\vec{k}_i}(\vec{r}_1, \dots, \vec{r}_{N+1}). \quad (2.12)$$

The second term in equation (2.10) is composed of a superposition of final states of the target after the scattering, $\Phi_f(\vec{r}_1, \dots, \vec{r}_N)$, and the spherical waves, $\frac{e^{ik_f r_{N+1}}}{r_{N+1}}$, modulated by a function $f(\vec{k}_f, \vec{k}_i)$, denominated scattering amplitude. The boundary condition given in equation (2.10) comes from a simple interpretation about the scattering process: firstly the system is formed by a free particle, which is the incoming electron (plane wave), and the molecular target is in an initial state. After the collision occurs, the molecule is left on a given final state and the scattered electron is represented by an outgoing spherical wave modulated by the scattering amplitude. In this way, all information about the scattering process is stored in the scattering amplitude $f(\vec{k}_f, \vec{k}_i)$. In fact, it can be shown [76] that this quantity is directly related to the differential cross section by

$$\frac{d\sigma}{d\Omega}(k_f, k_i; \theta, \phi) = \frac{k_f}{k_i} |f(\vec{k}_f, \vec{k}_i)|^2. \quad (2.13)$$

Therefore, to study how electrons interact with molecules one need to calculated the scattering amplitudes of interest and through equation (2.13) obtain the relevant cross sections. In the present work, the amplitudes for the elastic and electronically inelastic channels were calculated through the Schwinger multichannel method. For the ionization cross sections, the BEB model was used. In what follows, both these methods are going to be discussed.

2.2 The Schwinger Multichannel Method

The Schwinger multichannel method (SMC) [31, 32, 78–81] is an extension of the Schwinger variational principle [82] for the scattering of low-energy electrons and positrons by molecules. It is a variational approach to obtain the scattering amplitudes of interest. In this section we will derive the expression for the scattering amplitude used in the SMC method and discuss the approximations used to perform the scattering calculations. Hereafter, we will focus only on the scattering of electrons by molecules, since the scattering of positrons by molecules is not in the scope of the present work.

2.2.1 Scattering Amplitude

The general solution of the Schrödinger equation is given as a sum of the solution of the unperturbed Hamiltonian H_0 with a particular solution obtained through the

Green's function method. This solution is known as the Lippmann-Schwinger equation which, in bra-ket notation, is given by [76]

$$|\Psi_{\vec{k}_{i,f}}^{(\pm)}\rangle = |S_{\vec{k}_{i,f}}\rangle + G_0^{(\pm)}V|\Psi_{\vec{k}_{i,f}}^{(\pm)}\rangle, \quad (2.14)$$

where $|S_{\vec{k}_{i,f}}\rangle$ corresponds to an eigenstate of the unperturbed Hamiltonian H_0 which, if projected in the coordinate space, gives

$$\langle \vec{r}_1, \dots, \vec{r}_N, \vec{r}_{N+1} | S_{\vec{k}_{i,f}} \rangle = \Phi_{\vec{k}_{i,f}}(\vec{r}_1, \dots, \vec{r}_N) e^{i\vec{k}_{i,f} \cdot \vec{r}_{N+1}}. \quad (2.15)$$

$G_0^{(\pm)}$ is the free-particle Green's operator given by

$$G_0^{(\pm)} = \lim_{\epsilon \rightarrow 0} (E - H_0 \pm i\epsilon)^{-1}; \quad (2.16)$$

and V is the interaction potential given in equation (2.8). The indexes (\pm) are associated with two distinct forms of the scattering wave function $|\Psi_{\vec{k}_{i,f}}^{(\pm)}\rangle$ in the asymptotic region. The $(+)$ case corresponds to an incident plane wave that has a linear momentum \vec{k}_i summed to an outgoing spherical wave, while the $(-)$ case is associated with the sum of an incoming spherical wave with momentum \vec{k}_i and a scattered plane wave with linear momentum \vec{k}_f . Although only the $(+)$ case gives the correct physical interpretation of the scattering problem, both solutions are mathematically possible.

Projecting equation (2.14) into the coordinates space, analyzing its behaviour in the asymptotic region and considering that it is subject to the asymptotic condition given in equation (2.10) the scattering amplitude can be written as [76]

$$f(\vec{k}_f, \vec{k}_i) = -\frac{1}{2\pi} \langle S_{\vec{k}_f} | V | \Psi_{\vec{k}_i}^{(+)} \rangle \quad (2.17)$$

and

$$f(\vec{k}_f, \vec{k}_i) = -\frac{1}{2\pi} \langle \Psi_{\vec{k}_f}^{(-)} | V | S_{\vec{k}_i} \rangle, \quad (2.18)$$

depending on the sign chosen for the asymptotic condition.

Acting on equation (2.14) with the interaction potential through the left side and rearranging the terms one obtains

$$A^{(\pm)} |\Psi_{\vec{k}_{i,f}}^{(\pm)}\rangle = V |S_{\vec{k}_{i,f}}\rangle \quad (2.19)$$

where

$$A^{(\pm)} = V - VG_0^{(\pm)}V. \quad (2.20)$$

Substituting equation (2.19) into equation (2.18) a third expression for the scattering amplitude is found

$$f(\vec{k}_f, \vec{k}_i) = -\frac{1}{2\pi} \langle \Psi_{\vec{k}_f}^{(-)} | A^{(+)} | \Psi_{\vec{k}_i}^{(+)} \rangle, \quad (2.21)$$

which combined with equations (2.17) and (2.18) leads to the functional expression of the scattering amplitude

$$\left[f(\vec{k}_f, \vec{k}_i) \right] = -\frac{1}{2\pi} \left[\langle S_{\vec{k}_f}^- | V | \Psi_{\vec{k}_i}^{(+)} \rangle + \langle \Psi_{\vec{k}_f}^{(-)} | V | S_{\vec{k}_i}^- \rangle - \langle \Psi_{\vec{k}_f}^{(-)} | A^{(+)} | \Psi_{\vec{k}_i}^{(+)} \rangle \right]. \quad (2.22)$$

An important property of the operator $A^{(\pm)}$ can be derived from the functional given in equation (2.22). This functional has to be stationary upon arbitrary variations of the scattering wave function. Thus, perturbations of the first order in the kets and bras

$$\begin{aligned} |\bar{\Psi}_{\vec{k}_i}^{(+)}\rangle &= |\Psi_{\vec{k}_i}^{(+)}\rangle + |\delta\Psi_{\vec{k}_i}^{(+)}\rangle \\ \langle\bar{\Psi}_{\vec{k}_f}^{(-)}| &= \langle\Psi_{\vec{k}_f}^{(-)}| + \langle\delta\Psi_{\vec{k}_f}^{(-)}| \end{aligned} \quad (2.23)$$

lead to

$$\delta \left[f(\vec{k}_f, \vec{k}_i) \right] = -(2\pi)^2 \langle\delta\Psi_{\vec{k}_f}^{(-)}| \left[V | S_{\vec{k}_i}^- \rangle - A^{(+)} | \Psi_{\vec{k}_i}^{(+)} \rangle \right] - (2\pi)^2 \left[\langle S_{\vec{k}_f}^- | V - \langle \Psi_{\vec{k}_f}^{(-)} | A^{(+)} \right] \delta\Psi_{\vec{k}_i}^{(+)} = 0, \quad (2.24)$$

and thus it is necessary that

$$\begin{aligned} V | S_{\vec{k}_i}^- \rangle - A^{(+)} | \Psi_{\vec{k}_i}^{(+)} \rangle &= 0 \\ \langle S_{\vec{k}_f}^- | V - \langle \Psi_{\vec{k}_f}^{(-)} | A^{(+)} &= 0. \end{aligned} \quad (2.25)$$

The first equation above is simply equation (2.19) with the (+) sign. Taking the Hermitian conjugate of the second equation we obtain

$$V | S_{\vec{k}_f}^- \rangle - [A^{(+)}]^\dagger | \Psi_{\vec{k}_f}^{(-)} \rangle = 0 \quad (2.26)$$

and since this equation and equation (2.19) with the (−) sign have to simultaneously be true, the operators $A^{(\pm)}$ have to respect

$$[A^{(+)}]^\dagger = A^{(-)}. \quad (2.27)$$

Now, expanding the scattering wave function in a known basis set $\{|\chi_m\rangle\}$, such that

$$|\Psi_{\vec{k}_i}^{(+)}\rangle = \sum_m a_m^{(+)}(\vec{k}_i) |\chi_m\rangle \quad (2.28)$$

and

$$\langle\Psi_{\vec{k}_f}^{(-)}| = \sum_n a_n^{(-)*}(\vec{k}_f) \langle\chi_n|. \quad (2.29)$$

With this, the coefficients $a_m^{(+)}$ and $a_n^{(-)*}$ are variational parameters. Using equations (2.28) and (2.29) in the functional expression of the variational amplitude given in equation (2.22), and imposing variational stability in the first order, one obtain

$$a_m^{(+)}(\vec{k}_i) = \sum_n (d^{-1})_{mn} \langle\chi_n | V | S_{\vec{k}_i}^- \rangle \quad (2.30)$$

and

$$a_n^{(-)*}(\vec{k}_f) = \sum_m (d^{-1})_{mn} \langle S_{\vec{k}_f} | V | \chi_m \rangle \quad (2.31)$$

where

$$d_{mn} = \langle \chi_m | A^{(+)} | \chi_n \rangle. \quad (2.32)$$

This allows the scattering amplitude to be written as

$$f(\vec{k}_f, \vec{k}_i) = -\frac{1}{2\pi} \sum_m \sum_n \langle S_{\vec{k}_f} | V | \chi_m \rangle (d^{-1})_{mn} \langle \chi_n | V | S_{\vec{k}_i} \rangle. \quad (2.33)$$

Although all calculations done so far are correct, an important detail was not considered. Since we are dealing with the scattering of an electron by a molecular target the incident particle is indistinguishable from the electrons of the target molecule. Thus, $|\Psi_{\vec{k}_i, f}^{(\pm)}\rangle$, and consequentially the right side of equation (2.14), has to be antisymmetric. It was shown that for this to be true, in addition to the discrete states of the molecular target the continuum states also have to be included in the Green's function $G_0^{(\pm)}$ [83]. Hence, equation (2.16) has to be rewritten in the basis set composed of H_0 eigenstates. This is possible through the use of the closure relation

$$\mathbb{1}_{H_0} = \sum_n' \int d^3k |\Phi_n \vec{k}\rangle \langle \Phi_n \vec{k}| \quad (2.34)$$

where $|\Phi_n \vec{k}\rangle$ are the eigenstates of H_0

$$H_0 |\Phi_n \vec{k}\rangle = \left[E_n + \frac{k^2}{2} \right] |\Phi_n \vec{k}\rangle \quad (2.35)$$

and

$$\sum_n' \quad (2.36)$$

represents the summation over all discrete states and the integration over continuum states of the molecule. Then, the Green's function may be written as

$$G_0^{(\pm)} = \lim_{\epsilon \rightarrow 0} \sum_n' \int d^3k \frac{|\Phi_n \vec{k}\rangle \langle \Phi_n \vec{k}|}{E - E_n - \frac{k^2}{2} \pm i\epsilon} \quad (2.37)$$

or, since $E = E_n + \frac{k_n^2}{2}$,

$$G_0^{(\pm)} = \lim_{\epsilon \rightarrow 0} \sum_n' \int d^3k \frac{|\Phi_n \vec{k}\rangle \langle \Phi_n \vec{k}|}{\frac{k_n^2}{2} - \frac{k^2}{2} \pm i\epsilon}. \quad (2.38)$$

The continuum states representing ionization channels would lead to a long-ranged potential, not properly described by the boundary condition given in equation (2.10). Additionally, handling an infinite number of continuum states is computationally impossible. To deal with these problems, we introduce a projector operator P , constructed as

$$P = \sum_{f=1}^{N_{open}} |\Phi_f\rangle \langle \Phi_f| \quad (2.39)$$

responsible for projecting the wave function onto the space composed of N_{open} discrete states of the molecular target. In the case of elastic calculations, only the ground state $|\Phi_1\rangle$ of the target is included in the construction of the projector. In the case where electronically inelastic channels are included in the scattering calculations, the projector is enlarged from the elastic case to also include electronically excited states of the molecule. This projector defines the open-channel space in the scattering calculations, that is, the space composed of all electronic states of the molecule that are accessible during the scattering process.

The Lippmann-Schwinger equation (2.14) projected onto the P -space is written as

$$P|\Psi_{\vec{k}_{i,f}}^{(\pm)}\rangle = |S_{\vec{k}_{i,f}}\rangle + G_P^{(\pm)}V|\Psi_{\vec{k}_{i,f}}^{(\pm)}\rangle, \quad (2.40)$$

where $G_P^{(\pm)} = PG_0^{(\pm)}$ is the Green's operator projected onto the open channel space defined by P :

$$G_P^{(\pm)} = \lim_{\epsilon \rightarrow 0} \sum_f^{N_{open}} \int d^3k \frac{|\Phi_f \vec{k}\rangle \langle \Phi_f \vec{k}|}{\frac{k_f^2}{2} - \frac{k^2}{2} \pm i\epsilon}. \quad (2.41)$$

Although this projection solves the previous problem related to the continuum states of the Green's function, it has a shortcome. Applying the potential V through the left on equation (2.40) we find

$$A^{(\pm)}|\Psi_{\vec{k}_{i,f}}^{(\pm)}\rangle = V|S_{\vec{k}_{i,f}}\rangle \quad (2.42)$$

such that now the operators $A^{(\pm)}$ becomes

$$A^{(\pm)} = VP - VG_P^{(\pm)}V \quad (2.43)$$

which no longer respect the condition given in equation (2.27), since VP is not necessarily Hermitian. To solve this we, recover the information contained in the complementary space of P lost upon projection, and then obtain a new expression for the operator $A^{(+)}$ that satisfies equation (2.27) [84]. A projector onto the complementary space of P can be defined as $(\mathbb{1} - aP)$, where a will be chosen latter. Therefore, the wave function can be written as

$$|\Psi_{\vec{k}_i}^{(+)}\rangle = aP|\Psi_{\vec{k}_i}^{(+)}\rangle + (\mathbb{1} - aP)|\Psi_{\vec{k}_i}^{(+)}\rangle \quad (2.44)$$

which satisfies the Schrödinger equation

$$\hat{H}|\Psi_{\vec{k}_i}^{(+)}\rangle = 0. \quad (2.45)$$

Using the Lippmann-Schwinger equation (2.40) projected onto the P -space and equation (2.44) we obtain

$$\hat{H} \left[a(|S_{\vec{k}_i}\rangle + G_P^{(+)}V|\Psi_{\vec{k}_i}^{(+)}\rangle) + (\mathbb{1} - aP)|\Psi_{\vec{k}_i}^{(+)}\rangle \right] = 0 \quad (2.46)$$

that, with [84]

$$\begin{aligned} [H_0, P] &= 0, \\ \hat{H}P|\Psi_{\vec{k}_i}^{(+)}\rangle &= \frac{1}{2}[(E - H_0)P + P(E - H_0)]|\Psi_{\vec{k}_i}^{(+)}\rangle - VP|\Psi_{\vec{k}_i}^{(+)}\rangle \end{aligned} \quad (2.47)$$

and after some mathematical manipulations leads to

$$A^{(+)}|\Psi_{\vec{k}_i}^{(+)}\rangle = V|S_{\vec{k}_i}\rangle \quad (2.48)$$

where the new form of the operator $A^{(+)}$ is

$$A^{(+)} = \frac{1}{2}(PV + VP) - VG_P^{(+)}V + \frac{1}{a} \left[\hat{H} - \frac{a}{2}(\hat{H}P + P\hat{H}) \right]. \quad (2.49)$$

The operator $A^{(+)}$ in the equation above almost satisfies equation (2.27). However, there is an issue with the operator T_{N+1} contained within \hat{H} : it couples the continuum functions that describe the scattered electron, causing \hat{H} to lose its Hermiticity. To address this issue and ensure that equation (2.27) is satisfied, we need to guarantee that

$$\frac{1}{a} \left[\hat{H} - \frac{a}{2}(\hat{H}P + P\hat{H}) \right] \quad (2.50)$$

is Hermitian, that is,

$$\langle \Psi_{\vec{k}_f}^{(-)} | \frac{1}{a} \left[\hat{H} - \frac{a}{2}(\hat{H}P + P\hat{H}) \right] | \Psi_{\vec{k}_i}^{(+)} \rangle = \langle \Psi_{\vec{k}_i}^{(+)} | \frac{1}{a} \left[\hat{H} - \frac{a}{2}(P\hat{H} + \hat{H}P) \right] | \Psi_{\vec{k}_f}^{(-)} \rangle. \quad (2.51)$$

One way to ensure this is if both sides of the equation above vanish for a specific choice of a , that is,

$$\langle \Psi_{\vec{k}_f}^{(-)} | \frac{1}{a} \left[\hat{H} - \frac{a}{2}(\hat{H}P + P\hat{H}) \right] | \Psi_{\vec{k}_i}^{(+)} \rangle = 0. \quad (2.52)$$

This was shown to happen if $a = N + 1$ [31, 79], ensuring that the operator presented in equation (2.50) is Hermitian and, consequentially, the validity of equation (2.27) is secured.

In this way, the final form of the scattering amplitude is given by

$$f(\vec{k}_f, \vec{k}_i) = -\frac{1}{2\pi} \sum_{m,n} \langle S_{\vec{k}_f} | V | \chi_m \rangle (d^{-1})_{mn} \langle \chi_n | V | S_{\vec{k}_i} \rangle, \quad (2.53)$$

where

$$d_{mn} = \langle \chi_m | A^{(+)} | \chi_n \rangle \quad (2.54)$$

and

$$A^{(+)} = \frac{1}{2}(PV + VP) - VG_P^{(+)}V + \frac{1}{N+1} \left[\hat{H} - \frac{N+1}{2}(\hat{H}P + P\hat{H}) \right]. \quad (2.55)$$

There are a couple of important points that should be noted about this expression of the scattering amplitude. Firstly, note that the wave function always appears multiplied by the potential V (equations (2.17), (2.18) and (2.21)). In addition to that, the asymptotic

boundary condition is contained in the Green's function. As a consequence, the scattering wave function is not subjected to the boundary condition and the basis functions only need to describe the scattering within the range of the potential. These enable the use of square integrable functions (L^2), such as Cartesian Gaussian functions (CGs), as a single-particle basis set for the scattering calculations, greatly reducing the computational cost, since all integrals can be evaluated analytically. The only exception is the term involving the operator $VG_P^{(+)}V$, which is evaluated with a numerical quadrature. This approach avoids the use of very large basis sets in the scattering calculations due to the slow convergence of the matrix elements of the operator $VG_P^{(+)}V$ [85]. Despite the computational advantages, the use of CG functions has a shortcoming: since these are short-ranged functions, the long-ranged interactions are poorly described. Thus, when a molecule has a permanent dipole moment, the Born-closure procedure is employed to correct the cross section for the long-ranged electron-dipole interactions. This procedure is described in appendix C.1. Another strategy to reduce the computational cost of the scattering calculations is the use of *norm-conserving* pseudopotentials of Bachelet, Hamann and Schlüter (BHS) [86] to represent the core electrons and nuclei of the molecule, which is discussed in appendix C.2. The implementation of these pseudopotentials was done by Bettega, Ferreira and Lima [87, 88], and the method itself is now denominated as Schwinger multichannel method implemented with pseudopotentials (SMCPP). This version of the method was used in all calculations presented in this work. Finally, note that the scattering amplitude given in equation (2.53) is calculated in the reference frame of the molecule. Thus, in order to compare the calculated cross sections with the experimental results measured in the laboratory-frame, we need to perform a frame transformation. This is discussed in appendix C.3. It is also worth noting that the present calculations were performed with the current parallel implementation of the SMCPP code [89].

2.2.2 Approximation Level

The distinct levels of approximation in which the scattering calculations can be performed through the SMCPP method will be discussed in details in this section. Additionally, the strategy used to describe the electronically excited states of the target for the multichannel coupling calculations is also presented.

The scattering calculation can be performed in two distinct levels: the elastic and multichannel coupling approximations. In the former, the molecule remains in the ground state during the scattering process, such that only the elastic channel is treated as open in the scattering calculations. In the latter, the molecule is allowed to be electronically excited by the incident electron and electronically inelastic channels are now accessible during the scattering process. Furthermore, the elastic calculations can be performed

in two distinct approximations, the static-exchange (SE) and the static-exchange plus polarization (SEP) approximations. All these approximations are related to how the projector operator P , given in equation (2.39), and how the basis set used for the scattering calculation, given by the set $\{|\chi_m\rangle\}$ in equation (2.53), are constructed. Each $|\chi_m\rangle$ that composes the basis set is called a configuration state function (CSF) and it is constructed as the antisymmetrized product of a target state and a function that represents the continuum electron. The set $\{|\chi_m\rangle\}$ is also called configuration space, since it contains the CSFs used in the scattering calculations. In this section, we will discuss these distinct approximations in detail.

2.2.2.1 Elastic approximation

The SE approximation is the simplest approximation in which the scattering calculations can be performed. In this approximation the molecule remains in the ground state, such that the open-channel space is solely composed by the elastic channel. This level of calculation takes in consideration only the static potential from the Coulomb interaction between the incident electron and the electrons and nuclei of the molecule, and the exchange effects that emerge from the antisymmetrization of the wave function due to the indistinguishability between the incident electron and the molecular electrons. The polarization effects, that is, the relaxation of the molecular electronic cloud due to the incident electron, is completely omitted in this level of calculation. Consequently, this approximation is reliable for the qualitative description of the scattering at high impact energies, usually higher than 10 eV, since in this regime the interaction time between the incident electron and the target is small enough that the molecular cloud does not have enough time to relax due to the incident electron. For lower impact energies the interaction time increases and polarization effects become more relevant in the scattering process. Typical collision times range from around 1×10^{-16} s at 1 eV to 2×10^{-17} s at 30 eV [79]. Thus, the SE approximation does not give the most reliable description of the scattering in the low-energy regime. Additionally, since only the elastic channel is treated as open in this approximation, the quantitative description of the scattering at higher impact energies is harmed due to the absence of the multichannel coupling effect (that will be discussed in detail in Sec. 2.4.3).

In this approximation, the projector P is constructed as

$$P = |\Phi_1\rangle\langle\Phi_1| \quad (2.56)$$

where $|\Phi_1\rangle$ is the ground state of the molecule, obtained with the Hartree-Fock method. For the discussion that follows, it is important to remember that in the Hartree-Fock method the ground state wave function is given by a single Slater determinant, that is

$$\langle\vec{x}_1, \dots, \vec{x}_N|\Phi_1\rangle = \Phi_1(\vec{x}_1, \vec{x}_2, \dots, \vec{x}_N) \quad (2.57)$$

and

$$\Phi_1(\vec{x}_1, \vec{x}_2, \dots, \vec{x}_N) = \frac{1}{\sqrt{N!}} \begin{vmatrix} \chi_1(\vec{x}_1) & \chi_2(\vec{x}_1) & \cdots & \chi_a(\vec{x}_1) & \cdots & \chi_N(\vec{x}_1) \\ \chi_1(\vec{x}_2) & \chi_2(\vec{x}_2) & \cdots & \chi_a(\vec{x}_2) & \cdots & \chi_N(\vec{x}_2) \\ \vdots & \vdots & \vdots & \vdots & \ddots & \vdots \\ \chi_1(\vec{x}_N) & \chi_2(\vec{x}_N) & \cdots & \chi_a(\vec{x}_N) & \cdots & \chi_N(\vec{x}_N) \end{vmatrix} \quad (2.58)$$

where $\frac{1}{\sqrt{N!}}$ is a normalization factor and $\chi_i(\vec{x}_i)$ are molecular spin-orbitals written as

$$\chi_i(\vec{x}) = \begin{cases} \psi_i(\vec{r})\alpha(\omega) \\ \text{or} \\ \psi_i(\vec{r})\beta(\omega), \end{cases} \quad (2.59)$$

where \vec{x} includes both spatial (\vec{r}) and spin (ω) coordinates, α (β) represents an electron with spin up (down) and $\psi(x_i, y_i, z_i)$ are spacial orbitals written as a linear combination of atomic orbitals

$$\psi_i = \sum_{\mu} c_{\mu i} \zeta_{\mu}. \quad (2.60)$$

The atomic orbitals ζ_{μ} are expanded in a set of Cartesian Gaussian (CG) functions. These functions are centered at the coordinates of a given atom A of the molecule ($\vec{R}_A = (X_A, Y_A, Z_A)$) and have the form

$$\lambda_{lmn}^{\alpha} = N_{lmn} (x - X_A)^l (y - Y_A)^m (z - Z_A)^n e^{-\alpha|\vec{r} - \vec{R}_A|^2} \quad (2.61)$$

where α is the exponent of the Gaussian function and the sum $l + m + n$ gives the type of the CG function, such that if this sum is equal to 0, 1, or 2, the CG function corresponds to an s , p , or d function, respectively. Note that, as discussed before, the use of CGs function enables all integrals in equation (2.53) to be evaluated analytically.

In the SE approximation, the CSFs are constructed as

$$|\chi_m\rangle = \mathcal{A}|\Phi_1\rangle \otimes |\varphi_m\rangle \quad (2.62)$$

where $|\varphi_m\rangle$ is the scattering orbital that represents the incoming electron and \mathcal{A} is the antisymmetrization operator of $N + 1$ electrons. In this approximation, the scattering orbitals are the virtual orbitals (VOs) of the molecule obtained from the Hartree-Fock calculation, which are directly orthogonal to the occupied molecular orbitals of the Slater determinant $|\Phi_1\rangle$.

Another important aspect of the SE approximation is that it is the least computationally expensive calculation. Since only the ground state is included in the construction of the projector P , only the scattering amplitudes for the elastic channels are calculated. Furthermore, since the number of CSFs is equal to the number of VOs of the molecule, usually ranging from 70 VOs for small molecules up to a couple hundred VOs for bigger

molecules, the matrices that need to be evaluated in equation (2.53) are relatively small and computationally easy to deal with.

In the SEP approximation, the molecular electronic cloud is allowed to relax due to the presence of the incident electron. In turn, the description of the scattering process in the low-energy regime (< 10 eV) is improved in relation to the SE approximation, since the polarization effect is especially important for low-impact energies.

In this level of calculation the projector P is also written as in equation (2.56), where only the elastic channels is treated as open. However, the configuration space is enlarged in comparison to the SE approximation through the inclusion of CSFs constructed as

$$|\chi_m\rangle = \mathcal{A}|\Phi_a^r\rangle \otimes |\varphi_n\rangle \quad (2.63)$$

where $|\Phi_a^r\rangle$ are N -electron Slater determinants obtained by performing single (virtual) excitations of the target from an occupied (hole) spin orbital χ_a to an unoccupied (particle) spin orbital χ_r . More explicitly, $\langle \vec{x}_1, \dots, \vec{x}_N | \Phi_a^r \rangle = \Phi_a^r(\vec{x}_1, \vec{x}_2, \dots, \vec{x}_N)$ such that

$$\Phi_a^r(\vec{x}_1, \vec{x}_2, \dots, \vec{x}_N) = \frac{1}{\sqrt{N!}} \begin{vmatrix} \chi_1(\vec{x}_1) & \chi_2(\vec{x}_1) & \cdots & \chi_r(\vec{x}_1) & \cdots & \chi_N(\vec{x}_1) \\ \chi_1(\vec{x}_2) & \chi_2(\vec{x}_2) & \cdots & \chi_r(\vec{x}_2) & \cdots & \chi_N(\vec{x}_2) \\ \vdots & \vdots & \vdots & \vdots & \ddots & \vdots \\ \chi_1(\vec{x}_N) & \chi_2(\vec{x}_N) & \cdots & \chi_r(\vec{x}_N) & \cdots & \chi_N(\vec{x}_N) \end{vmatrix}. \quad (2.64)$$

Note the substitution of χ_a in equation (2.58) for χ_r in the equation above. This single excitation can have two distinct spin couplings: singlets ($S = 0$) and triplets ($S = 1$), while we restrain the CSF to have a dublet spin coupling ($S = 1/2$) since the total spin of the scattering state must be conserved.

Historically, many criteria have been developed and applied for selecting the hole, particle and scattering orbitals used to construct CSFs in the SEP approximation. These range from selecting the n -lowest molecular orbitals as particle and scattering orbitals [90] limited by the computational capability available, to using only the resonant orbital to construct the configuration space [91], or employing a cut-off energy criteria [92]. The strategy used to construct the CSF space for each of the calculations presented in this dissertation is going to be discussed in the respective chapter of each molecule.

Although the SEP approximation provides an improved description of the electron-molecule interaction at low impact energies, it has two limitations: the virtual excitations generate pseudoresonances in the higher impact energy regime and the calculations becomes more expensive. Pseudoresonances are structures that appear in the cross section due to channels that are energetically accessible but treated as closed in the elastic approximation. To rectify this problem a more robust scattering calculation that includes inelastic scattering channels is necessary. The way in which we perform

these kind of calculations will be described in the next section. Additionally, since the configuration space is enlarged, the matrices that need to be evaluated are now larger in comparison to the SE approximation, which leads to more computationally expensive calculations².

2.2.2.2 Multichannel coupling approximation

In the approximations mentioned previously, only the elastic channel was included in the open-channel space. When polarization effects are included, the SEP approximation provides a good description of the scattering, both qualitatively and quantitatively, for impact energies below the first electronic excitation threshold of the molecule³. The approximation in which inelastic processes are taken into account in the scattering calculations will be denoted as the multichannel coupling (MC) approximation in this dissertation. For energies above the first electronic excitation threshold the incident electron may promote electronic excitations of the molecule, and the effects associated with these excitations need to be taken into account in the calculations to fully describe the scattering process. To do so, the projector operator P is now constructed as

$$P = \sum_{f=1}^{N_{open}} |\Phi_f\rangle\langle\Phi_f| \quad (2.65)$$

where $|\Phi_f\rangle$ is an electronic state of the molecule, being the ground state if $f = 1$ or an electronically excited state if $f > 1$; and the sum runs over all N_{open} accessible channels. Now, since the projector includes more than the elastic channel, an individual scattering amplitude is calculated for each of the possible electronically inelastic channels, increasing considerably the computational cost of the scattering calculations.

For impact energies higher than the ionization energy of the molecule the ionization channel is also energetically accessible. Although a complete description of the scattering process should include ionization, this is not implemented in the current version of the SMCPP method. Thus, this channel is omitted in the scattering calculation performed with the SMCPP method presented here.

The first step to perform a scattering calculation in the multichannel coupling approximation is to describe the possible final states of the molecule. The main challenge here is to properly describe these electronically excited states while maintaining a feasible computational cost for the scattering calculations. In the present work, these states are described by the minimal orbital basis for single configuration interaction

² Currently, for small molecules, the CSF space of a SE calculation contains something around 70 to 300 CSFs. For a SEP calculation this number increases to something in the thousands and tens of thousands.

³ This is true only within the Born-Oppenheimer approximation. Otherwise, vibrational and rotational excitation should also be taken into account above their respective thresholds.

(MOB-SCI) approach [93]. To understand this strategy it is important to remember some aspects of the Hartree-Fock method and of the configuration interaction (CI) technique [77].

The Hartree-Fock procedure yields not only the ground state Slater determinant, shown in equation (2.58), but also a set of unoccupied molecular orbitals. With those, one may construct singly-excited Slater determinants which represents the promotion of an electron from a hole to a particle orbital with a given spin coupling, such as the one presented in equation (2.64). However, the unoccupied orbitals obtained via Hartree-Fock method describes the movement of an electron in a field of N electrons, and are more suitable for describing the negative ion of the molecule rather than electronically excited states.

Thus, to obtain an improved description of electronically excited states, a new set of virtual unoccupied orbitals can be generated in the field of $(N - 1)$ electrons. These orbitals are known as improved virtual orbitals (IVOs) [94], and have been used in scattering calculations to incorporate electronic excitation of the target molecule in the past [71–73]. While IVOs can improve upon the Hartree-Fock description, they have limitations in accurately describing multiple electronically excited states simultaneously. IVOs are generated using a chosen hole orbital with a specific spin coupling, which means that electronically excited states associated with the promotion of electrons from other hole orbitals or with a different spin coupling than the one used to generate the IVOs are usually poorly described.

Because the scattering of the incident electron can excite the molecule to more than one electronically excited states, the IVO strategy may not be entirely suitable for describing the molecular target within the context of scattering calculations. To provide a more accurate description of these states, the configuration interaction technique (CI) [77] may be employed. In the CI technique, the molecular wave function is written as

$$|\Phi_{\text{CI}}\rangle = c_1|\Phi_1\rangle + \sum_{a;r} c_a^r|\Phi_a^r\rangle + \sum_{a<b;r<s} c_{ab}^{rs}|\Phi_{ab}^{rs}\rangle + \sum_{a<b<c;r<s<t} c_{abc}^{rst}|\Phi_{abc}^{rst}\rangle + \dots \quad (2.66)$$

where $|\Phi_1\rangle$ is the reference Slater determinant, obtained through the Hartree-Fock method, $|\Phi_a^r\rangle$ is a singly excited Slater determinant as given in equation (2.64), $|\Phi_{ab}^{rs}\rangle$ is a doubly excited Slater determinant and so on. In this way, the total CI wave function $|\Phi_{\text{CI}}\rangle$ is given as the linear combination of electronic configurations formed by excitations of the reference Slater determinant $|\Phi_1\rangle$ ⁴.

If all possible excitations are included in the expansion given in equation (2.66), the procedure is known as full configuration interaction (FCI). Although this gives the ex-

⁴ Note that when one diagonalizes the molecular Hamiltonian with this wave function different configuration couple among themselves ($\langle\Phi_{\text{CI}}|H_N|\Phi_{\text{CI}}\rangle$), hence the name "configuration interaction".

act molecular wave function within a given basis set, it is computationally very expensive. Even for small molecules with a small basis set the number of possible configurations needed to expand the FCI wave function makes the electronic structure calculations impossible. One way to bypass this problem is to truncate the expansion (2.66) such that only a few excitations are considered, lowering the number of configurations, leading to a feasible computational cost. Particularly, if only the first and second terms are included in the equation (2.66), that is, if only the reference and singly-excited Slater determinants are included in the CI expansion the procedure is called single configuration interaction (SCI).

In the SCI approximation the wave function is written as⁵

$$|\Phi_{\text{SCI}}\rangle = c_1|\Phi_1\rangle + \sum_{a;r} c_a^r |\Phi_a^r\rangle \quad (2.67)$$

and the Slater determinants and coefficients are the same as explained before. If all possible singly-excited Slater determinants are included in the expansion above, the procedure is called full-single configuration interaction (FSCI). Although the FSCI technique is viable for the electronic structure calculations of small molecules, it is not possible to perform electron scattering calculations where the molecular wave function is described within this approximation. The FSCI approximation leads to a large number of electronically excited states, and since an individual scattering amplitude need to be calculated for each possible channel in equation (2.53), the scattering calculations are computationally impossible to be performed.

To solve this problem, a reduced set of singly-excited Slater determinants is selected from the FSCI wave function in order to maintain a proper description of the first few electronically excited states, while lowering the computational cost in a way that makes the scattering calculations affordable. That is, the second term in equation (2.67) is truncated in a way that the most relevant Slater determinants for the description of the lower electronically excited states are maintained in the new expansion. This procedure was develop by da Costa *et al.* [93], and is known as the MOB-SCI approach.

The set of Slater determinants used in the MOB-SCI expansion is selected based on the coefficients obtained from a FSCI calculation. In practice, the first step is to obtain a set of IVOs [94] to represent the unoccupied molecular orbitals of the target. Then, a FSCI calculation is performed, that is, the molecular Hamiltonian (H_N) is diagonalized in the basis set of all possible singly-excited Slater determinants. This diagonalization yields both the ground state and electronically excited states. For each electronically excited state, a specific coefficient is obtained for each Slater determinant

⁵ Note that, due to Brillouin's theorem [77], the ground state does not couple with singly-excited states, thus $c_1 = 0$. However, in order to maintain consistency with equation (2.66), we include this term in equation (2.67).

from the basis set. Then, a subset of Slater determinants is selected in order to represent accurately the first few electronically excited states obtained from the FSCI calculation. This is done based on the coefficient of each Slater determinant obtained from the FSCI calculation. Slater determinants with coefficients whose squared modulus is large (close to one) have a significant contribution to the description of an electronically excited state. On the other hand, the contribution of Slater determinants with small coefficients is comparatively less relevant. Thus, we select only the Slater determinants with coefficients whose squared modulus are large for the MOB-SCI expansion.

To illustrate this procedure, suppose that we are interested only in a given electronically excited state α from an irreducible representation Γ , denoted as $|\Phi_{\text{FSCI}}^{(\Gamma,\alpha)}\rangle$. The expansion of this excited state after the FSCI procedure is given by⁶

$$|\Phi_{\text{FSCI}}^{(\Gamma,\alpha)}\rangle = \sum_{a;r} c_a^{r;(\Gamma,\alpha)} |\Phi_a^r\rangle. \quad (2.68)$$

To describe this state within the MOB-SCI approach we would look at the coefficients $c_a^{r;(\Gamma,\alpha)}$ and select only those whose modulus square is large (close to one). The amount of Slater determinants chosen is usually based on the computational capabilities available to perform the proceeding scattering calculations. Additional details about the MOB-SCI procedure, including a numerical example, may be found in appendix C.4.

After the electronically excited states of the molecule are described, we move forward to the scattering calculations. In this work, the configuration space used to perform the scattering calculations in the multichannel coupling approximation is constructed as

$$|\chi_m\rangle = \mathcal{A} |\Phi_a^r\rangle \otimes |\varphi_n\rangle \quad (2.69)$$

where $|\Phi_a^r\rangle$ is the same set of singly-excited Slater determinants used in the MOB-SCI expansion. \mathcal{A} and $|\varphi_n\rangle$ are the antisymmetrization operator and a scattering orbital, respectively. In contrast to previous work published in the literature, where the configurational space is enlarged by virtual excitation of the target (see, for instance, Ref. [95]), recent computational advances and optimization of the code enabled the inclusion of a relatively large amount of Slater determinants in the MOB-SCI expansion, such that this set of Slater determinants produces a large configuration space leading to a proper description of the polarization effects by itself, without the need to include further virtual excitations [51, 96]. This will be showed more clearly in the results section of each molecule, where the position of the shape resonance in the elastic channel obtained through a CSF space constructed in this manner is in good agreement with experimental data, indicating a good description of the polarization effects in the scattering calculations.

⁶ Note that the term related to the ground state is equal to zero due to Brillouin's theorem [77].

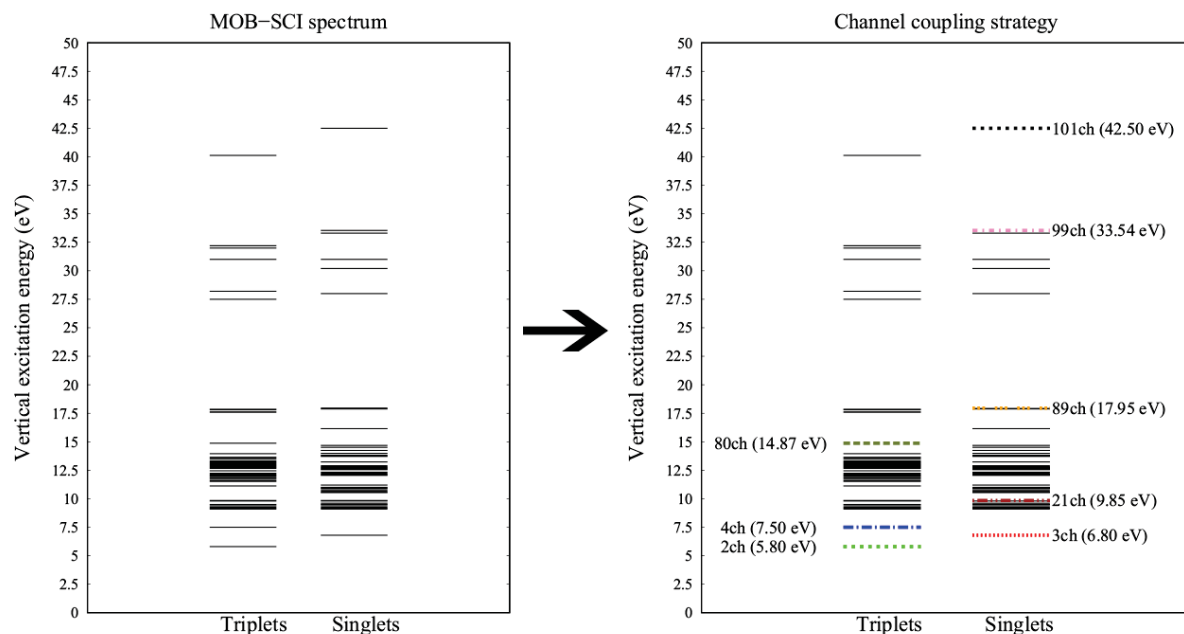


Figure 2.2 – (a) Schematic representation of vertical excitation energies of the electronically excited states of a fictitious molecule AB obtained through a MOB-SCI calculation. (b) Possible multichannel coupling strategy used in the scattering calculations. For more details, see the text.

As the incident electron energy increases, the molecule can be excited to an increasingly larger number of electronically excited states, due to the energy conservation law (2.1). Ideally, to accurately describe the scattering process, all energetically accessible states of the molecule for each impact energy should be included in the constructions of the projector P , given in equation (2.39). Consequentially, there would be as many distinct projectors P as there are energetically accessible channels, which would lead to as many distinct scattering calculations. For instance, suppose that for a given molecule AB a scattering calculation within the MOB-SCI approach is to be done. Suppose also that the MOB-SCI approach is performed with a set of 50 Slater determinants, such that there are 100 electronically excited states of the molecule included in the scattering calculations (50 triplets and 50 singlets). This MOB-SCI spectrum can be represented as in Fig. 2.2 (a), where each horizontal line is associated with a different electronically excited state. This calculation would be performed with a maximum of 101 open channels: the elastic channel, 50 channels associated with the excitation of the molecule to the 50 triplets states and 50 channels associated with the singlets. If all energetically accessible channels are treated as open in each impact energy, 101 distinct projectors P would be constructed, resulting in 101 distinct scattering calculations. Additionally, to distinguish between closely lying states, one would need a very fine energy grid. This is practically unattainable for most molecules.

To address this issue, we utilize a different channel coupling strategy. In practice,

we select from all possible projectors P the ones that better describe the scattering in selected energies. These projectors are chosen based on the availability of experimental data, the presence of closely lying states or to investigate the influence of an individual selected states of interest in the scattering process. Additionally, we may also choose projectors that lead to intermediate levels of calculation. In this way the amount of distinct scattering calculations associated with each projector P is reduced, making it computationally feasible, while trying to maintaining an optimal description of the scattering process throughout all impact energies.

Going back to the hypothetical case of molecule AB. Suppose that the vertical excitation energies obtained through the MOB-SCI strategy for the 100 electronically excited states of molecule AB are as given in Fig. 2.2 (a). Suppose also that in the literature there are experimental DCSs reported for this molecule at 10, 15 and 20 eV. A possible coupling strategy would be to select the projectors that lead to the levels of calculation shown in Fig. 2.2 (b). Each level of calculation is denoted by $N_{open}ch$, indicating that N_{open} channels are treated as open in that level of calculation. In our hypothetical scenario, the calculation performed with 2, 3 and 4 open channels (2ch, 3ch and 4ch) would be done to investigate how the opening of these low-lying electronically excited states influence the cross sections. The 21ch, 80ch and 89ch calculations would provide the result where all energetically accessible channels are treated as open in 10, 15 and 20 eV, respectively. These are the best results regarding channel coupling at the energies of the hypothetical experimental DCSs from the literature. Also, the calculations with 21 and 80 open channels comprise the closely lying states between 8 and 10 eV and 11 and 15 eV, respectively. The 99ch calculation would be done to open all closely lying states between 27.5 and 34 eV at once. Finally, the calculation at 101ch would treat all channels obtained within the MOB-SCI strategy as open in the scattering calculations (100 electronically inelastic channels plus the elastic channel). In this way, instead of performing 101 distinct scattering calculations, only 9 are performed: the calculation where only the elastic channels is treat as open and the 8 levels of calculation shown in Fig. 2.2 (b).

It is worth emphasizing that equation (2.1) must be respected in all calculations. Therefore, for each multichannel coupling scheme the incident electron impact energy must be above the threshold of the highest excited state within that level of calculation. For instance, for the 2ch calculation shown in Fig. 2.2 (b), the impact energy of the incident electron have to greater than 5.8 eV, so that the first electronically inelastic channel is energetically accessible during the scattering process.

The comparison between the calculated DCSs and the measured data is straightforward. One just need to take the DCS calculated with the highest amount of open channels in a given energy and compare this result to the experimental data. For

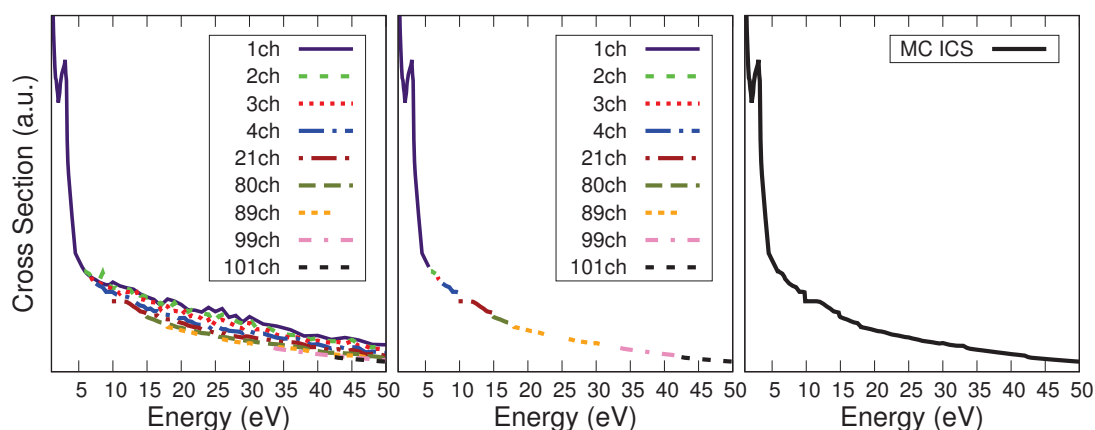


Figure 2.3 – Procedure to obtain the final MC cross sections for the fictitious molecule AB. Firstly, the ICSs are calculated with the different levels of multichannel coupling, as established in the strategy depicted in Fig. 2.2 (Left panel). Then, the ICS calculated with the highest amount of open channels is selected in each energy regime (Middle panel). Finally, the MC ICS is obtained concatenating the ICSs selected in the previous step (Right panel). A low-energy resonance and the multichannel coupling effect are also depicted in the figure.

instance, in the case of molecule AB, the 89ch DCS would be the best result at 20 eV, since all energetically accessible channels are treated as open in this level of calculation; and therefore this is the DCS that should be compared to the experimental data from the literature. Now, to obtain a final integral cross section (ICS) that includes the effects that arise from the electronic excitation of the molecule we use the ICSs calculated with the largest open-channel space in each energy regime. To obtain the ICS of the fictitious molecule AB (Fig. 2.2 (b)), the 1ch ICS would be used for impact energies below 5.80 eV, the 2ch ICS would be used for energies between 5.80 and 6.80 eV, the 3ch ICS would be used for energies between 6.80 eV and 7.50 eV, the 4ch ICS would be used for energies between 7.50 and 9.85 eV, the 21ch ICS would be used for energies between 9.85 and 14.87 eV, the 80ch ICS would be used for energies between 14.87 and 17.95 eV, the 89ch ICS would be used for energies between 17.95 and 33.54 eV, the 99ch ICS would be used for energies between 33.54 and 42.50 eV and the 101ch ICS would be used for energies above 42.50 eV. The ICS obtained through this process is said to be calculated at the multichannel coupling (MC) approximation. This procedure is depicted in Fig. 2.3. Note that in Fig. 2.3 a resonance and the multichannel coupling effect are also depicted. These phenomena are going to be discussed later in this chapter.

In summary, to perform scattering calculations in the multichannel coupling approximation with the SMCPP method, electronically excited states of the molecule must be included in the construction of the projector P given in equation (2.39). The MOB-SCI approach is used to obtain these electronically excited states, which involves

three steps: (i) generating a set of IVOs to represent the unoccupied molecular orbitals, (ii) performing a FSCI calculation, and (iii) select the relevant Slater determinants from the FSCI expansion of the wave function to perform the MOB-SCI calculation. Once the electronically excited states spectrum is obtained using the MOB-SCI method, a channel coupling strategy is created, and the scattering calculations are performed for different multichannel coupling schemes.

2.3 Binary-Encounter-Bethe model

In the Born-Oppenheimer approximation, the possible outcomes for an electron-molecule collision are the elastic scattering of the incident electron, the electronic excitation or the ionization of the molecular target. Thus, in order to perform a complete study on the electron scattering by molecules and obtain an estimation of the total cross section (disregarding vibration and rotational excitations) one must obtain the total ionization cross section (TICS) in addition to the elastic and electronic excitation cross sections. Although recently some effort has been made to include the ionization channel in the SMCPP method [97], it remains restricted to dealing only with the elastic and electronically inelastic channels. Thus, a different approach must be used to obtain the TICS.

The binary-encounter-Bethe (BEB) model [98] provides a simple and easy-to-use formula for the ionization cross sections. It emerges from the combination of two theories: the Mott theory for collision of two free electrons, which provides the description of the scattering of incident electrons with small impact parameter, and the Bethe theory, which accounts for the electrons that collide with large impact parameters.

The BEB model is free from arbitrary parameters or fitting constants. The cross section for the ionization of N_i electrons from an occupied orbital with binding energy B_i and average kinetic energy U_i by an incoming electron with energy E is

$$\sigma_i(t_i) = \frac{4\pi a_0^2 N_i (R/B_i)^2}{t_i + u_i + 1} \left[\frac{\ln(t_i)}{2} \left(1 - \frac{1}{t_i^2} \right) + 1 - \frac{1}{t_i} - \frac{\ln(t_i)}{t_i + 1} \right], \quad (2.70)$$

where a_0 is the Bohr radius, R is the Rydberg energy (13.6 eV), $t_i = E/B_i$, and $u_i = U_i/B_i$. The TICS is obtained as the sum of the ionization cross sections of each occupied molecular orbital, that is,

$$\sigma_{\text{TICS}} = \sum_{i=1}^{N_{occ}} \sigma_i(t_i) \quad (2.71)$$

where N_{occ} is the number of occupied molecular orbitals. All the necessary values to calculate the ionization cross sections through this method (U_i , B_i and N_i) are readily

obtained from an electronic structure calculation for the ground state of the molecular target.

It is important to emphasize that the calculations performed with the BEB model are independent from the calculations performed with the SMCPP method. This entails that the ionization channel does not compete for the flux that defines the elastic and electronically inelastic cross sections, nor these compete for the flux that defines the ionization cross sections.

Finally, by summing the total ionization cross section obtained through the BEB model, with the elastic and electronically inelastic cross sections calculated with the SMCPP method, we obtained the total cross section for the scattering of electrons by the molecules studied⁷.

2.4 Electron Scattering Phenomena

Now that we have established the methods used to obtain the cross sections, we shall explore some of the physical phenomena that emerge when electrons are scattered by molecules. To keep things concise, we will focus our discussion on the features that we observed in our results, namely shape resonances, the Ramsauer-Townsend minimum, and the multichannel coupling effect.

2.4.1 Resonances

As stated in the introduction of this work, the scattering process can produce a resonant state, which consists of the temporary capture of the incident electron by the molecular target. These resonances are ubiquitous in electron-induced chemistry, being responsible for the formation of charged radicals through molecular dissociation. Thus, identifying and characterizing these resonances is a common goal of electron scattering studies.

The capture mechanism of this complex phenomena can be understood in terms of a simplified picture, where the effective potential given by $V_{\text{eff}} = -V_0 + (\ell(\ell + 1))/r^2$ describes the scattering process. This potential is composed of an attractive well and an angular momentum barrier, as depicted in Fig. 2.4. An electron with energy E_1 will be simply scattered back into the continuum. On the other hand, an electron with incident energy E_2 may tunnel through the potential barrier and be captured by the effective well, forming a temporary bound state. In this case, a resonance is formed.

⁷ Once again, it is important to remember that we are working within the Born-Oppenheimer approximation. Thus, vibrational and rotational excitations are not considered.

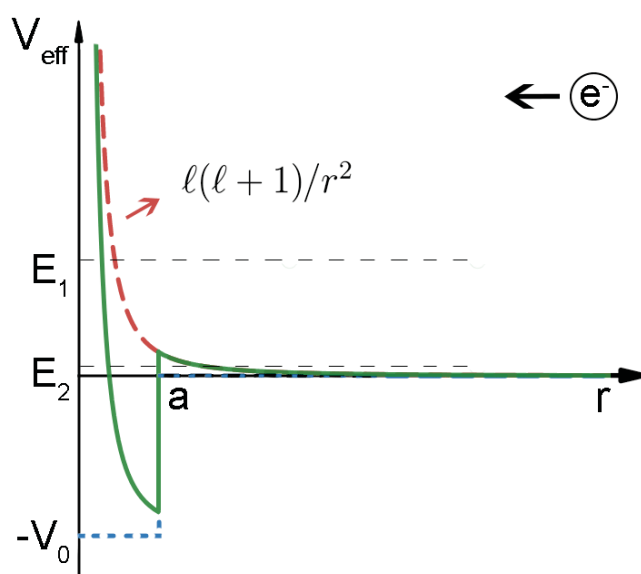


Figure 2.4 – Pictorial representation of the formation of a resonance. The effective potential felt by the incoming electron (from the right) is composed of an attractive square well and a angular momentum barrier. While an incident electron with energy E_1 is scattered back to the continuum, the effective well traps an electron with incident energy E_2 .

There are many signatures of resonances in the scattering calculations. Pronounced Lorentzian profiles in the cross sections indicates the presence of a resonant state. The central energy of these structures is the energy of the resonance, while the width of the Lorentzian peaks is associated with the lifetime of the resonant state. Through Heisenberg's uncertainty principle, a relationship between the resonance's lifetime and its width can be derived:

$$\Delta E \Delta t \approx \hbar, \quad (2.72)$$

where ΔE is the resonance's width, Δt is its lifetime and \hbar is Plank's constant over 2π . An example of how these profiles may appear in the cross sections is depicted in Fig. 2.3 for the fictitious molecule AB previously introduced. Below 5.0 eV a small structure is seen in the cross section, indicating the formation of a resonance.

Another possible way to identify and characterize resonances is through the diagonalization of the scattering Hamiltonian H_{N+1} in the CSFs space. This procedure yields a set of eigenvalues and eigenvectors. From this set, the eigenvectors whose eigenvalues are close to the resonant peaks in the cross sections may be analyzed. Since shape resonances leave the molecule in its electronic ground state, the eigenvectors of the scattering Hamiltonian linked with shape resonances are expected to be predominantly described by CSFs that are constructed with the ground state of the molecule. Thus, if the sum of the square of the coefficients associated with the static-exchange space of an eigenvector is large (close to one), this indicates that this eigenvector may be associated with a shape resonance. Note that the CSFs that com-

pose the static-exchange space are constructed with ground state Slater determinant of the molecule. Additionally, single-particle orbitals may be constructed from the possible resonant eigenstates of H_{N+1} . These orbitals are built as

$$|\phi_j\rangle = \sum_m^{n_{se}} |\varphi_m\rangle \langle \chi_m | \Psi_j^{N+1} \rangle \quad (2.73)$$

where the sum runs over all n_{se} CSFs that belong to the static-exchange space ($|\chi_m\rangle$, eq. 2.62), $|\varphi_m\rangle$ is the scattering orbital used in the construction of $|\chi_m\rangle$ and $|\Psi_j^{N+1}\rangle$ is the H_{N+1} eigenvector. These orbitals provide an accurate representation of the resonant states of the molecule and may be used to further identify and characterize shape resonances. Valence orbitals are responsible for the capture of the electron in shape resonances. Thus, if the single-particle orbital obtained with equation (2.73) has a valence-like character, it provides further evidence for the formation of a resonant state. Furthermore, the character of this orbital denotes the character of the shape resonance, being of σ^* or π^* character.

Other approaches may also be used to study resonant states. The eigenphase sum may be calculated, and a jump of π indicates the presence of a resonance [76], albeit in some cases this is obscured by the non-resonant (background) scattering. Another signature of resonances formation may be found in a time delay analysis [99], but this is not yet implemented in the SMCPP method.

As previously mentioned, resonances can be of shape, Feshbach or core-excited character. Shape resonances are formed by the capture of the incident electron into an unoccupied molecular orbital, while the molecule itself remains in the electronic ground state. With the various tools available, shape resonances can be relatively easy to identify and characterize. However, when considering resonances involving simultaneous electronic excitation of the molecule, such as Feshbach and core-excited resonances, the situation becomes more complex. The low-intensity of these resonances and the high sensitivity of the electronically inelastic cross sections to pseudoresonances and threshold effects makes the characterization of Feshbach and core-excited resonances very hard, if not impossible, for most molecules with the SMC method [19, 51, 95, 96]. Pseudoresonances are structures that have no physical meaning and appear in the cross sections due to energetically accessible channels that are treated as closed in a given level of calculation. Threshold effects are sudden increases and decreases in the cross sections associated with the opening of an inelastic channel that will be discussed in Sec. 2.4.3. Further theoretical work, that goes beyond the proposal of this dissertation, needs to be made in order to uniquely characterize these type of resonances.

2.4.2 Ramsauer-Townsend Minimum

One may write the cross section in a partial wave expansion as [76]

$$\sigma(k) = \sum_{\ell=0}^{\infty} \sigma_{\ell}(k) = \sum_{\ell=0}^{\infty} \frac{4\pi}{k^2} (2\ell + 1) \sin^2 \delta_{\ell}(k), \quad (2.74)$$

where k is the absolute value of the incident particle's wave vector, and δ_{ℓ} is the phase-shift (eigenphase) associated with the partial wave with angular quantum number ℓ .

In the low-impact energy regime the cross section is dominated by the s -wave ($\ell = 0$) scattering. In this case, equation (2.74) reduces to

$$\sigma(k) = \sigma_0(k) = \frac{4\pi}{k^2} \sin^2 \delta_0(k). \quad (2.75)$$

Thus, the cross section goes to zero when $\sin^2 \delta_0 = 0$, which occurs when the eigenphase associated with the s -wave becomes zero or goes through π . Especially, when the potential felt by the incoming electron changes from attractive to repulsive the s -wave eigenphase is equal to zero [62]. For apolar molecules, the potential that describes the electron molecule interaction can be written as

$$V = V_{static} + V_{exchange} + V_{pol}. \quad (2.76)$$

In the expression above, V_{static} is the static Coulomb potential (attractive), $V_{exchange}$ is a potential associated with the antisymmetrization of the wave function (repulsive)⁸, and V_{pol} is a potential associated with the polarization of the molecular target (attractive).

At specific impact energies, the net potential can change its sign, resulting in a global minimum of the cross section. This phenomenon is known as Ramsauer-Townsend (RT) minimum. Since the cross section represents a relative probability of interaction, the RT minimum corresponds to an incident energy such that the molecule becomes virtually transparent to the incident electron. It is important to note that this effect only occurs when considering polarization effects. In the absence of polarization, the attractive portion of the potential is not sufficiently strong, leading to a purely repulsive potential in the low-impact energy regime.

2.4.3 Multichannel Coupling Effect

Polarization effects play a crucial role in the low-impact energy regime. These effects are vital to accurately describe phenomena like shape resonances and the RT minimum. As we move towards higher impact energies, where inelastic channels

⁸ In the sense of Pauli's exclusion principle the incoming electrons cannot occupy a doubly occupied spin-orbital, generating a "repulsive potential".

become energetically accessible, the scattering behaviour is primarily governed by the multichannel coupling effect [100].

To understand the multichannel coupling effect lets recall equation (2.2). The differential cross section (DCS) for a given channel is defined as the ratio of the number of scattered particles per unit time associated with that channel (dn_f) within a solid angle ($d\Omega$), to the incident flux of particles (F_i):

$$\frac{d\sigma_f}{d\Omega}(k; \theta, \phi) = \frac{dn_f}{F_i d\Omega}. \quad (2.77)$$

Writing dn_f as

$$dn_f = \frac{J_f r^2 d\Omega}{t}, \quad (2.78)$$

where J_f is the probability current associated with the scattered particles, $r^2 d\Omega$ is the infinitesimal area into which particles are scattered and t is unit time. Now, since

$$F_i t = J_i, \quad (2.79)$$

where J_i is the probability current associated with the incoming wave function, we obtain

$$\frac{d\sigma_f}{d\Omega}(k; \theta, \phi) = \frac{J_f r^2}{J_i}. \quad (2.80)$$

Therefore, the DCS for each final channel is associated with the probability current of that individual channel. As a consequence, if the probability current decreases, the corresponding DCS also decreases.

The probability flux is defined as

$$\vec{J} = \frac{\hbar}{m} \Im(\Psi^* \vec{\nabla} \Psi), \quad (2.81)$$

where Ψ is the scattering wave function. Note that for real potentials, which is the case here, \vec{J} respects the continuity equation

$$\frac{\partial \rho}{\partial t} + \vec{\nabla} \cdot \vec{J} = 0, \quad (2.82)$$

where $\rho = |\Psi|^2$. This entails that the total probability current is conserved throughout the scattering process among all open channels, that is, total incoming and outgoing fluxes must be equal.

The multichannel coupling effect is introduced in the scattering calculation when inelastic channels are treated as open. This effect results in a decrease in the magnitude of the cross sections. With the two concepts mentioned above, we are able to understand that this effect arises from the competition for the probability flux between the accessible channels. As more channels are treated as open, the competition for the probability flux increases, decreasing the flux that defines each individual cross

section, lowering its magnitude. To illustrate this, let's consider a scenario in which a 1ch calculation is performed, with only one channel treated as open. In this case, all probability flux will define only the cross section associated with this channel. However, if a second calculation is subsequently performed, where two channels are treated as open (2ch calculation), the second channel will compete for the flux that was previously solely defining the cross section of the first channel. Consequently, the magnitude of the first channel's cross section decreases. Therefore, as the number of open channels increases in scattering calculations, the magnitude of the cross sections decreases. It's important to note that as the incident electron energy increases, more channels become energetically accessible. Hence, this effect becomes more significant at higher-impact energies.

An useful classical analogy to gain some physical intuition about this effect is that of water flowing through a pipe system [101], as depicted in Fig. 2.5. Initially, when only one pipe is open (Fig. 2.5 (a)), all the water flows exclusively through that particular pipe. Then, as more pipes are subsequently opened, the flow of water gets distributed among the additional pipes, resulting in a reduction of the flux passing through the initial pipe (Fig. 2.5 (b)).

Equipped with the concepts behind the multichannel coupling effect we may now understand the origin of the threshold effects in the cross sections. Near the excitation threshold the cross section associated with that channel increases rapidly with energy. This generates an abrupt competition for the flux that defines each cross section in the vicinity of the threshold, which causes the cross sections of the previously open channels to rapidly increase or decrease, generating "jumps" in the cross sections, known as Wigner cusps [102, 103]. This effect was observed experimentally for the vibrational excitations channels of hydrogen halides [104] and appear in our cross sections when electronically inelastic channels are taken in consideration in our calculation.

An example of how the multichannel coupling effect appears in our results

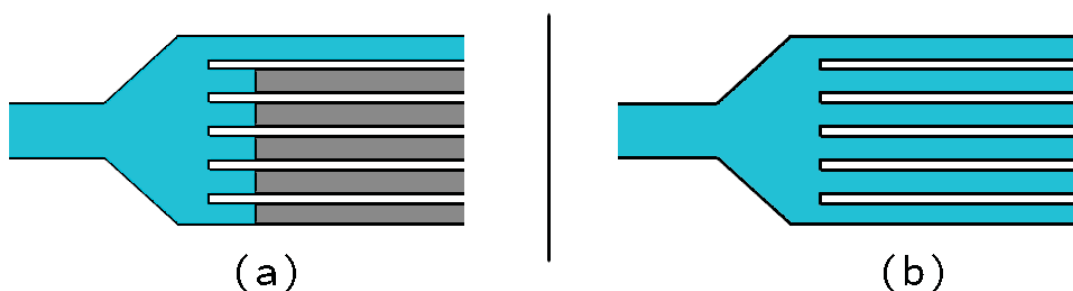


Figure 2.5 – Pictorial representation of the multichannel coupling effect in the flow of water in a pipe system. Firstly, only one pipe is open, thus all the water flows only through this accessible channel (a). Then, more pipes are opened, allowing the water to flow through them, which reduces the flux that flows through the original channel (b).

can be seen in Fig. 2.3 for the previously introduced fictitious molecule AB. The left panel showcases ICSs calculated using various multichannel coupling schemes. As the number of open channels increases in the calculation, the magnitude of the cross section decreases. Some small threshold effects may also be observed.

CHAPTER 3

Formamide

In this chapter the cross sections for the elastic and electronically inelastic scattering of electrons by formamide (Figure 3.1) are presented and discussed. This work was done in collaboration with professor Giseli Maria Moreira and has been published in the *Physical Review A* journal early 2023 [51].

Formamide is the simplest molecule containing a peptide bond, a fundamental linkage between amino acids that constitutes the building blocks of proteins. As a consequence, formamide is an important toy-model to investigate the interactions between low-energy electrons and the peptide backbone of proteins [36]. Furthermore,

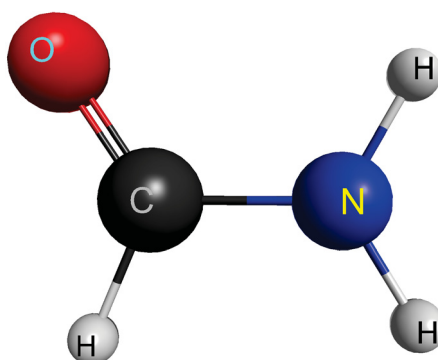


Figure 3.1 – Schematic representation of formamide's chemical structure (generated with MacMolPlt [35]).

since formamide has been observed in the interstellar medium [37, 38] and can be used as a starting point to synthesize DNA nucleobases [11], it is also considered an important prebiotic molecule. Thus, the interactions between electrons and formamide are relevant from both the biological and astrophysical perspectives.

Although measured cross sections were not published in the literature, the electron-formamide interactions have been studied experimentally. Seydou *et al.* [39] reported the formation of a π^* shape resonance at 2.05 eV through an electron transmission spectroscopy (ETS) experiment. Hamann *et al.* [40] studied the DEA of formamide up to 18 eV using a crossed electron/molecule beam technique and reported four resonant dissociation channels. Li *et al.* [41], with a combined experimental and computational effort, investigated in more detail the DEA mechanisms of formamide.

Conversely, an abundance of theoretical cross sections for the scattering of electrons by formamide have been reported in the literature. Bettenga [42] calculated the elastic integral (ICSs) and momentum transfer cross sections (MTCSs) for the electron scattering by formamide through the SMCPP method in the SE and SEP approximations. A π^* shape resonance located in the C=O bond was found centered around 4.5 eV in the SE approximation and around 2.5 eV in the SEP approximation. Wang and Tian [43] investigated the elastic and electronically inelastic scattering of electrons by formamide using the R-matrix method in the SE, SEP and close-coupling (CC) approximations. These authors reported differential cross sections (DCSs), ICS and MTCS for the elastic channel, while 4 integral electronically inelastic cross sections were reported for the excitation of formamide from the ground state to its 4 low-lying electronically excited states. The electron induced ionization of formamide was studied by Gupta *et al.* [44], using the spherical complex optical potential formalism (SCOP) and complex scattering potential ionisation contribution method and the Binary-encounter-Bethe (BEB) model calculated the total ionization cross section (TICS) for formamide. Homem *et al.* [45] reported a comprehensive set of cross sections composed of the elastic ICS, DCSs, MTCS, total absorption cross section (TACS) and total cross section (TCS) for the scattering of electron by formamide. In their work, the cross sections were obtained with a single-center-expansion technique combined with the method of Padé (SCE+Padé). Vinodkumar *et al.* [46] reported elastic DCSs, MTCS, excitation ICSs for 8 electronically excited states of formamide and the TCS using a combination of the R-matrix method for impact energies below 20 eV and the SCOP formalism for higher impact energies. Silva *et al.* [47] studied the electron and positron interactions with formamide, reporting the elastic ICS, MTCS and DCSs obtained through the SMCPP method for energies below 10 eV. Later, the same authors investigated the behaviour of the π^* shape resonance upon single and double methylation of formamide [48].

Additional theoretical studies have been done on the electron-formamide inter-

actions that did not report cross sections. Goumans *et al.* [49] investigated the possible dissociation pathways of formamide mediated by DEA. These authors reported a π^* shape resonance around 3.77 eV and a σ^* resonance around 14.9 eV in the ground state equilibrium geometry and studied their behaviour as the C-H and C-N bonds were stretched. Gallup [50] studied the shape resonances of selected organic molecules using the finite element discrete model method, finding at 2.1226 eV a ${}^2A''$ resonance for formamide.

Here, we extend the previous results obtained with the SMCPP method [42, 47, 48] by increasing the impact energies up to 50 eV, including multichannel coupling effects in the scattering calculations and investigating electronically inelastic channels. As discussed in chapter 2, the minimal orbital basis for a single configuration interaction (MOB-SCI) strategy [93] was used to describe the electronically excited states of the molecule. In the calculations presented in this chapter, 89 hole-particle pairs (Slater determinants) were used in the MOB-SCI expansion of the molecular wave function, resulting in a scattering calculation with up to 179 open channels (89 singlets + 89 triplets + elastic channel). To complement these results and estimate a TCS¹, the total ionization cross sections (TICS) was obtained with the BEB model [98].

3.1 Computational Details

The geometry of the ground state of formamide was optimized through a MP2/aug-cc-pVDZ calculation with the computational package GAMESS [105] in the C_s point group. All the following calculations were performed at this geometry. The basis set used in the MOB-SCI and scattering calculations contains $6s5p3d$ CG functions for the heavy atoms of formamide (C, O and N) with exponents shown in Tab. 3.1, while the $4s/3s$ basis set of Dunning [106] increased with one additional p -type function with exponent 0.75 was used for the hydrogen atoms². The improved virtual orbitals (IVOs) [94] used as unoccupied molecular orbitals were generated with triplet coupling using the highest occupied orbital of a' symmetry as hole orbital.

Within the chosen basis set, the expansion of the FSCI wave function contains 1134 hole-particle pairs, which arise due to single excitations from 9 hole orbitals to 126 particle orbitals. From these, 89 hole-particle pairs were selected for the MOB-SCI calculation. This reduction in the number of hole-particles pairs makes the scattering calculations with the inclusion of the multichannel coupling computationally feasible while still keeping an appropriate level of accuracy in the description of the lowest 20

¹ This cross section was estimated within the Born-Oppenheimer approximation in the sense that vibrational and rotational excitations of the molecule were not considered.

² These are s , p and d functions in the sense of equation (2.61), which are used to expand the atomic orbitals ζ_μ used in equation (2.60).

Table 3.1 – Exponents of the uncontracted basis functions for the C, N and O atoms.

Type	C	N	O
<i>s</i>	12.49628	17.56734	16.05878
<i>s</i>	2.470286	3.423615	5.920242
<i>s</i>	0.614028	0.884301	1.034907
<i>s</i>	0.184028	0.259045	0.316843
<i>s</i>	0.039982	0.055708	0.065203
<i>s</i>	0.009996	0.013927	0.016301
<i>p</i>	5.228869	7.050692	10.14127
<i>p</i>	1.592058	1.910543	2.783023
<i>p</i>	0.568612	0.579261	0.841010
<i>p</i>	0.210326	0.165395	0.232940
<i>p</i>	0.072250	0.037192	0.052211
<i>d</i>	1.794795	0.975569	1.698024
<i>d</i>	0.420257	0.253058	0.455259
<i>d</i>	0.101114	0.078904	0.146894

electronically excited states of the molecular target. An additional calculation with the equation-of-motion coupled-cluster with singles and doubles (EOM-CCSD) [107–110] method and the aug-cc-pVDZ basis set was performed to evaluate the quality of the electronically excited states obtained in the FSCI and MOB-SCI approximations. This robust EOM-CCSD/aug-cc-pVDZ calculation was done using the computational package Psi4 [111]. In Table 3.2 the vertical excitation energies obtained with these calculations are presented alongside theoretical [43, 46, 112, 113] and experimental [114–116] results found in the literature. Firstly, it is important to highlight that the MOB-SCI results reproduce well the FSCI spectrum, which indicates that the 89 hole-particle pairs selected for the MOB-SCI expansion of the molecular wave function are well suited to describe the low-lying excited states of the molecule within the single-configuration interaction (SCI) approach. When comparing these SCI results to the more robust EOM-CCSD/aug-cc-pVDZ calculation and with the results from the literature [43, 46, 112–116] an overall satisfactory agreement is found. The limitations of the SCI approximation are reflected in two aspects: the first one is that the order of some electronically excited states is inverted in relation to more robust electronic structures calculations. For instance, the order of the two lowest electronically excited states ($1^3A'$ and $1^3A''$) is inverted in the FSCI and MOB-SCI spectrum if compared to the EOM-CCSD calculation. The second one is that the electronically excited states of A' symmetry are not well described. An additional FSCI calculation (not shown here) with a larger basis set containing $7s7p3d$ CG functions showed no improvement on the two shortcomings mentioned. Thus, they seem to be related to the limitation of using only single excitations in the molecular wave function expansion. To rectify that, a more robust electronic structure method would need to be used to describe the electronically excited states in

Table 3.2 – Vertical excitation energies (in eV) for the first 10 excited electronic states obtained from a full single configuration interaction (FSCI), minimal orbital basis for single configuration interaction (MOB-SCI) and EOM-CCSD/aug-cc-pVDZ calculations. We compared our results with the theoretical results of Wang and Tian (CAS-Cl/cc-pVTZ) [43], Vinodkumar *et al.* (CI/6-311G) [46], Chong (TDDFT/(SAOP)/et-pVQZ) [112] and Hirst *et al.* (MRCI/6-31+g**) [113] and also with the experimental results of ^αGingell *et al.* (VUV and EELS) [114], ^βStaley *et al.* (ion cyclotron resonance detection) [115], and ^γBasch *et al.* (VUV) [116].

State	FSCI	MOB-SCI	EOM-CCSD	Ref. [43]	Ref. [46]	Ref. [112]	Ref. [113]	Expt.
1 ³ A'	5.368	5.572	5.605	5.24	-	5.64	-	6.0 ^α
1 ³ A''	5.675	5.841	5.238	5.71	6.07	5.23	-	5.2 ^α ,5.30 ^β
1 ¹ A''	6.331	6.416	5.572	5.49	-	5.71	5.86	5.82 ^α ,5.65 ^γ
2 ³ A''	7.259	7.450	6.481	6.30	-	-	-	
2 ¹ A''	7.646	7.745	6.694	6.72	6.47	7.32	6.14	
1 ¹ A'	8.378	8.644	6.795	6.95	-	6.64	6.49	6.35 ^α ,6.80 ^γ
3 ³ A''	8.440	8.546	7.482	7.62	-	-	7.01	
2 ³ A'	8.510	8.609	6.731	6.98	6.63	6.48	-	6.4 ^α
3 ¹ A''	8.593	8.651	7.546	7.77	-	8.07	-	
3 ³ A'	8.624	8.930	7.306	7.63	8.91	-	-	

the scattering calculation, which is beyond the scope of the present dissertation.

A schematic representation of the MOB-SCI spectrum is presented in Figure 3.2, along the different levels of multichannel coupling selected to perform the scattering calculations. As mentioned in chapter 2, the distinct levels of multichannel coupling are denoted by $N_{open}ch$, where N_{open} is the number of channels treated as open in that level of approximation. The coupling levels used in the scattering calculations were performed following the strategy: 3ch, 4ch, 6ch, 22ch, 57ch, 103ch, 135ch, 154ch, 167ch, 177ch, and 179ch, where the thresholds of each level of calculation are presented in Figure 3.2. The 3ch, 4ch and 6ch calculations were performed to analyse how the low-lying electronically excited states compete for the flux that defines the cross sections. The 22ch, 57ch, 103ch, 135ch, 154ch consider the best possible multichannel coupling for impact energies of 10.0, 12.5, 15.0, 17.5 and 20.0 eV, respectively. The 167ch and 177ch calculations were performed to treat a group of closely lying states as open channels simultaneously, and the 179ch calculation considers all electronically inelastic channels as open in the scattering calculations.

It is important to note that even if a specific channel is not treated as open in a particular level of calculation, it is still included in the configurational space as a closed channel, that is, the same CSF space is used in all levels of calculation. This guarantees that the effects seen when comparing different levels of calculation arises solely from the different multichannel coupling schemes used for each calculation. Additionally, these closed channels contribute to the description of the polarization effects of the molecular target. On the other hand, the ICS calculated with fewer open channels present pseudoresonances in the high energy regime (as will be shown in the next

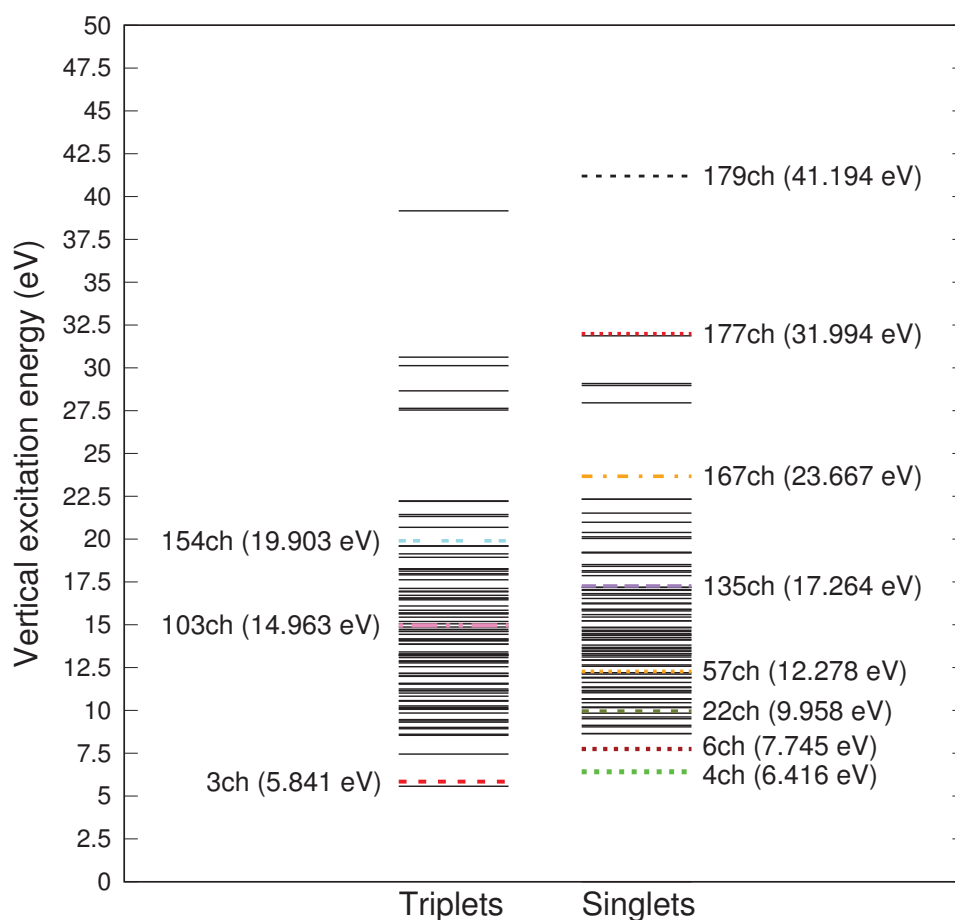


Figure 3.2 – Schematic representation of the vertical excitation energies (in eV) of the 178 electronically excited states of formamide obtained with the MOB-SCI calculation and the different multichannel coupling strategies employed in the scattering calculations. The dashed red line corresponds to the threshold of the 3ch scattering calculation; dashed green line, 4ch; dashed brown line, 6ch; dashed olive line, 22ch; dotted orange line, 57ch; dash-dot-dot pink line, 103ch; long-dashed purple line, 135ch; double-dotted cyan line, 154ch; dash-dot orange line, 167ch; dotted red line, 177ch. The 179ch threshold is also indicated.

section). These structures have no physical meaning and are a result of channels that are energetically accessible but treated as closed in these levels of calculation.

As mentioned in chapter 2, in this dissertation the scattering calculations that include multichannel coupling used the same hole-particle pairs of the MOB-SCI expansion to construct the singly-excited Slater determinants of the CSFs (see eq. (2.69)). All unoccupied IVOs were used as scattering orbitals. With this procedure, we obtained 5554 CSFs of A' and 5786 of A'' symmetry. Note that the size of the CSF space of A'' symmetry is comparable to the ones used in previous results obtained with the SMCPP method aimed to describe the low-energy electron-formamide scattering [42, 47]. Therefore, we expect that the polarization effects of the target due to the incident

Table 3.3 – Chosen values for l_{SMC} for the Born-Closure procedure performed in the calculations of the elastic cross sections. Energy ranges are presented in eV.

l_{SMC}	Energies	l_{SMC}	Energies
1	1.0 to 1.9	6	25.0 to 30.0
2	2.0 to 3.5	7	31.0 to 44.0
3	4.0 to 6.5	8	45.0
4	6.6 to 12.0	9	46.0 to 50.0
5	12.5 to 24.0		

electron are well described by this configuration space. This expectation is indeed correct since the position of the π^* shape resonance agrees well with the data presented in the literature, as will be discussed latter.

Formamide is a polar molecule, thus the Born-Closure procedure was performed in order to improve the description of long-ranged interactions in the scattering calculations. According to our calculations, formamide has a permanent dipole moment of 4.35 D. This result overestimates the experimental value of 3.73 D [117]. To perform the Born-Closure procedure one needs to choose in equation (C.2) a l_{SMC} value for each impact energy. These were chosen in order to obtain a good agreement between the DCSs at high scattering angles calculated utilizing the Born closure and solely through the SMC method. The l_{SMC} used in each energy regime are listed in Tab. 3.3.

The necessary parameters for the BEB calculation were obtained at the equilibrium ground state geometry at the HF/aug-cc-pVDZ level of calculation as implemented in the GAMESS computational package [105]. These parameters are presented in appendix D.

3.2 Elastic channel

The elastic DCSs for selected impact energies are depicted in Fig. 3.3. These cross sections were obtained with the SMCPP method and the Born-closure procedure for the different levels of multichannel coupling presented in Fig. 3.2. As expected, the multichannel coupling effect can be seen in the results shown in Fig. 3.3, where the magnitude of the elastic DCSs decreases as the number of open channels increases in the scattering calculations. As explained in chapter 2, this effect is a consequence of the competition between the elastic and electronically inelastic channels for the flux that defines the cross sections. Interestingly, the low-lying channels appear to compete more actively for the flux that defines the elastic cross section than the higher-lying channels. This is reflected in our results when one compares the DCSs calculated with up to 103 open channel, where the difference in magnitude is noticeable, meanwhile the magnitude of the DCSs calculated with higher channel coupling schemes ($N_{open} > 103$)

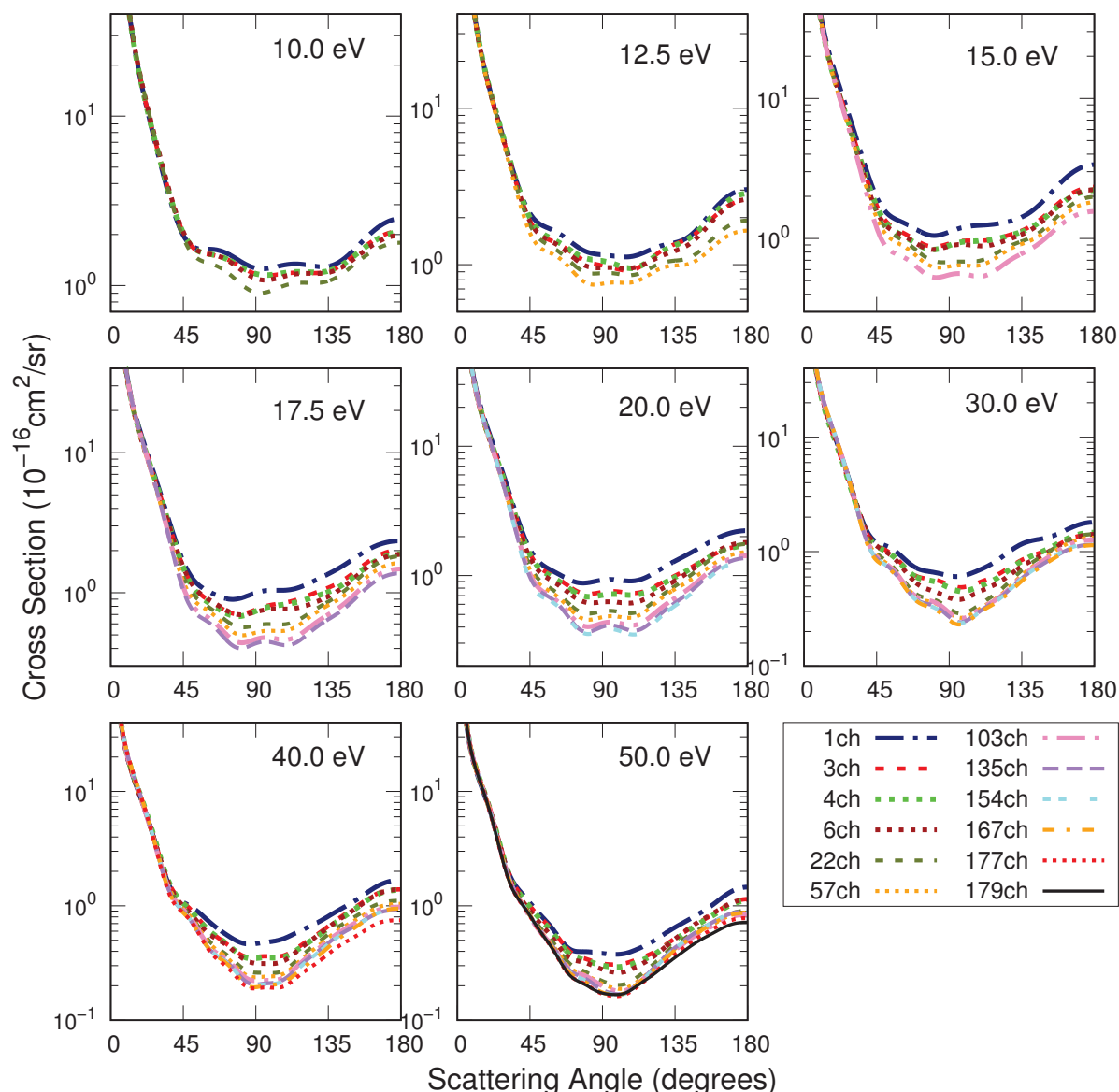


Figure 3.3 – Elastic DCSs for the scattering of electrons by formamide calculated with different multichannel coupling schemes. Dash-dotted blue line, 1ch; dashed red line, 3ch; dashed green line, 4ch; dashed brown line, 6ch; dashed olive line, 22ch; dotted orange line, 57ch; dash-dot-dot pink line, 103ch; long-dashed purple line, 135ch; double-dotted cyan line, 154ch; dashed orange line, 167ch; dotted red line, 177ch and full black line, 179ch.

are similar. Apart from that, due to the long-ranged dipole interactions between the electron and the molecular target, a high forward scattering is observed in all cross sections presented in Fig. 3.3.

Although experimental DCSs were not found in the literature, there are theoretical results for impact energies below 14 eV [43, 45–47]. In Figs. 3.4 and 3.5, these results are compared to the present elastic DCSs calculated with only the elastic channel open (1ch) and with the results obtained with the highest multichannel coupling (MC) scheme in each impact energy (3ch at 6 eV, 6ch at 8 eV, 22ch at 10 and 12 eV and

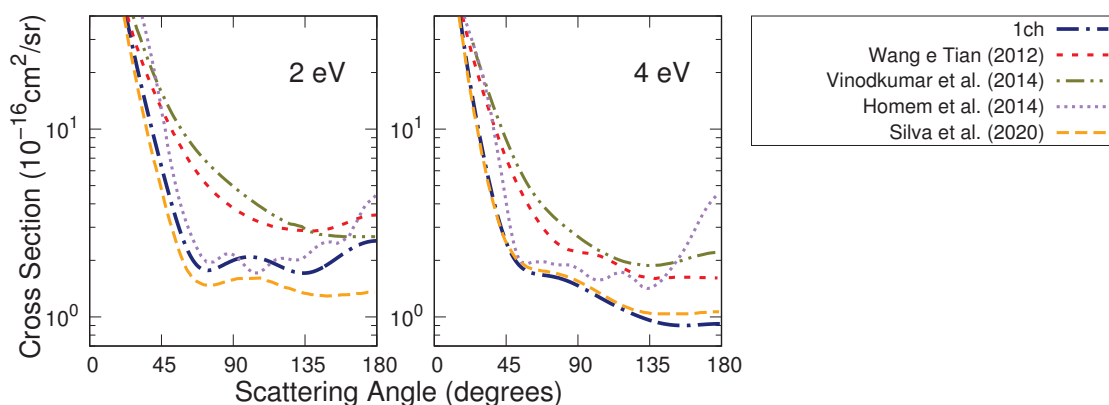


Figure 3.4 – Elastic DCSs for the impact energies of 2 and 4 eV. Dash-dot blue line, present 1ch; short-dashed red line, results from Wang and Tian (R-Matrix) [43]; dash-double-dotted olive line, results from Vinodkumar *et al.* (R-Matrix) [46]; dotted purple line, results from Homem *et al.* (SCE+Padé) [45]; dashed orange line, results from Silva *et al.* (SMCPP) [47].

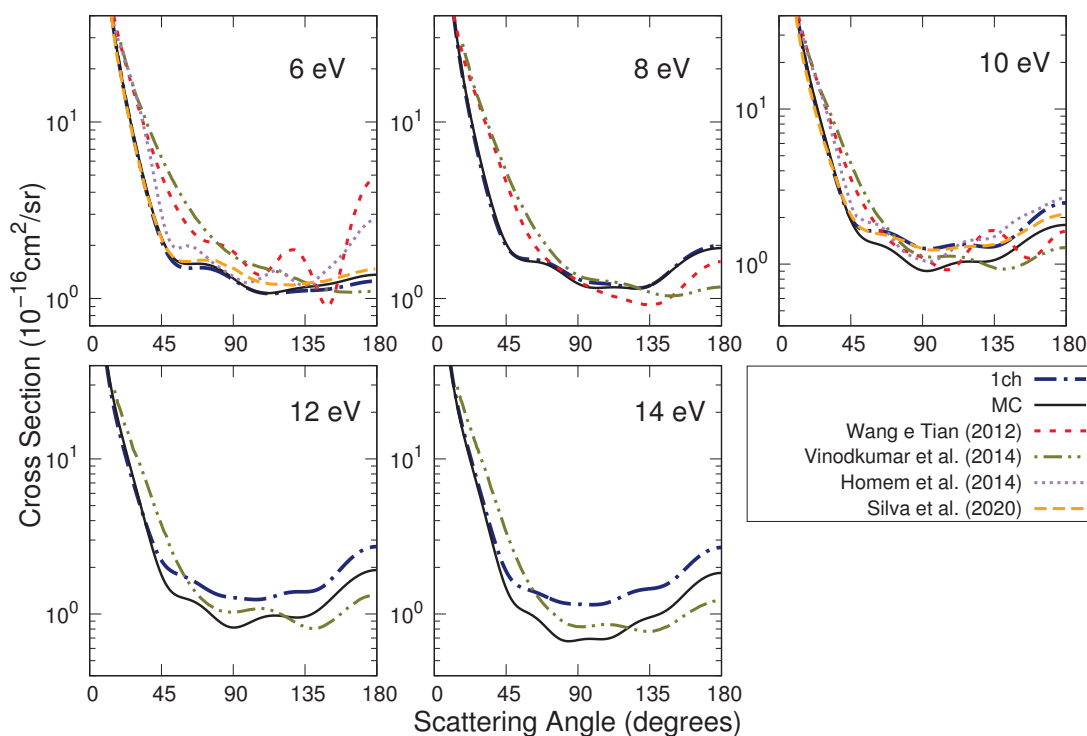


Figure 3.5 – Elastic DCSs for the impact energies of 6, 8, 10, 12 and 14 eV. Dash-dot blue line, present 1ch; full black line, present results obtained with the highest multichannel coupling (MC) scheme in each impact energy (3ch at 6 eV, 6ch at 8 eV, 22ch at 10 eV and 12 eV and 57ch at 14 eV); short-dashed red line, results from Wang and Tian (R-Matrix) [43]; dotted purple line, results from Homem *et al.* (SCE+Padé) [45]; dash-double-dotted olive line, results from Vinodkumar *et al.* (R-Matrix) [46]; dashed orange line, results from Silva *et al.* (SMCPP) [47].

57ch at 14 eV). Besides from the DCS at 2 eV, the 1ch calculation agrees well with the previous results from Silva *et al.* [47]. This was expected since these authors also used the SMCPP method with a similar CSF space. The discrepancy at 2 eV arises from the

position of the shape resonance in the ICSs (that will be shown latter in this section), which is slightly different between the present calculation and the one performed by Silva *et al.* [47]. Unfortunately, the comparison between the present results and the data from the literature obtained with other theoretical methods [43, 45, 46] is far from satisfactory. The differences at 2 and 4 eV may be related once again to the position of the shape resonance in the ICSs due to different polarization schemes used in each calculation, which affect the magnitude and oscillatory behaviour of the DCSs around these energies. At 6, 8, 10, 12 and 14 eV the overall magnitude of all the calculated DCSs are similar, but the oscillatory behaviour differs. The lack of experimental data makes it impossible to further scrutinize these differences beyond conjectures.

The elastic ICSs calculated without the born-closure procedure with different multichannel coupling schemes are presented in Fig. 3.6. The well-known shape resonance of formamide is centered at 2.18 eV according to our 1ch calculation. Once again, the multichannel coupling effect can be observed in the ICSs shown in Fig. 3.6, where the magnitude of the ICS decreases as the open-channel space increases in the scattering calculations. Additionally, the pseudoresonances observed above the first excitation threshold (5.572 eV) in the 1ch calculation tend to vanish from the cross sections as more channels are treated as open, up to a point where the cross section is structureless when all electronically inelastic channels are treated as open (179ch).

To obtain an elastic ICS that includes both the polarization and multichannel

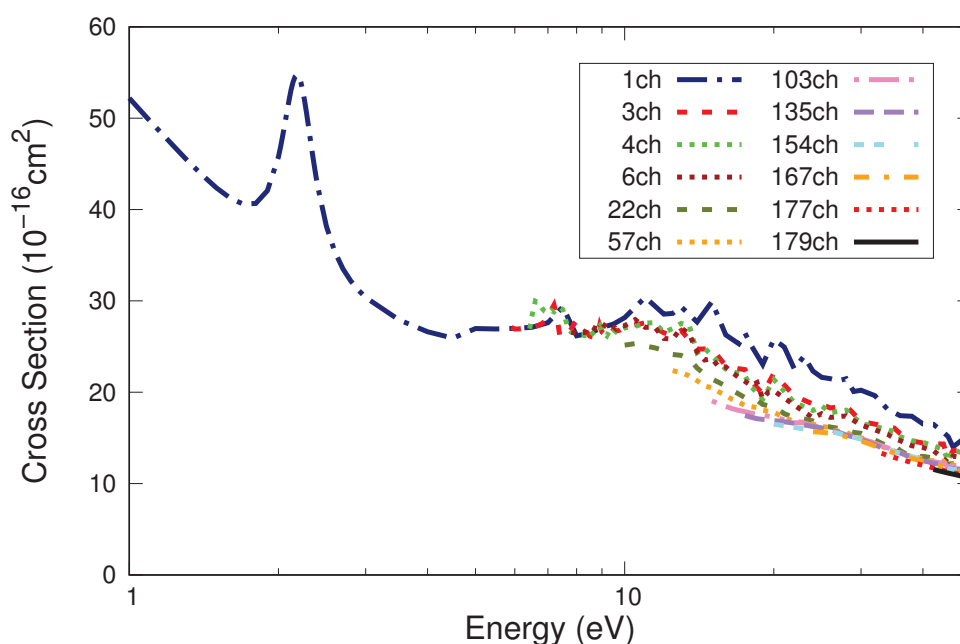


Figure 3.6 – Elastic ICS calculated using different multichannel coupling schemes. The lines in color follow the caption of Fig. 3.3.

Table 3.4 – Channel coupling strategies used for each electron impact energy (in eV) interval to compute the final cross sections obtained in the multichannel coupling (MC) approximation.

Electron impact energy	MC level	Electron impact energy	MC level
0.1 to 5.841	1ch	14.963 to 17.264	103ch
5.841 to 6.416	3ch	17.264 to 19.903	135ch
6.416 to 7.745	4ch	19.903 to 23.667	154ch
7.745 to 9.958	6ch	23.667 to 31.994	167ch
9.958 to 12.278	22ch	31.994 to 41.194	177ch
12.278 to 14.963	57ch	41.194 to 50.000	179ch

coupling effects, we used the ICSs obtained with the best possible multichannel coupling level in each energy regime, following the multichannel coupling strategy depicted in Fig. 3.2. We refer to this approximation as the multichannel coupling (MC) level. For this approximation, the multichannel coupling scheme considered for a given incident energy interval can be found in Tab. 3.4 and is indicated by a line in color in Fig. 3.2. That is, for energies up to 5.841 eV the 1ch ICS was used to obtain the ICS at the MC level, for energies between 5.841 and 6.416 eV the 3ch ICS was used, and so on.

In Fig. 3.7 the elastic MC ICSs calculated with and without Born-closure procedure are presented alongside results from the literature [39, 42, 43, 45, 47, 49]. As opposed to the elastic DCSs which give a more detailed description of the scattering process, the differences between the calculations performed here and in previous works are averaged out in the ICS and an overall good agreement is found (note the log scale in the x axis). The main discrepancies arise from the position of the shape resonance in the ICSs, related to the distinct treatments of the polarization effects in each calculation. Furthermore, the high magnitude of the permanent dipole moment of formamide leads to a large cross section when the Born-closure procedure is performed, resulting in a good agreement with previous results from the literature [45, 47]. In the present calculation the well-known π^* shape resonance is centered at 2.18 eV, which is in good agreement with some results from the literature [39, 40, 42, 43, 47, 48, 50], while underestimates others [43, 45, 46, 49]. A comparison between the position of this shape resonance found by us in the present calculation and the ones mentioned from the literature can be found in Tab. 3.5. It is also important to highlight that in the present calculation there is a tail of the π^* shape resonance at 2 eV, while in the ICS from Silva *et al.* [47] the resonance is centered at slightly higher energy, which explains the differences found in the elastic DCS at 2 eV (Fig. 3.4). Beyond that, the spectrum of electronically excited states of formamide is the densest between 6 and 20 eV (Fig. 3.2). As a consequence, many channels that are energetically accessible are treated as closed in this energy regime even at the MC level of calculation. Thus, pseudoresonances and threshold effects appear in the cross section below 20 eV. Finally, in contrast to the previous studies

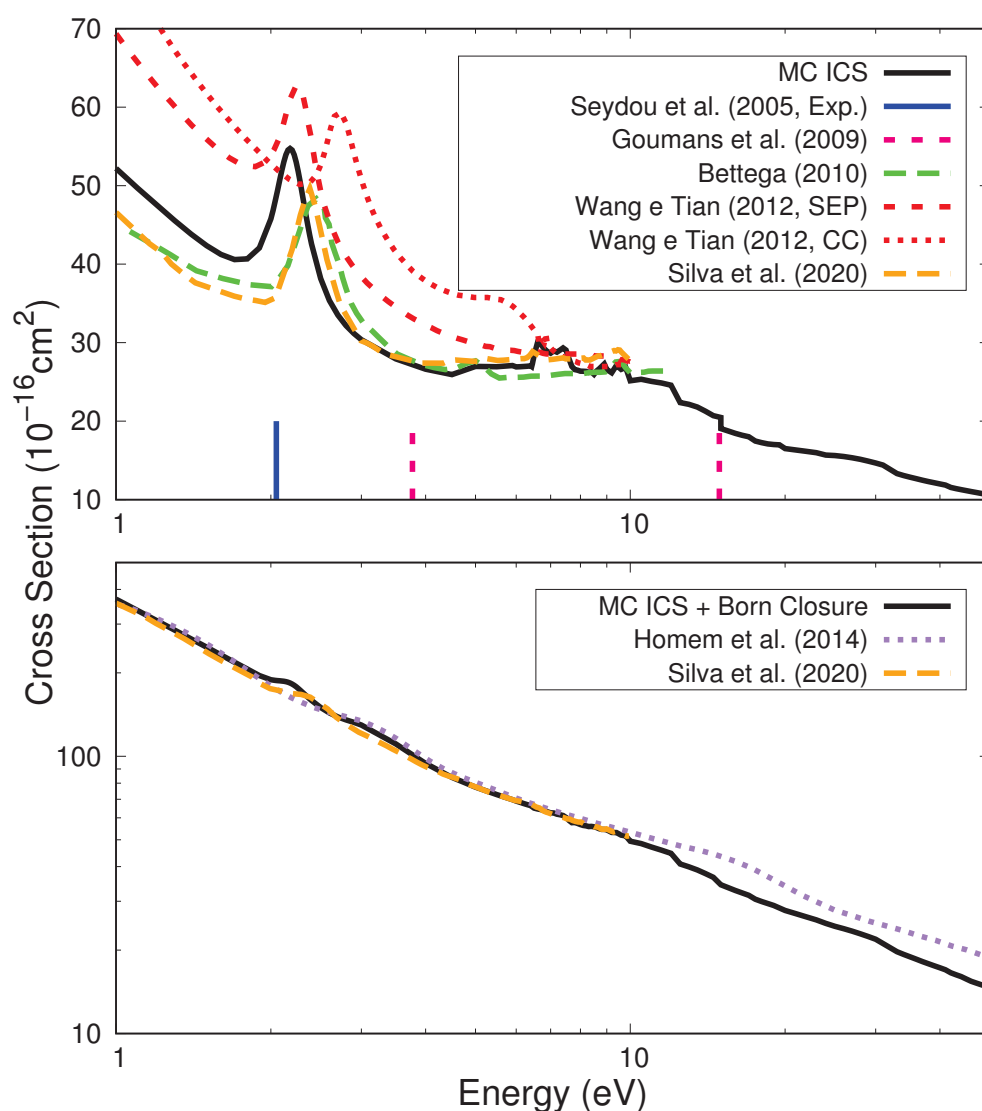


Figure 3.7 – Upper panel: Elastic ICS without the Born-closure procedure for the scattering of electrons by formamide. Lower panel: Elastic ICS with the Born-closure procedure. Full black line, present MC results; dashed green line, results from Bettega (SMCPP) [42]; dashed red line, SEP results from Wang and Tian (R-Matrix) [43]; dotted red line, CC results from Wang and Tian (R-Matrix) [43]; dashed orange line, results from Silva *et al.* (SMCPP) [47]; and dotted purple line, results from Homem *et al.* (SCE+Padé) [45]. The position of the resonances from Seydou *et al.* (Experimental) [39] and Goumans *et al.* (Theory) [49] are also presented as a vertical blue line and vertical dashed pink lines; respectively.

performed by Goumans *et al.* [49], Homem *et al.* [45] and Vinodkumar *et al.* [46] a broad shape resonance around 15 eV was not observed in our results. This resonance may be hidden by the pseudoresonances present in the MC ICS at intermediate energies.

Table 3.5 – Position of the shape resonance found by the present calculation and from the literature (in eV).

Reference	Energy
Present	2.18
Seydou <i>et al.</i> [39]	2.05
Hamann <i>et al.</i> [40]	2.0 - 2.7
Bettega [42]	2.5
Wang and Tian [43]	2.25 (SEP), 2.67 (CC)
Homem <i>et al.</i> [45]	3.5
Vinodkumar <i>et al.</i> [46]	3.41
Silva <i>et al.</i> [47]	2.38
Silva <i>et al.</i> [48]	2.32 (SEP1), 2.46 (SEP3)
Goumans <i>et al.</i> [49]	3.77
Gallup [50]	2.1226

3.3 Electronically inelastic channels

The DCSs for the electronic excitation from the ground state to the $1^3A'$ (5.572 eV), $1^3A''$ (5.841 eV), $1^1A''$ (6.416 eV) and $2^3A''$ (7.450 eV) states of formamide are presented in Figs. 3.8, 3.9, 3.10 and 3.11, respectively. The magnitude of these cross sections decreases as more channels are included in the open-channel space, as expected. As is the case for the elastic DCSs, the low-lying channel seem to compete more actively for the flux that defines these cross sections than the higher-lying channel,

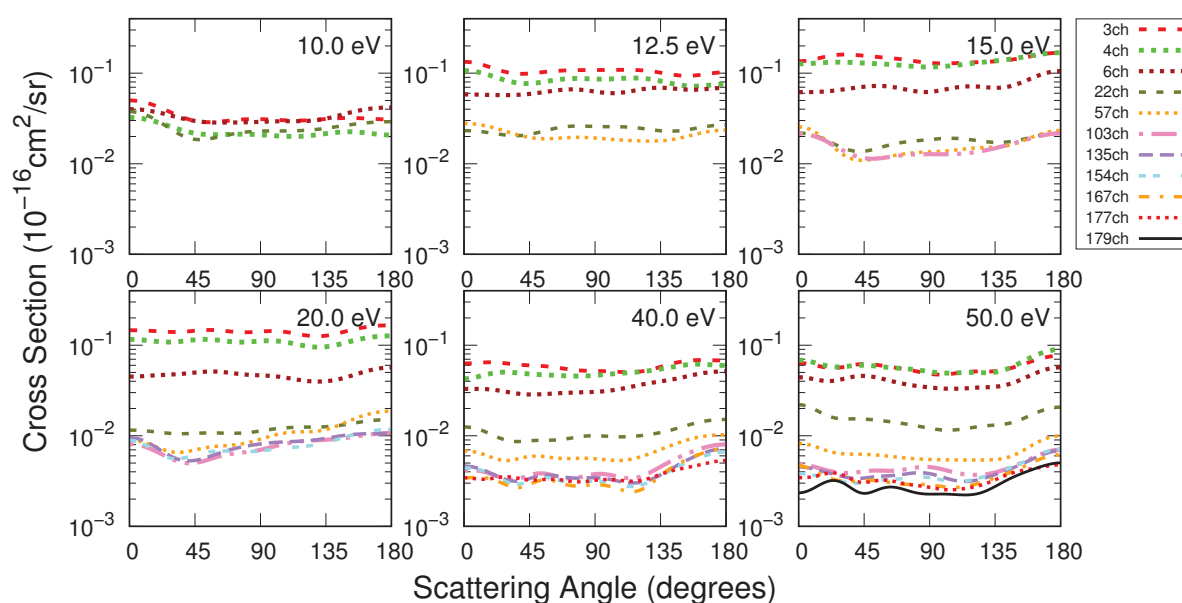


Figure 3.8 – DCSs for the electronic excitation of the $1^3A'$ (5.572 eV) state of formamide. The color code follows Fig. 3.2: Dashed red line, 3ch; dashed green line, 4ch; dashed brown line, 6ch; dashed olive line, 22ch; dotted orange line, 57ch; dash-dot-dot pink line, 103ch; long-dashed purple line, 135ch; double-dotted cyan line, 154ch; dot-dashed orange line, 167ch; dotted red line, 177ch; solid black line, 179ch.

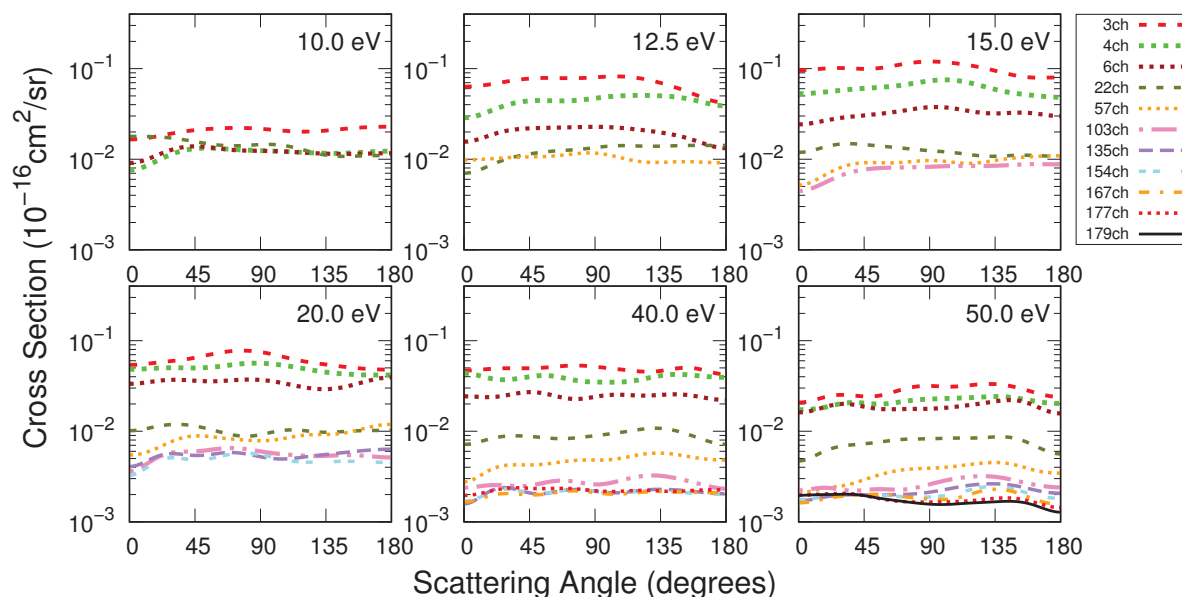


Figure 3.9 – Same as in Fig. 3.8, but for the $1^3A''$ (5.841 eV) state

that is, the DCSs changes more noticeably when low-lying electronically excited states are included in the projector operator P than when higher-lying states are included. Furthermore, in some cases, the DCSs calculated with fewer open channels have a lower magnitude than the ones calculated with a larger open channel space. These inversions are a result of pseudoresonances in the calculations with fewer open channels.

The electronic excitation from the ground state to the $1^1A''$ (6.416 eV) states is dipole-allowed and, as a consequence, long-ranged interactions play a significant role in the scattering process. The Born-closure procedure was not performed and we expect the DCSs reported in Fig. 3.10 to be underestimated for low scattering angles (below

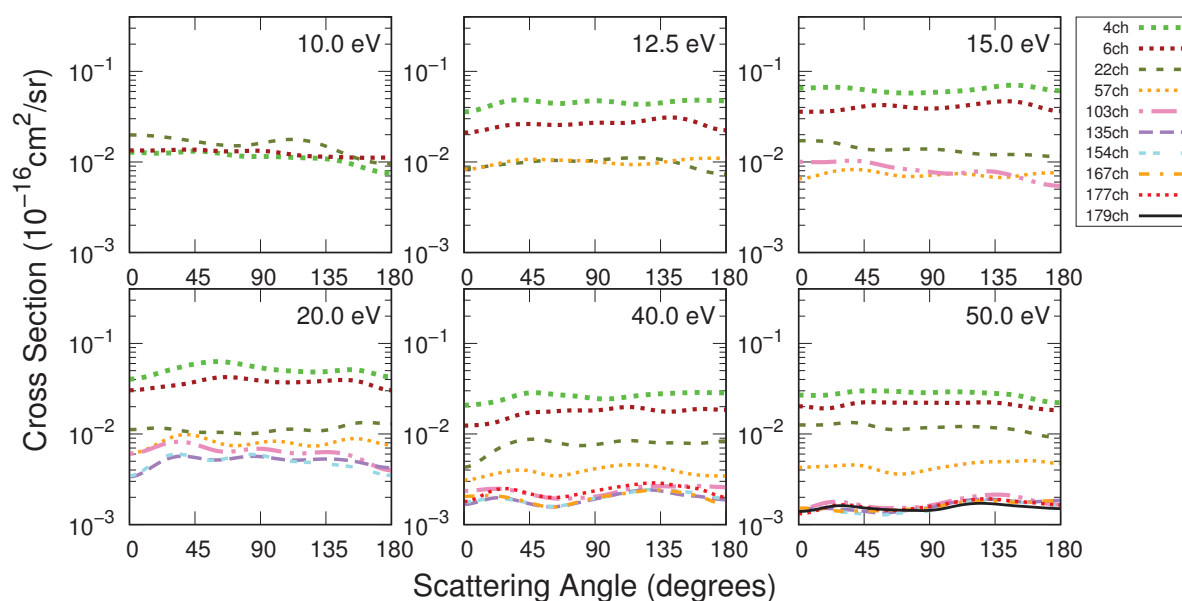


Figure 3.10 – Same as in Fig. 3.8, but for the $1^1A''$ (6.416 eV) state

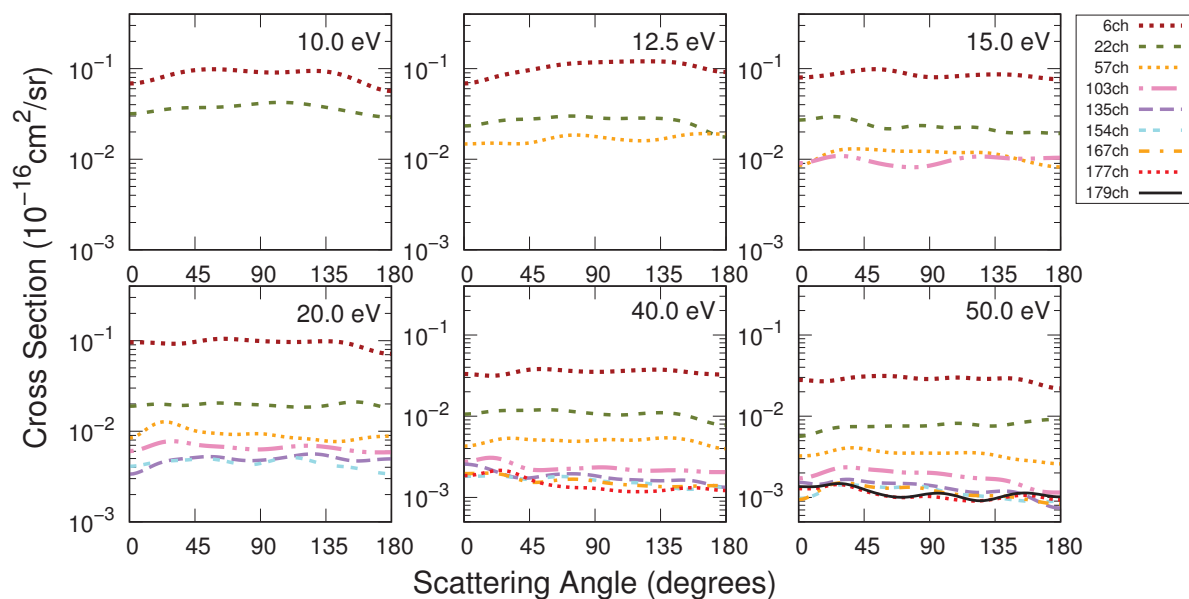


Figure 3.11 – Same as in Fig. 3.8, but for the $2^3A''$ (7.540 eV) state

20 degrees). Here, in the calculations regarding the electron scattering by methane depicted in the next chapter, and in recent applications of the SMCPP method [118–120] the electronically inelastic cross sections calculated with the Born-closure procedure fails to describe the scattering for higher angles, i.e., the cross sections calculated with and without the procedure do not match for higher scattering angles. This makes the selection of the l_{SMC} in the expression given in equation (C.2) impossible, and thus we are not able to perform the Born-closure procedure for these electronically inelastic channels.

The ICSs for the electronic excitation from the ground state to the $1^3A'$ (5.572 eV), $1^3A''$ (5.841 eV), $1^1A''$ (6.416 eV) and $2^3A''$ (7.450 eV) states of formamide are presented in Fig. 3.12, alongside the results of Wang and Tian [43] and Vinodkumar *et al.* [46]. These cross sections were obtained in the MC approximation, that is, the best multichannel coupling scheme following Tab. 3.4 was used in each energy regime. As is the case of the elastic ICS, between 6 and 20 eV, the cross sections present pseudoresonances and threshold effects associated with the high density of electronically excited states of formamide (and of closed channels that are energetically accessible) in this energy regime. However, the electronically inelastic cross sections are orders of magnitude smaller than the elastic cross sections. As a consequence, the electronically inelastic cross sections are more sensitive to these structures, thus appearing more pronounced in the electronically inelastic channels. Above 20 eV, the electronically inelastic MC ICSs are smooth and structures since only a few channels are treated as closed in the scattering calculations for most impact energies.

The comparison between the present electronically inelastic ICS and the results found in the literature is far from satisfactory. Due to pseudoresonances and threshold

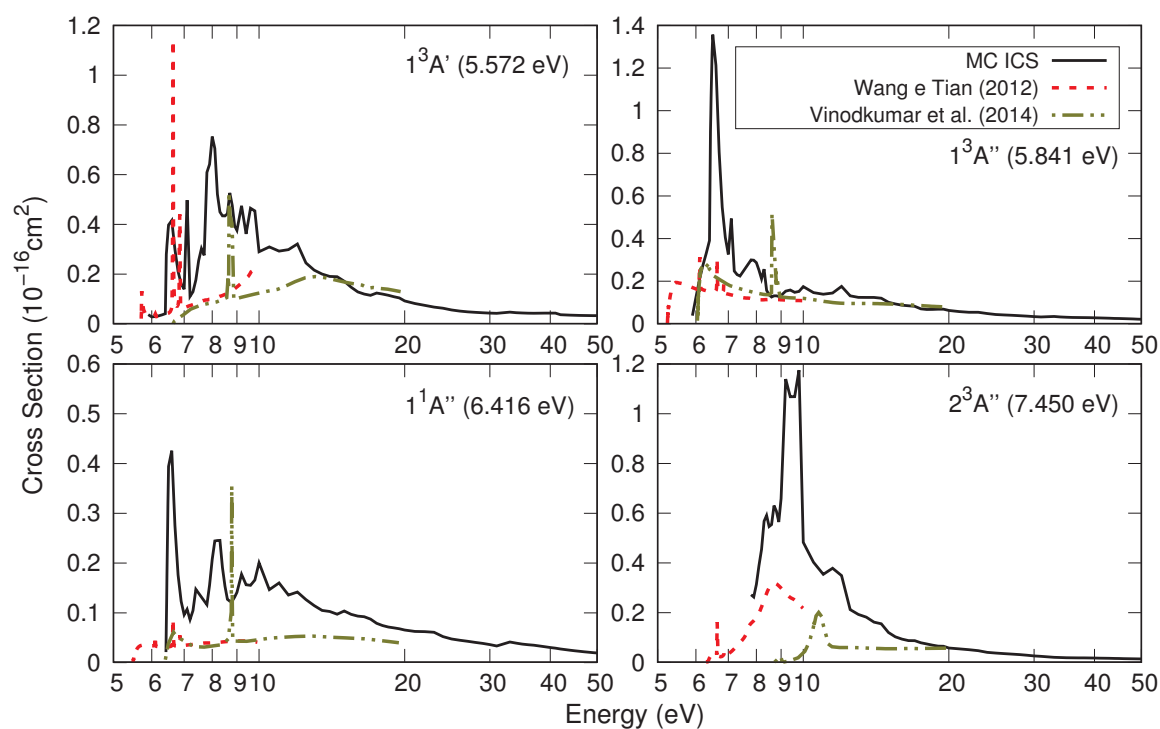


Figure 3.12 – ICSs for the excitation of formamide to the $1^3A'$ (5.572 eV), $1^3A''$ (5.841 eV), $1^1A''$ (6.416 eV) and $2^3A''$ (7.450 eV) states. Full black line, present MC results; dashed red line, results from Wang and Tian (R-Matrix) [43]; dash-double-dotted olive line, results from Vinodkumar *et al.* (R-Matrix) [46].

effects that appear in our ICSs, we cannot assign structures to core-excited or Feshbach resonances with certainty. Nevertheless, note also that although performed with the

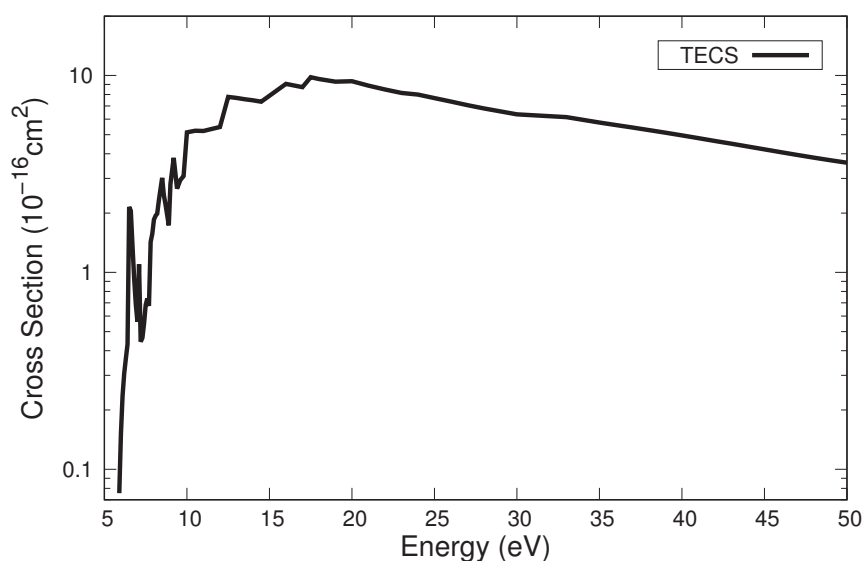


Figure 3.13 – TECS for the electron scattering by formamide. This cross section was obtained summing all the electronically inelastic ICSs.

same method, both R-matrix results from the literature do not agree amongst themselves in regards to the number, position and character of the resonances found in the electronically inelastic cross sections. Wang and Tian [43] found 3 Feshbach and 1 mixed core-excited shape resonance while Vinodkumar *et al.* [46] found 2 Feshbach and 3 mixed core-excited shape resonances. Furthermore, the low-magnitude of the electronically inelastic cross sections enhances their sensitivity to the computational details used in the scattering calculations. For instance, the threshold of the cross sections depends directly upon the description of the electronically excited state of the molecule. Thus, different approaches for the description of the electronically excited states of the molecule lead to distinct cross sections. These results emphasize the challenges of dealing with electronically inelastic scattering calculation from the theoretical point of view, where the cross sections and resonances are extremely sensitive to the description of the electronically excited states, to the multichannel coupling treatment and to the other computational details involved in the calculations.

Finally, the total excitation cross sections (TECS) for formamide calculated as the sum of all electronically inelastic ICSs are presented in Fig. 3.13. Once again, non-physical pseudoresonances and threshold effects can be observed for impact energies below 20 eV while the cross section is smooth for higher impact energies.

3.4 Total ionization cross section

In order to estimate a total cross section for formamide we also need to take into account the ionization processes that may occur. Since the ionization channel is not yet implemented in the SMCPP method, the TICS was obtained with the BEB model. As a consequence, the ionization channel does not compete for the flux that defines the cross sections already presented in this chapter, nor the cross sections calculated with the SMCPP method compete for the flux that defines the TICS. The present TICS, the TICS from Gupta [44] and the TACS from Homem *et al.* [45] are presented in the Fig. 3.14. The present TICS has a maximum at 91 eV and agrees well with the results of Gallup [50], underestimating the results from Homem *et al.* [45]. This is expected since the TACS involves channels beyond the single ionization channel.

3.5 Total cross sections

The TCS is calculated as the sum of the elastic MC ICS (calculated with the Born-closure procedure), the TECS and the TICS. The TCS is presented in Fig. 3.15 alongside results from the literature [45, 46]. The qualitative behaviour of the cross

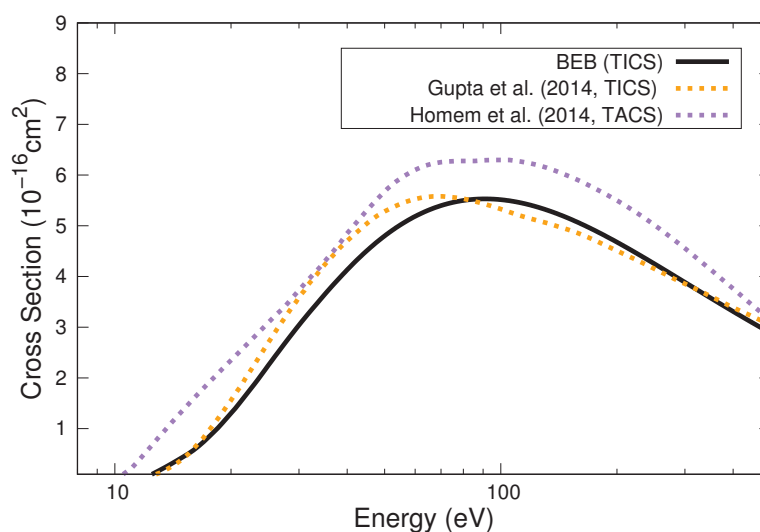


Figure 3.14 – Full black line, present TICS; dashed orange line, TICS from Gupta *et al.* (BEB) [44]; and dashed purple line, TACS from Homem *et al.* (SCE+Padé) [45].

section is analogous to the ICS depicted in Fig. 3.7. A good agreement with the results from Homem *et al.* [45] is found, while the present TCS overestimates the one reported by Vinodkumar *et al.* [46]. We also point out that although Vinodkumar *et al.* [46] performed the Born-closure procedure in their calculations, the TCS reported by these authors is close in magnitude to the elastic ICS calculated without the Born-closure procedure in the present work.

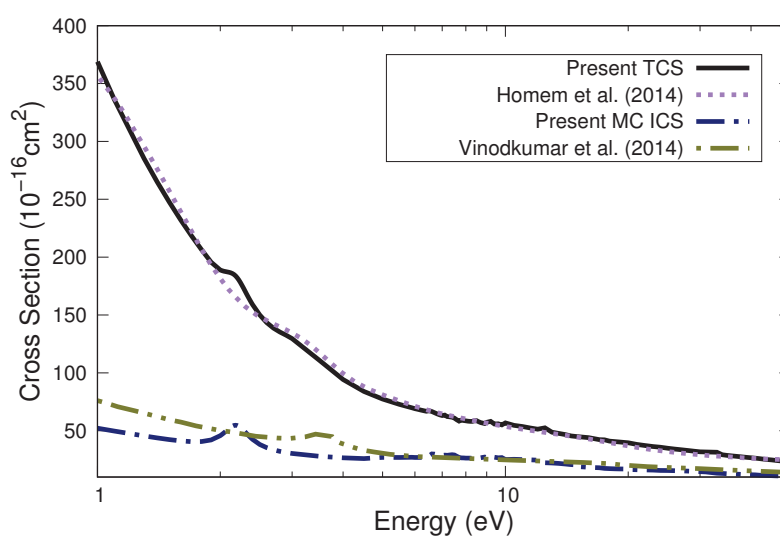


Figure 3.15 – TCS for the electron scattering by formamide. Full black line, present TCS; dashed purple line, TCS from Homem *et al.* (SCE+Padé) [45]; dash-double-dotted olive line, TCS from Vinodkumar *et al.* (R-Matrix) [46]; dashed-dotted blue line, elastic ICS calculated without the Born-Closure procedure.

3.6 Conclusion

In this chapter, the elastic and electronically inelastic electron scattering cross sections by formamide were presented and discussed. These calculations were performed with up to 179 open channels through the MOB-SCI approach. The multichannel coupling effect was observed in our results, where the cross sections magnitude decreased with an increasing number of open channels in the scattering calculations. Regarding the elastic channel, the qualitative comparison between our elastic DCSs and those reported in the literature [43, 45–47] is far from satisfactory. However, these discrepancies are less pronounced when comparing the ICSs. Particularly, the well-known shape resonance of formamide is well positioned in energy in our calculations, indicating a good description of the polarization effects. On the other hand, the vast quantity of pseudoresonances and threshold effects allied to the sensitivity of the electronically inelastic cross sections makes the comparison between our results and the ones from the literature [43, 46] far from satisfactory. Additionally, the TICS and TCS were also presented.

CHAPTER 4

Methane

In this chapter the elastic and electronically inelastic electron scattering cross sections by methane (Fig. 4.1) are going to be presented and discussed. As with the other molecules explored throughout this dissertation, this project was a collaborative effort, with the participation of Professors Giseli Maria Moreira and Romarly Fernandes da Costa. The results presented here have been submitted for publication in the *Journal of Applied Physics*.

Methane is one of the simplest polyatomic molecules that exists, being composed of a carbon atom surrounded by four hydrogen atoms. From an applied perspective, this system has important uses in technological fields, such as in plasma enhanced chemical vapor deposition [52, 53]. Besides that, methane is also a molecule widely distributed in the interstellar medium [54, 55]. Thus, electron-methane interactions are

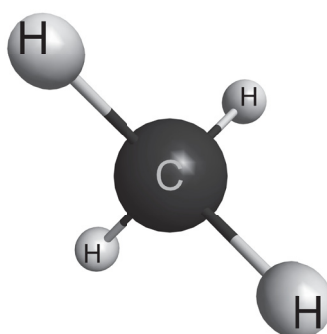


Figure 4.1 – Schematic representation of the chemical structure of methane (generated with MacMolPlt [35]).

relevant for both technological and astrophysical modelling. Additionally, methane is a potent greenhouse gas in the Earth's atmosphere contributing to global warming [56]. Therefore, it is essential to adopt measures to minimize its emissions.

Because of methane's simplicity and many applications its interaction with electrons has been comprehensively investigated. A thorough survey of the literature can be found in the works of Fuss *et al.* [57], Song *et al.* [58] and Gadoum and Benyoucef [59], and here only a few representative works are mentioned.

Extensive investigation into the elastic electron scattering by methane has been conducted through theoretical and experimental studies. Gianturco and Thompson [60] reported in 1976 the partial contributions of the T_2 , A_1 and E symmetries to the total cross section for the scattering of electrons by methane, finding a RT minimum at low-impact energies. Lengsfield *et al.* [61] investigated the electron-methane interactions between 0.2 and 10 eV with the complex Kohn method, reporting integral (ICS) and differential (DCS) elastic cross sections. Nestmann *et al.* [62] calculated the ICS and DCSs for the elastic scattering of electrons by methane with the R-matrix method. Gianturco *et al.* [63] using a single center expansion of the close-coupled equations reported DCSs and the ICS around the RT minimum of methane. Using an extension of the single-center approach, Althorpe *et al.* [64] investigated the vibrational excitation of methane by electron impact, reporting the elastic ICS. Bettega *et al.* [65] reported the ICS and DCSs for elastic scattering of electrons by methane calculated with the Schwinger multichannel (SMC) method implemented with pseudopotentials (SMCPP). Finally, Vinodkumar *et al.* [66] reported the ICS for the elastic channel obtained through a combination of the R-matrix and the spherical complex optical potential formalism.

Experimentally, Sohn *et al.* [67] studied the electron-methane interactions reporting elastic DCSs and ICS between 0.2 and 5.0 eV. Shyn and Cravens [68] measured the elastic DCSs and, from these measurements, estimated the ICS for impact energies between 5 and 50 eV. Boesten and Tanaka [69], using a crossed beam spectrometer, reported absolute elastic ICS, DCSs and momentum-transfer cross section (MTCS) for the scattering of electrons by methane up to 100 eV. Finally, Cho *et al.* [33], through a joint theoretical and experimental effort, studied the elastic scattering of electrons by methane, reporting the ICS, DCSs and MTCS measured and calculated using the iterative Schwinger variational method (ISVM) combined with the distorted-wave approximation and a complex optical potential (COP).

On the other hand, when looking at the electronically inelastic channels, the story is different. As mentioned in the introduction of this dissertation, the study of the electronic excitation processes poses a challenging task, and the lack of electronically inelastic cross sections reported in the literature for most molecules reflects that. The only experimental electronic excitation cross sections available are the ones reported

by Vušković and Trajmar [70], which were measured for unresolved bands of methane. These cross sections were obtained from the measured inelastic to elastic scattering intensity ratios and from the measured elastic DCSs that were normalized to the early results of Tanaka *et al.* [121] at 100°. Unfortunately, Tanaka's group later discovered that their early measurements fall systematically short of the direct measured total cross sections available in the literature, which motivated the more recent and reliable measurements previously mentioned [69]. Hence, Vušković and Trajmar [70] cross sections are not as reliable as one wished. From the theoretical side, the simplicity of methane enabled more cross sections to be reported, but these calculations were limited to only a few simultaneously open channels. Winstead *et al.* [71], through the SMC method, calculated cross sections for the excitation of methane to its first triplet and singlet electronically excited states in calculations involving 2, 3 and 7 open channels. Gil *et al.* [72] reported integral electronically inelastic cross sections for methane calculated with different multichannel coupling schemes using the complex Kohn method including up to 55 channels. Bettega *et al.* [73] reported the electronically inelastic integral cross section for the excitation of the first triplet state of XH_4 ($X=C, Si, Ge, Sn, Pb$) molecules using the SMCPP method in a two-channel calculation. Joshipura *et al.* [74] reported the total excitation cross section for methane amidst a set of tetrahedral molecules and SF_6 by using the complex scattering potential-ionization contribution formalism. Ziólkowski *et al.* [75] investigated the neutral dissociation of methane and presented, in addition to the elastic ICS, the integral excitation cross sections for 9 electronically excited states of methane calculated with the R-matrix method including 24 channels in their calculations.

The ionization of methane due to electron impact has also been studied in the literature. In addition to the reviews mentioned above [57–59], we also call attention to the works of Kim *et al.* [122] and Deutsch *et al.* [123], that calculated in the total ionization cross section of methane amongst other molecules with the BEB model and the Deutsch–Märk (DM) formalism, respectively.

Here, we intend to further investigate the scattering of electrons by methane, focusing on the electronic excitation of the molecule and in the inclusion of the multi-channel coupling effects in the scattering calculations. We present the ICSs and DCSs for the elastic and electronically inelastic channels calculated by using the SMCPP method within the minimal-orbital basis for single configuration interaction (MOB-SCI) strategy, with up to 181 open channels. These represent an update of the previous cross sections obtained with the SMC [71] and SMCPP [65, 73] methods. The previous results were computationally limited and considered only a few open channels. In contrast, recent computational advances, allied to the parallelization and optimization of the code, enabled us to compute the electron scattering cross sections taking into account a larger number of electronically inelastic channels in the scattering calculations. Additionally, we

also present the total ionization and total cross sections for the scattering of electrons by methane.

4.1 Computational Details

Methane, being a tetrahedral molecule, belongs to the T_d point group, resulting in doubly- or triply-degenerated electronically excited states. However, since the SMC method only deals with abelian groups, the calculations were carried out in the C_{2v} point group. To obtain the electronically inelastic cross section for the excitation of methane to a doubly- or triply-degenerated state, we summed the cross sections calculated for each component of these states according to the C_{2v} point group. Consequently, three distinct scattering channels are associated with excitations to a single triply-degenerated state and two scattering channels are associated with doubly-degenerated states. The correspondence between the T_d and C_{2v} point groups is presented in Table 4.1.

All calculations were performed in the same geometry ($R_{\text{CH}} = 2.05a_0$) used in Ref. [73]. For the calculations carried out with the SMC method, the basis set of Ref. [73] was used to describe the valence electrons of carbon and hydrogen atoms. This basis set contains $6s$, $4p$ and $3d$ CG functions for the C atom and uses Dunning's basis set [106], with one additional p -type function with exponent 1.0 for the hydrogen atoms. Additionally, $3s$ and $3p$ diffuse Cartesian Gaussian (CG) functions were added to four charge-less extra centers that together with the hydrogen atoms form a cube around the carbon atom. These extra CG functions aid in the description of methane's more diffuse electronically excited states of Rydberg character. The exponents of the CG functions used for the C and extra centers can be found in Table 4.2.

The electronic configuration of methane's ground state according to the C_{2v} point group is $(core)^2(1a_1)^2(2a_1)^2(1b_1)^2(1b_2)^2$, where the three highest molecular orbitals are degenerated (t_2 symmetry). The improved virtual orbitals (IVOs) [94] used to represent the unoccupied molecular orbitals for the scattering and MOB-SCI calculations were generated with triplet spin-coupling and the $(1a_1)$ molecular orbital was used as hole orbital in order to preserve degeneracy.

Table 4.1 – Relation between the irreducible representations of the T_d and C_{2v} point groups.

T_d	C_{2v}
A_1	A_1
A_2	A_2
E	$A_1 + A_2$
T_1	$B_1 + B_2 + A_2$
T_2	$A_1 + B_1 + B_2$

Table 4.2 – Exponents of the basis functions used in the C atom and extra centers.

Type	Carbon	Extra Centers
<i>s</i>	7.979510	1.600000
<i>s</i>	3.277998	0.400000
<i>s</i>	0.520826	0.100000
<i>s</i>	0.168132	-
<i>s</i>	0.041465	-
<i>s</i>	0.019352	-
<i>p</i>	4.985125	0.320000
<i>p</i>	1.382734	0.080000
<i>p</i>	0.416258	0.020000
<i>p</i>	0.118249	-
<i>d</i>	1.800000	-
<i>d</i>	0.600000	-
<i>d</i>	0.200000	-

As mentioned previously, the MOB-SCI [93] approach was used to describe the electronically excited states of the molecule in the scattering calculations. Out of the 416 hole-particle pairs employed in the FSCI calculation, 90 were chosen for expanding the wave function within the MOB-SCI approach. This selection was made in order to accurately describe the first 73 electronically excited states obtained with the FSCI calculation. As was done for formamide in chapter 3, to evaluate the quality of these results an additional all-electron EOM-CCSD [107–110] calculation with the aug-cc-pVDZ basis set was performed using the computational software Psi₄ [111]. The vertical excitation energies obtained with the FSCI, MOB-SCI and EOM-CCSD/aug-cc-pVDZ calculations and previous results from the literature [71–73, 75, 124–127] for the first few electronically excited states of methane are presented in Table 4.3. We found an excellent agreement between the MOB-SCI and FSCI vertical excitation energies indicates that the MOB-SCI approach accurately reproduces the states obtained from the FSCI calculation. Additionally, we observe a good agreement between the vertical excitation energy of each individual state obtained through the single-configuration interaction calculation and those obtained using the more robust EOM-CCSD/aug-cc-pVDZ method. This suggests that the single-configuration interaction approximation effectively describes the first few electronically excited states of methane. A good agreement is also found with other theoretical results from the literature [71–73, 75, 124]. However, the agreement with experimental results obtained from measured spectra [125–127] is not as good. These discrepancies are expected and can be attributed to nuclear motion in the excited states associated with the Jahn-Teller distortion that occurs in the first triplet and singlet excited states of methane (1^3T_2 and 1^1T_2). Since the calculations are performed within the fixed-nuclei approximation, they do not account for the relaxation of molecular ge-

Table 4.3 – Excitation energies (in eV) of the first few electronically excited states of methane. Results for the vertical excitation energies calculated with the FSCI, MOB-SCI and EOM-CCSD/aug-cc-pVDZ are compared to previous theoretical results from Winstead *et al.* (IVOs) [71], Gil *et al.* (IVOs) [72], Bettega *et al.* (IVOs) [73], Ziólkowski *et al.* (CASCI) [75] and Mebel *et al.* (MRCI+D) [124] and to experimental results obtained from the maximum in the structures of the measured spectra (Expt.) [125–127]. See text for a detailed discussion.

States	FSCI	MOB-SCI	EOM-CCSD	Ref. [71]	Ref. [72]	Ref. [73]	Ref. [75]	Ref. [124]	Expt.
1^3T_2	10.334	10.535	10.163	10.86	10.93	10.84	11.296	10.2480	8.8 [127]
1^3A_1	11.051	11.532	11.133		12.06		12.251		
1^1T_2	11.102	11.147	10.566	11.24	11.25		12.349	10.6440	9.65-10.33 [125], 9.65-10.31 [126]
2^3T_2	12.211	12.258	11.732		12.26		13.607		
1^3E	12.262	12.297	11.882		13.13		14.224		
1^3T_1	12.345	12.357	12.006		12.45		14.338		
1^1E	12.354	12.381	11.962		12.41				
2^1T_2	12.370	12.404	11.852		12.38		14.409	11.9	11.61 [126]
1^1T_1	12.373	12.383	11.998		12.45		14.566		
3^3T_2	12.560	12.672	12.663		13.45				
2^3A_1	12.598	12.824	12.201		12.98				
3^1T_2	13.128	13.342	13.588		13.45				

ometry caused by electronic excitation and, thus, a comparison between the calculated vertical excitation energies and the structures observed in measured spectra is not straightforward. Additional evidence that supports that nuclear relaxation may be the responsible of such discrepancies can be seen in the work of Mebel *et al.* [124], where the authors investigated possible photodissociation pathways of methane. Amidst their findings, they showed a clear difference between the geometries of the 1^1T_2 electronically excited state and the ground state of the molecule, that the 1^3T_2 is purely dissociative and also a large discrepancy between the vertical and adiabatic excitation energies to these states. Therefore, the use of the Born-Oppenheimer approximation in the present calculations largely contributes to the disagreement between the theoretical predictions and experimental measurements presented in Table 4.3. To rectify these differences it would be necessary to include the nuclear motion in the calculations, which is beyond the scope of the present work.

To perform the scattering calculations with the SMC method, one needs to define the CSFs and the projector operator P in equation (2.53). In the present work we performed the calculation with two distinct configuration spaces. In the first one, the same set of 90 hole-particle pairs used in the MOB-SCI calculation is used to construct the CSFs and all unoccupied IVOs are used as scattering orbitals. As was done before, this level of calculations is denoted as the multichannel coupling (MC) approximation. The number of CSFs of each symmetry according to the C_{2v} point group is presented in Table 4.4. With this configuration space, distinct calculations were performed with a different number of electronically excited states being included in the open channel space. These are denoted as $N_{open} ch$, where N_{open} is the number of channels that are treated as open in that level of calculation. Once again, it is important to note

Table 4.4 – Number of configurations of each symmetry according to the C_{2v} point group used in the scattering calculations. MC: configuration space constructed with 90 hole-particle pairs and all unoccupied molecular orbitals as scattering orbitals; FSCI: configuration space constructed using all occupied and unoccupied molecular orbitals as hole, particle and scattering orbitals.

Symmetry	MC	1ch-FSCI
A_1	2517	12017
A_2	2211	9671
B_1	2368	10840
B_2	2368	10840
Total	9464	43368

that since methane belongs to the T_d point group, two or three electronically inelastic scattering channels are associated with the doubly- or triply-degenerated states of the molecule, respectively. We indicate the distinct levels of multichannel coupling used in our calculations in Fig. 4.2. The calculations with 4, 7 and 8 open channels are performed to obtain the excitation cross section to the low-lying electronically excited states of methane from their thresholds. The calculations with 24, 97 and 175 open channels provide the most complete treatment of multichannel coupling for the impact energies of 12.5, 15.0 and 20.0 eV, respectively. The calculations with 61, 129, 132 and 153 open channels are related to groups of closely lying states and the 181ch calculation treats all electronically excited states obtained within the MOB-SCI approach as accessible during the scattering process. A 1ch calculation (not shown in Fig. 4.2) was also performed where only the elastic channel is treated as open in the scattering process. From these results, we select the best multichannel coupling in each energy regime to obtain the final MC cross sections. The multichannel coupling scheme considered for each incident electron impact energy can be found in Table 4.5. For energies below 10.535 eV only the elastic channel is energetically accessible, and the 1ch calculation is used to obtain the MC cross section. For impact energies between 10.535 eV and 11.148 eV the results obtained with the 4ch calculation were used to obtain the MC cross sections, for energies between 11.148 eV and 11.553 eV the 7ch results were used, and so on. This calculation includes in addition to the polarization effects the multichannel coupling effects, providing a good description of the scattering for low- and high-impact energies. In order to be concise, only the cross sections obtained within the 1ch and MC approximations are going to be presented in this chapter, since the comparison between the intermediate levels of calculation is the same as the one discussed for formamide in chapter 3.

Since methane is a small molecule we were also able to perform a second calculation with a more robust configurational space. In this calculation, all occupied molecular orbitals are used as hole and all unoccupied IVOs are used as particle and scattering orbitals in the construction of the CSF space. In Table 4.4 the number of

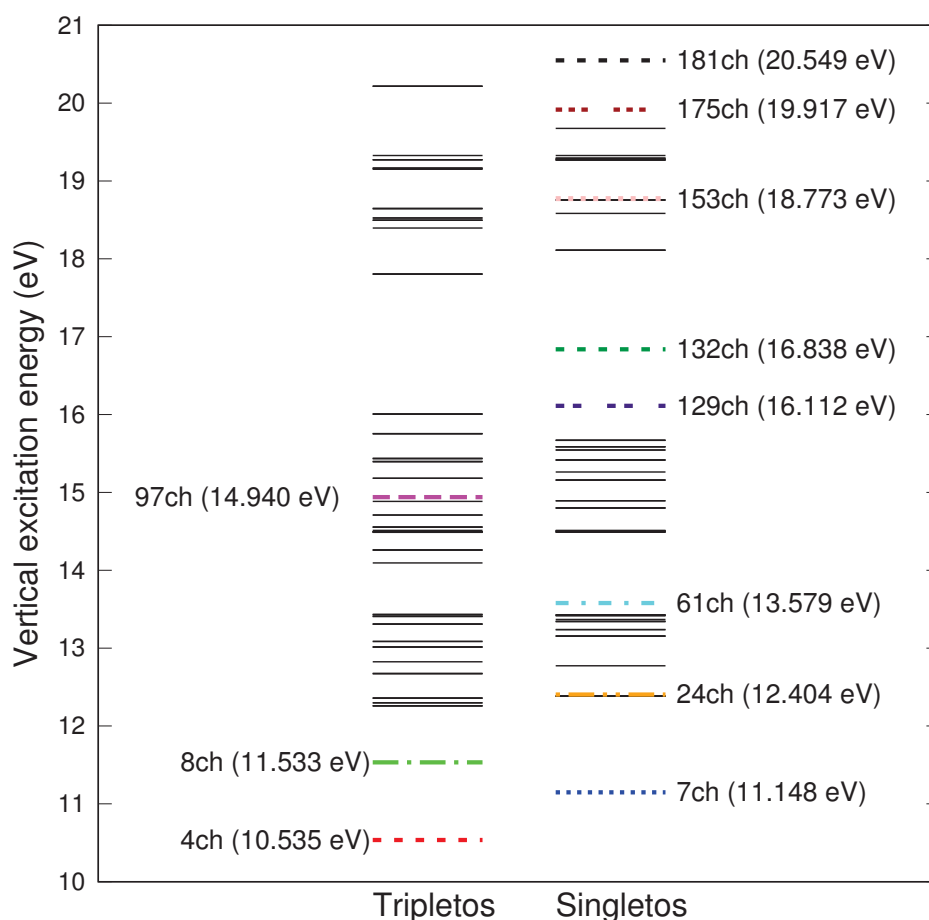


Figure 4.2 – Schematic representation of the vertical excitation energies (in eV) of the 180 electronically excited states (according to the C_{2v} point group) of methane obtained with the MOB-SCI calculation and the different multichannel coupling strategies employed in the scattering calculations. The lines in color indicate the best level of channel coupling at the energy shown in parenthesis. The dashed red line corresponds to the threshold of the 4ch scattering calculation; dotted blue line, 7ch; dash-dotted green line, 8ch; dash-dot-dotted orange line, 24ch; small-dash-dotted cyan line, 61ch; dashed magenta line, 97ch; double-dashed purple line, 129ch; small-dashed olive line, 132ch; dashed pink line, 153ch; triple-dotted brown line, 175ch; and dotted black line, 181ch.

CSFs per symmetry according to the C_{2v} point group is presented. In the scattering calculations, the polarization effect arises from the closed-channel space introduced by the inclusion of single virtual excitations in the CSFs construction. This effect is especially important at low-impact energies. Thus, since this second calculation was performed with the most robust CSF space possible within the chosen basis set, we expect it to describe the low-energy electron scattering very well. However, since all possible single excitations are used, the electronically excited states of the molecule are being described within the FSCI approximation. Consequently, a large number of electronically excited states is obtained, and due to computational restraints we

Table 4.5 – Channel coupling strategies used for each electron impact energy (in eV) interval to compute the final cross sections obtained in the multichannel coupling (MC) approximation.

Electron impact energy	MC level	Electron impact energy	MC level
0.1 to 10.535	1ch	14.940 to 16.112	97ch
10.535 to 11.148	4ch	16.112 to 16.838	129ch
11.148 to 11.533	7ch	16.838 to 18.773	132ch
11.533 to 12.404	8ch	18.773 to 19.917	153ch
12.404 to 13.579	24ch	19.917 to 20.549	175ch
13.579 to 14.940	61ch	20.549 to 50.000	181ch

were able to include only the ground state in the construction of the projector operator P , leading to a purely elastic calculation. Nevertheless, the results obtained in this approximation provides a good description of the elastic scattering and are also useful to evaluate the quality of the polarization effect description in the calculation mentioned in the last paragraph, where a reduced CSF space was used. Hereafter, the cross sections obtained in the calculation performed with this configurational space are referred to as 1ch-FSCI.

To obtain the parameters used in the calculation of the TICS through the BEB model we have performed a HF/aug-cc-pVQZ calculation using the GAMESS computational package [105]. Once again, it is important to remember that the ionization channel do not compete for the flux that define the cross sections obtained with the SMC method.

4.2 Elastic Channel

The elastic ICS for the electron scattering by methane calculated here at the 1ch, 1ch-FSCI and MC levels are depicted in Fig. 4.3. Below the first excitation threshold, the cross sections obtained with both configuration spaces are in qualitative and quantitative agreement, and effects that arise from the polarization in the scattering calculations, such as the well-known RT minimum of methane, are observed in both calculations. This indicates that the polarization effects are being well described by the reduced CSF space used in the 1ch and MC calculations. At higher impact energies the purely elastic 1ch and 1ch-FSCI calculations present pseudoresonances that vanish from the cross sections when electronically excited states are included in the open-channel space of the scattering calculations, resulting in a smooth MC cross section when all inelastic channels are treated as accessible during the scattering process, as expected. We recall that the same behaviour was observed for formamide in chapter 3. For intermediate impact energies, between 10 to 20 eV, the MC cross section still present

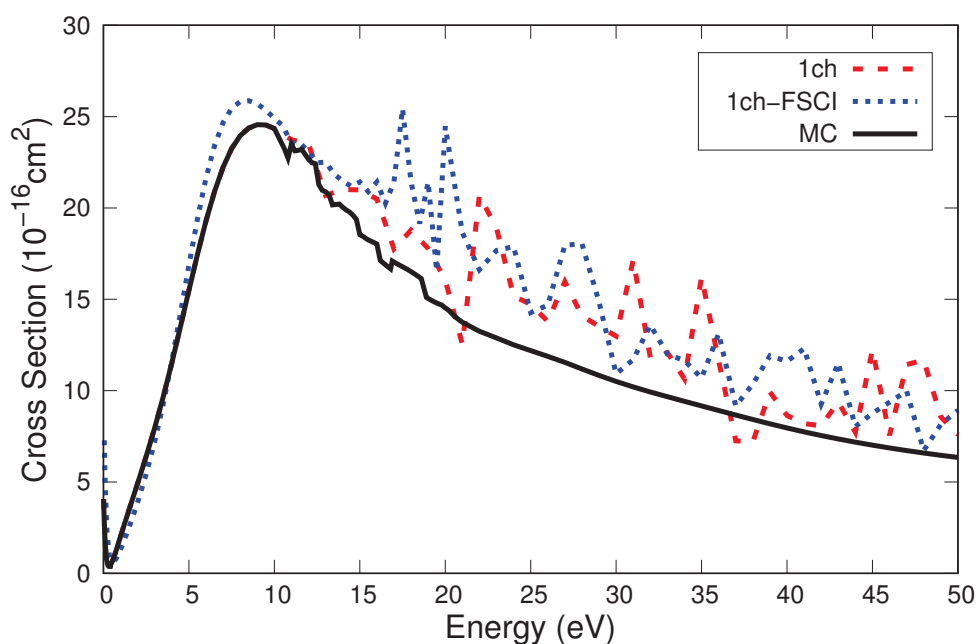


Figure 4.3 – Elastic integral cross section for electron scattering by methane. Dashed red line, 1ch result; dotted blue line, 1ch-FSCI; full black line, MC cross section.

some pseudoresonances, associated with energetically accessible channels that are still treated as closed, and threshold effects that lead to sudden small increases and decreases in the cross section. One can also observe the multichannel coupling effect when comparing the 1ch and MC ICSs.

In the upper panel of Fig. 4.4, the 1ch-FSCI and MC cross sections are compared with previous theoretical results from the literature [33, 61, 62, 64–66, 75]. A good agreement is found and the small discrepancies related to the position of the RT-minimum and shape resonance can be attributed to distinct treatments of the polarization effects in each calculation. In the lower panel of Fig. 4.4 a comparison between our 1ch-FSCI and MC results and the recommended cross sections [57, 58] and experimental data [33, 67–70] from the literature is made. An overall good agreement is also found here for the low-energy regime, notably between the 1ch-FSCI and the experimental results from Sohn *et al.* [67] and Boesten and Tanaka [69] around the region of the RT-minimum and the shape resonance. For higher impact energies the multichannel coupling effect improves the agreement with experimental data substantially, as can be seen in the comparison between the MC cross section and the results from the literature [33, 67–70]. Although a good agreement is generally found, a systematic overestimation of the recommended cross section of Fuss *et al.* [57] is observed for higher impact energies.

To analyze more thoroughly the low-energy scattering of electrons by methane, we present in Figs. 4.5 and 4.6 the ICSs calculated with the 1ch-FSCI and MC approxi-

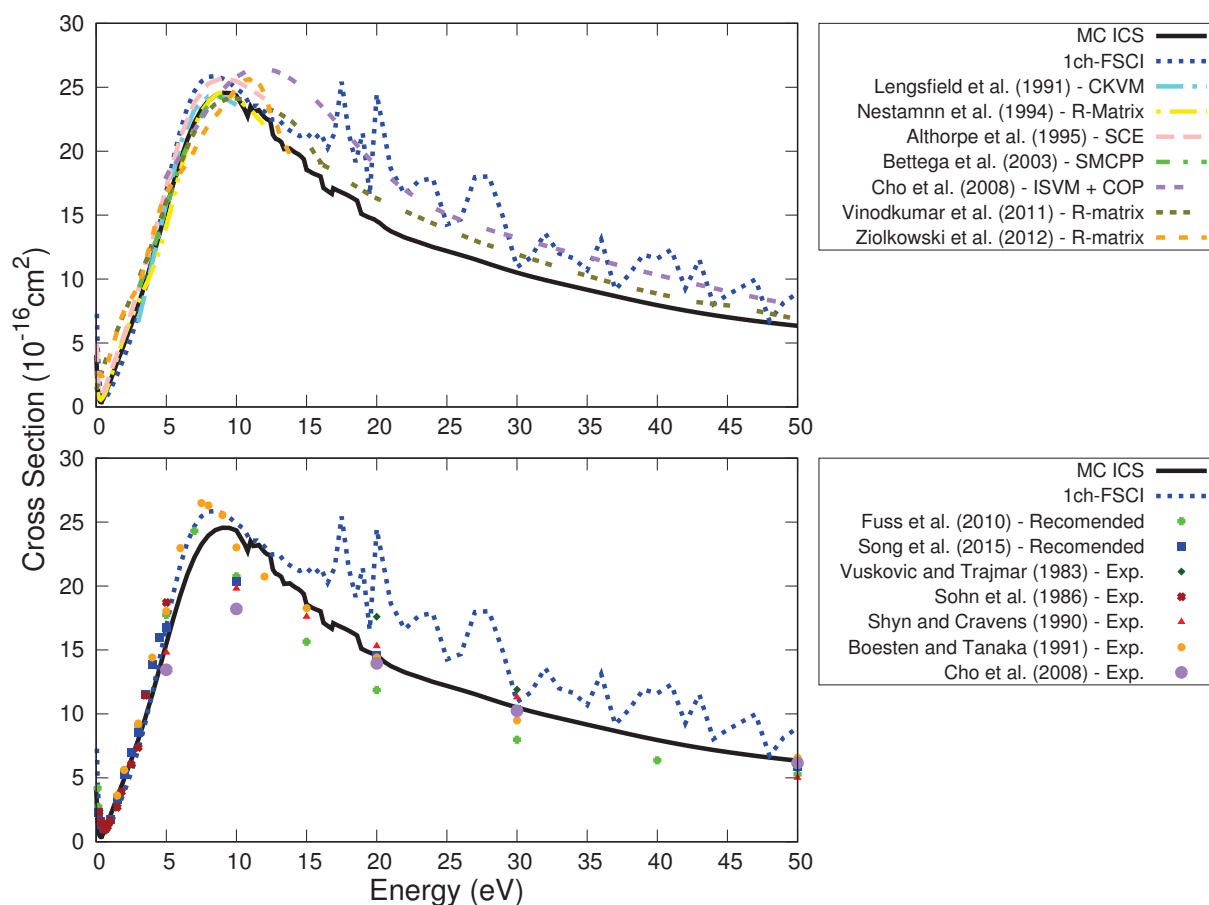


Figure 4.4 – Elastic integral cross section for electron scattering by methane compared with theoretical (upper panel) and experimental (lower panel) results. Upper panel: dotted blue line, 1ch-FSCI result; full black line, MC result; long-dash-dotted cyan line, Lengsfeld *et al.* (CKVM) [61]; dot-dash-dotted yellow line, Nestmann *et al.* (R-Matrix) [62]; dashed pink line, Althorpe *et al.* (SCE) [64]; dash-dot-dotted green line, Bettega *et al.* (SMCPP) [65]; double-dotted purple line, Cho *et al.* (ISVM + COP) [33]; dot-dot-dotted olive line, Vinodkumar *et al.* (R-Matrix) [66]; and dotted orange line, Ziółkowski *et al.* (R-Matrix) [75]. Lower panel: dotted blue line, 1ch-FSCI; full black line, MC results; green crosses, Fuss *et al.* (recommended) [57]; blue squares, Song *et al.* (recommended) [58]; brown crosses (x), Sohn *et al.* (Experimental) [67]; red triangles, Shyn and Cravens [68]; orange circles, Boesten and Tanaka (Experimental) [69]; open dotted purple dots, Cho *et al.* (Experimental) [33]; and dark-green diamonds, Vuškovic and Trajmar (Experimental) [70].

mations, the angular momentum decomposition of the ICS and the s -wave eigenphase up to 1 eV. The MC cross section tends to agree better with other theoretical results that reliably show a minimum in the cross section [62, 64] than the 1ch-FSCI approximation. However, when comparing the present calculations to the recommended cross sections [57, 58] and the experimental results [67] from the literature, we find a better agreement with the 1ch-FSCI calculation. This discrepancy arises from the different polarization strategies employed associated with the different configuration spaces used

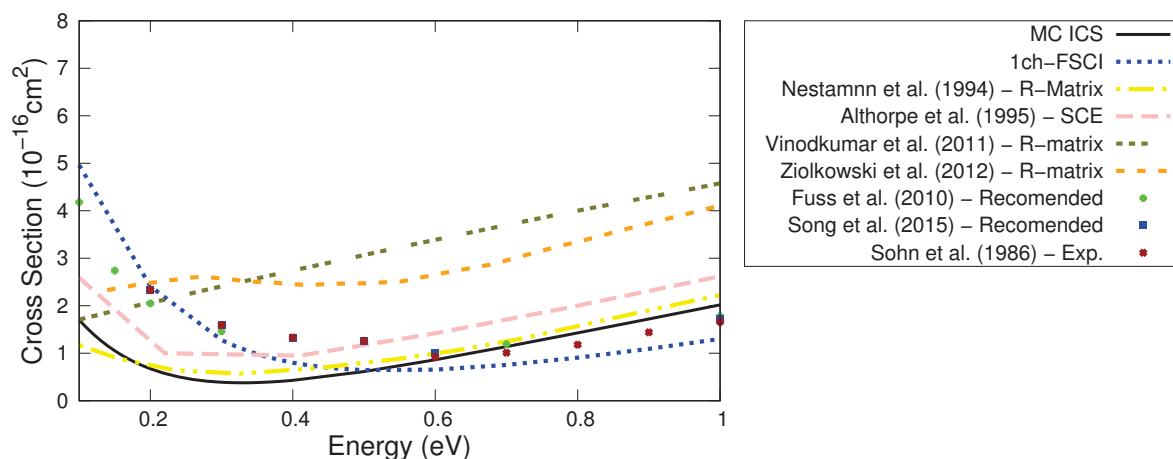


Figure 4.5 – Elastic integral cross section for energies below 1 eV calculated at the 1ch-FSCI approximation, dotted blue line; and MC level, full black line; alongside results from the literature: dot-dash-dotted yellow line, Nestmann *et al.* (R-Matrix) [62]; dashed pink line, Althorpe *et al.* (SCE) [64]; dot-dot-dotted olive line, Vinodkumar *et al.* (R-Matrix) [66]; dotted orange line, Ziolkowski *et al.* (R-Matrix) [75]; green crosses (+), Fuss *et al.* (recommended) [57]; blue squares, Song *et al.* (recommended) [58]; and brown crosses (x), Sohn *et al.* (Experimental) [67].

in each scattering calculation. The better agreement with experiment [67] indicates that these effects are more accurately described by the 1ch-FSCI calculation. From the partial wave analysis of the cross sections depicted in Fig. 4.6 it is clear that the minimum observed in the ICS is associated with the well known RT-minimum of methane, since the s -wave cross section tends to zero and the s -wave eigenphase changes sign at the same energy. This change in sign indicates that the net potential felt by the incoming electron changes from attractive to repulsive, characterizing the formation of a

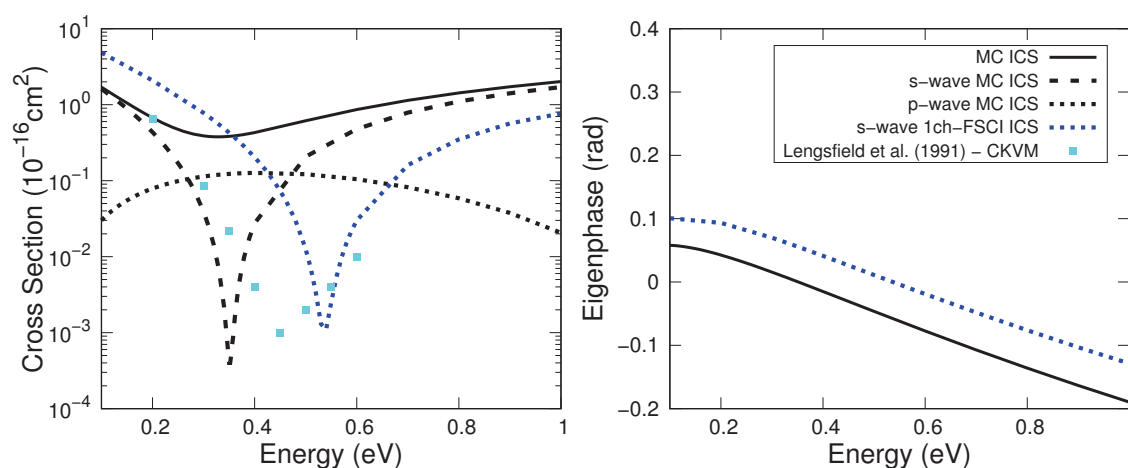


Figure 4.6 – Left panel: full black line, MC ICS; dashed black line, s -wave MC cross section; dotted black line, p -wave MC cross section; dotted blue line, s -wave 1ch-FSCI; cyan squares, Lengsfeld *et al.* (R-Matrix) [61]. Right panel: s -wave MC eigenphase; and dotted blue line, s -wave 1ch-FSCI eigenphase. The RT-minimum of methane is seen at 0.350 eV in the MC approximation and at 0.530 eV in the 1ch-FSCI calculation.

RT-minimum, which is located at 0.350 eV in the MC calculation. We also observe a predominance of the p -wave in the scattering energies around the RT-minimum, which explains the high magnitude of the ICS around this region. The same behaviour was observed for the 1ch-FSCI calculation, except that the minimum is centered at 0.530 eV. In Fig. 4.6 the results from Lengsfeld *et al.* [61] are also shown, and the difference in the position of the RT minimum between our calculations and their results can be attributed to the distinct treatment of the polarization effects.

The elastic DCSs for selected impact energies calculated at the 1ch, 1ch-FSCI and MC levels are presented in Fig. 4.7, 4.8 and 4.9 along with results from the literature [33, 58, 61, 65, 67–69]. Below the first excitation threshold (10.535 eV) the 1ch result is used to obtain the final MC cross section, therefore only the MC results are shown. For 0.5 and 1.0 eV the MC and 1ch-FSCI present distinct oscillatory behaviours due to the position of the RT-minimum in both levels of calculations. For these lower-impact energies, the MC results are in better agreement with the experimental data from Sohn *et al.* [67]. Between 3.0 and 12.0 eV all cross sections agree very well, except for a slightly overestimation of the experimental data from Shyn and Cravens [68] and Cho *et al.* [33] for scattering angles above 120 degrees. Additionally, at 3.0 and 5.0 eV, the 1ch-FSCI calculation shows a slightly better description of the forward scattering

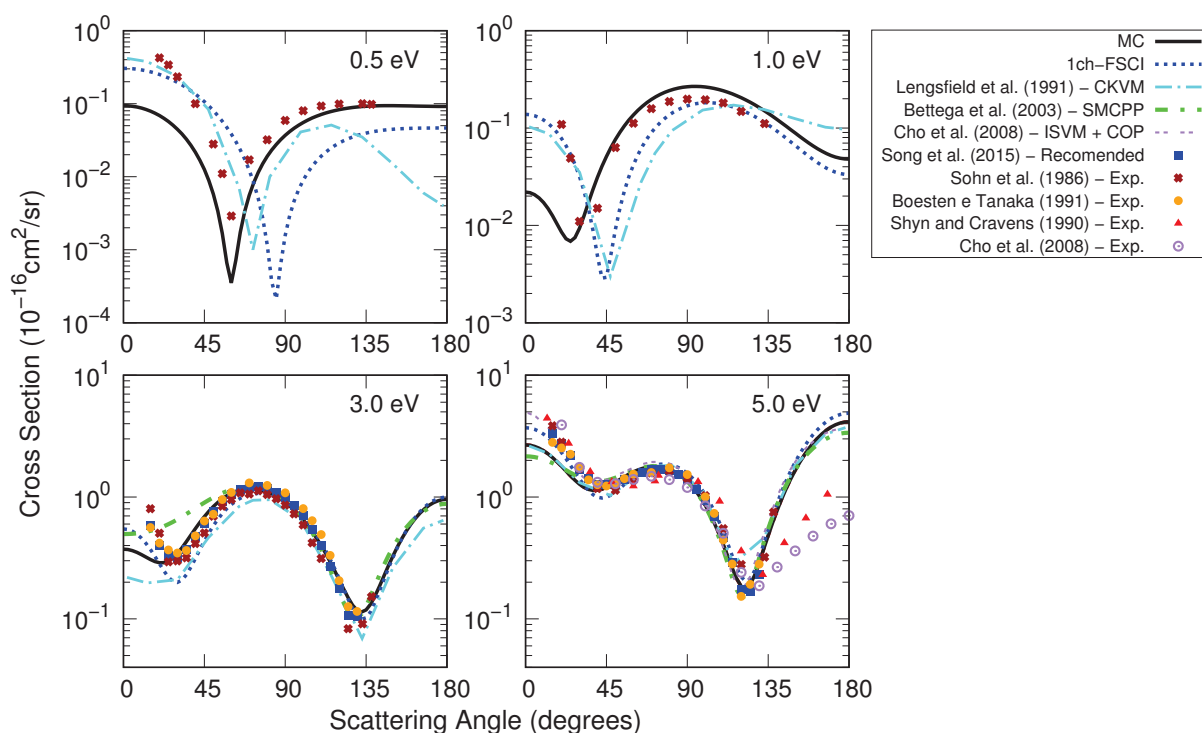


Figure 4.7 – Differential elastic cross sections for the electron scattering by methane at selected energies. The lines and points follow the same labels as in Fig. 4.4. Note that for energies below the first excitation threshold the cross sections obtained according to the 1ch and MC calculations coincide.

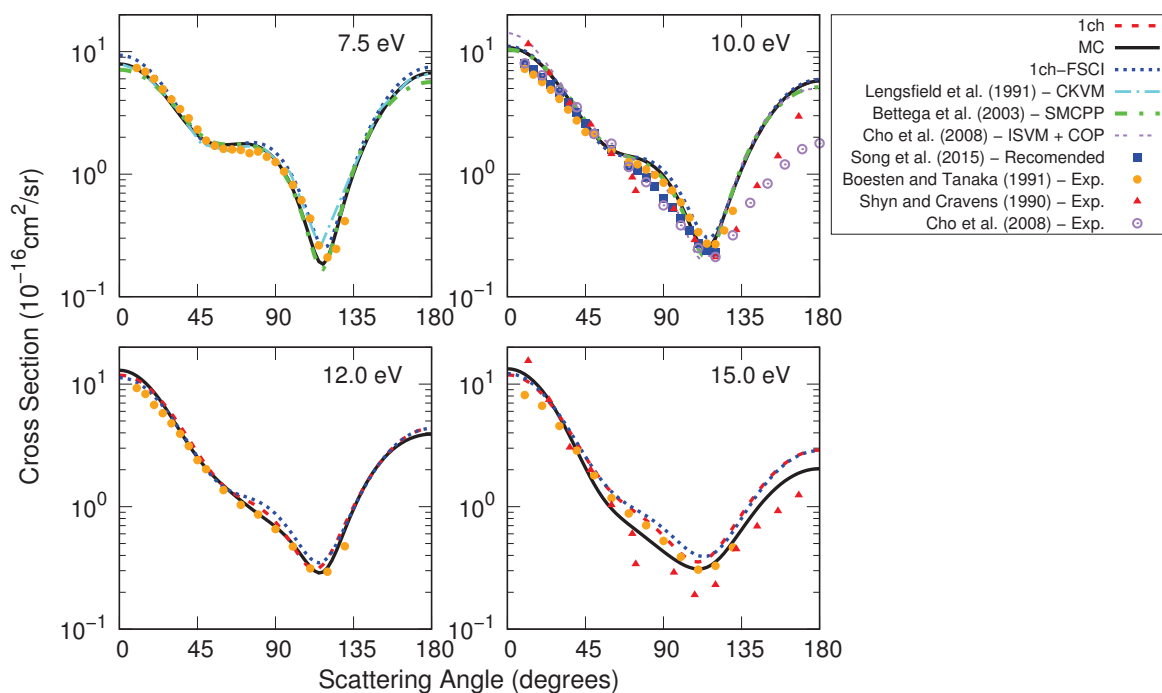


Figure 4.8 – Differential elastic cross sections for the electron scattering by methane at selected energies. The lines and points follow the same labels as in Fig. 4.4. Note that for energies below the first excitation threshold the cross sections obtained according to the 1ch and MC calculations coincide.

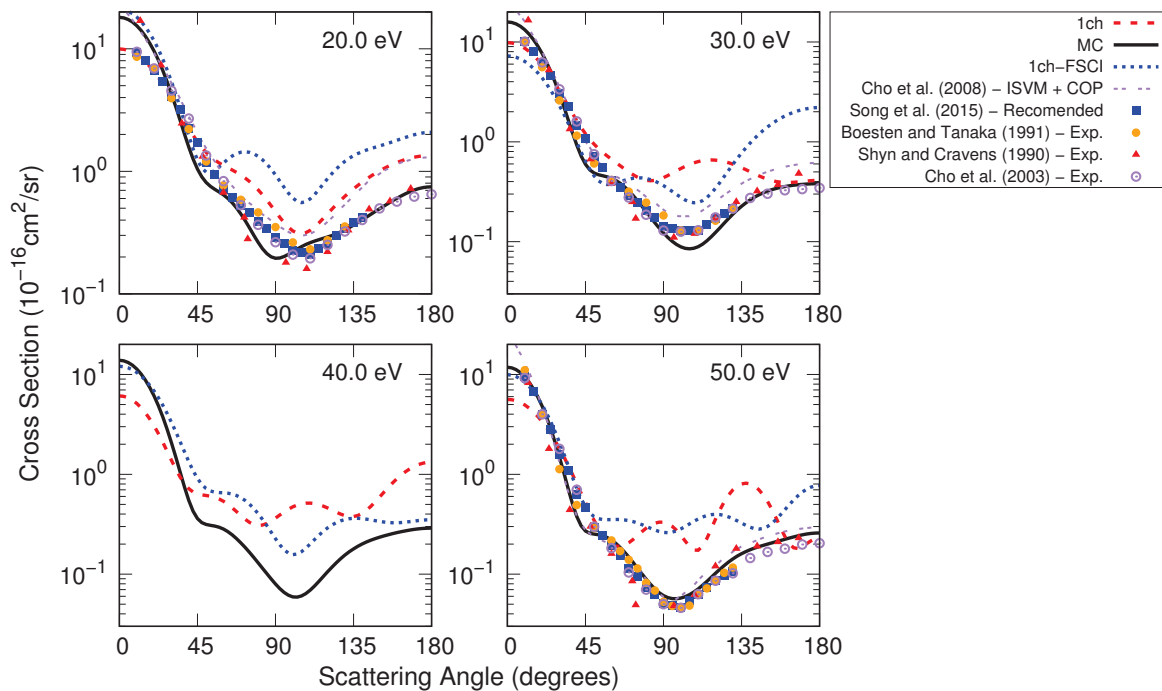


Figure 4.9 – Differential elastic cross sections for the electron scattering by methane at selected energies. The lines and points follow the same labels as in Fig. 4.4.

than the MC calculation when compared to the measured cross section [33, 58, 67–69]. At 15.0 eV a good agreement is also found, except for an overestimation of the experimental data from Shyn and Cravens [68]. At 12.0 and 15.0 eV the multichannel coupling effect is observed, but only small changes in the cross section are seen when one compares the 1ch and MC results. The competition for the flux that defines the cross section becomes more relevant as the incident electron energy increases, as can be seen by the large differences between these DCSs for impact energies in the 20.0 to 50.0 eV energy regime. In addition to lowering the magnitude of the cross sections, the introduction of the excitation processes in the scattering calculations corrects the ill oscillatory behaviour of the 1ch DCSs at higher impact energies associated with pseudoresonances in the corresponding ICS that vanish in the MC results. A good agreement is found between the MC DCSs and the results from the literature [33, 58, 68, 69] at these higher impact energies, indicating the importance of including the multichannel coupling for the description of the scattering at this energy regime. The only small deviation from the experimental data is at 20 eV, where the position of the minimum in the MC DCS is found to be at smaller angles than the observed experimentally. This is most likely due to a threshold effect at this impact energy associated with the opening of an electronically inelastic channel at 19.917 eV, as can be seen in Fig. 4.2. Nevertheless, the agreement with experimental data still is good [33, 58, 68, 69].

4.3 Electronically Inelastic Channels

The ICSs for the excitation of methane from the ground state to its first 9 electronically excited states calculated at the MC approximation are presented in Fig. 4.10. The 7-channel cross sections of Winstead *et al.* [71] (without the Born-closure procedure) and the 2-channel cross sections of Bettega *et al.* [73] calculated with the SMC and SMCPP methods, respectively, the cross section of Gil *et al.* [72] calculated with the complex Kohn method and the R-matrix results of Ziółkowski *et al.* [75] are also presented. In contrast to the excellent agreement with the available data from the literature in the elastic scattering channel, there are noticeable differences in the electronically inelastic cross sections. The low-magnitude of the electronic excitation cross sections leads to a high sensitivity of these cross sections to the computational details, which in turn leads to the dramatic differences seen in Fig. 4.10. Evidence that explicitly support this claim can be seen in the results calculated with different basis sets in the work of Ziółkowski *et al.* [75].

All the cross sections calculated by us presented in Fig. 4.10 follow a similar trend: below 20 eV the cross sections reaches its maximum value and displays numerous structures, while for impact energies above 20 eV the cross sections are smooth

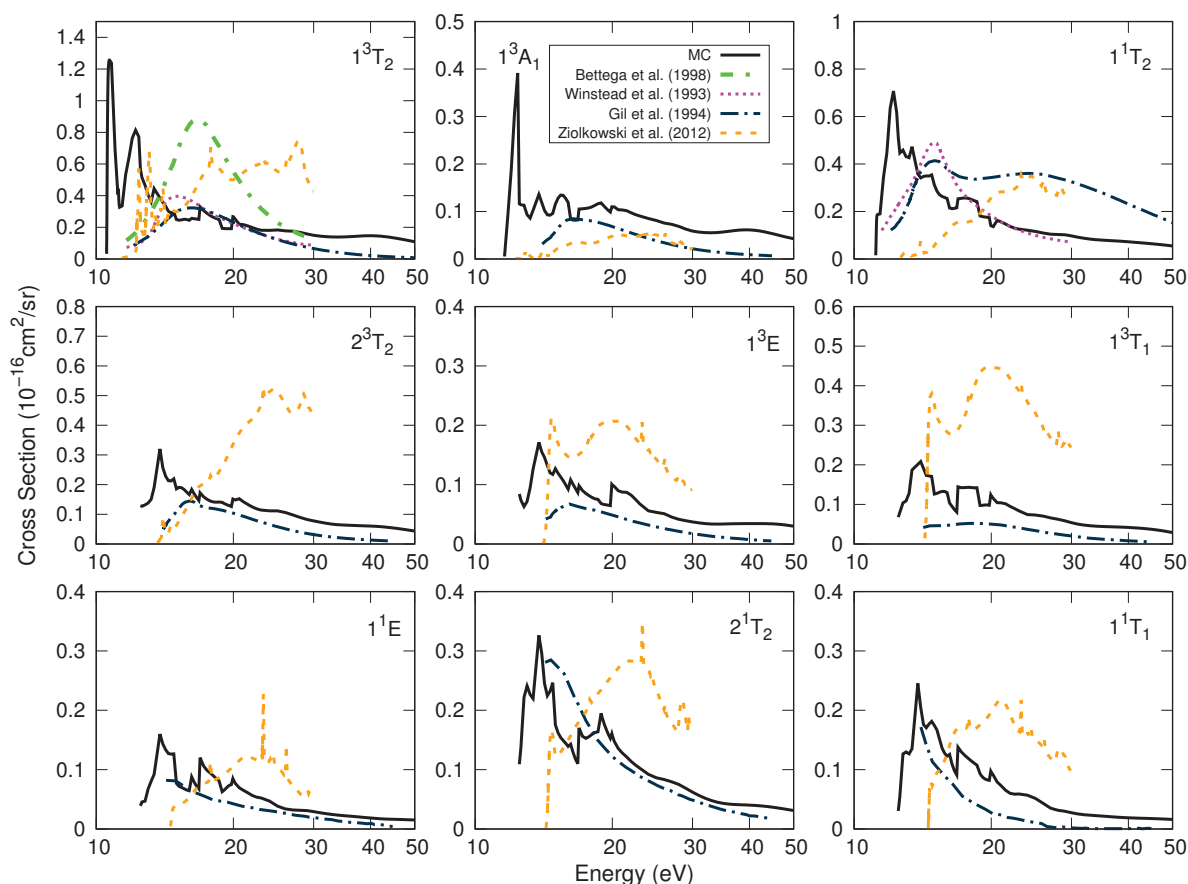


Figure 4.10 – Integral cross section for the 9 first electronically inelastic channels of methane. Full black line, present MC results; dotted magenta line, Winstead *et al.* (SMC) [71]; dash-dotted dark blue line, Gil *et al.* (CKVM) [72]; dash-dot-dotted green line, Bettega *et al.* (SMCPP) [73]; and dashed orange line, Ziolkowski *et al.* (R-Matrix) [75]. See text for a detailed discussion.

and structureless. The structures seen below 20 eV may be associated with resonances, pseudoresonances or threshold effects. Due to the small magnitude of the electronically inelastic cross sections, pseudoresonances and threshold effects appear more pronounced here when compared to the elastic cross section. Unfortunately, we are not able to distinguish between these and possible resonances in these cross sections. For energies above 20.549 eV, all energetically accessible channels are treated as open. Thus, due to the absence of closed-channels, the cross sections between 20 and 50 eV presents a smooth behaviour without structures.

Some interesting aspects of the theoretical treatment of the electronically inelastic scattering appear when a comparison with previous results from the literature is made (Fig. 4.10). First, let us compare our MC ICSs results to the 7-channel SMC calculation of Winstead *et al.* [71] and the 2-channel SMCPP results from Bettega *et al.* [73] for the 1^3T_2 and 1^1T_2 channels. We observe that all cross sections present the same qualitative behaviour, where the maximum is located below 20 eV and the cross section decreases

as the incident electron energy increases. For higher impact energies, the multichannel coupling effect dictates the behaviour of the cross section, leading to smaller values as more channels are treated as open. While our calculated cross section is overall smaller than the 2-channel calculation of Bettega *et al.* [73], as expected, surprisingly we found a good quantitative agreement with the 7-channel calculation of Winstead *et al.* [71] for energies above 20 eV. Since our calculations involve up to 181 open channels, it was expected that our cross sections would have a lower magnitude than the ones reported by the 7-channel calculation of Winstead *et al.* [71]. This seemingly puzzling comparison may be the result of a singular-value decomposition (SVD) technique used by Winstead *et al.* [71] to correct numerical instabilities that inversely artificially lowers the cross section's magnitude. Another interesting effect of dealing with a more complex multichannel coupling scheme is that structures appear below 20 eV, while the cross section calculated at 2-channel [73] and 7-channel [71] levels are smooth throughout all impact energies studied due to the absence of closed channels. The results reported by Gil *et al.* [72] were calculated using the complex Kohn method involving 54 electronically excited states of methane, albeit not all of them participate in the competition for the flux that defines the cross sections simultaneously due to the different multichannel coupling strategies adopted by the authors. Nevertheless, a good qualitative, and in some cases quantitative, agreement is found between our MC ICS and their cross sections [72]. The differences can be attributed to the sensitivity of the cross sections to the different methods and computational details used, such as the basis set and the description of the electronically excited states, and to the pseudoresonances that appear in our calculation. A poor agreement is found between the present MC ICSs and the ones reported by Ziłkowski *et al.* [75]. Although these authors observed some structures that may be related to the ones that appear in the MC ICSs, the qualitative behaviour differs greatly from our results and the other cross sections reported in the literature [71–73]. These comparisons have highlighted the daunting task of studying the electronic excitation of molecules through electron impact from a theoretical perspective, which continues to pose challenges to date.

In Fig. 4.11 and 4.12 we present the electronically inelastic DCSs for the excitation of methane from the ground state to the 1^3T_2 and 1^1T_2 electronically excited states at 12.5, 15.0, 20.0 and 30.0 eV, respectively. Although some oscillatory behaviour is seen in the 1^3T_2 excitation channel, such as the high magnitude of the DCS at 12.5 eV for higher scattering angles, the cross sections are mostly isotropic. In contrast, the DCSs for the 1^1T_2 excitation channel presents more pronounced oscillatory features at 15.0, 20.0 and 30.0 eV. The electronic excitation for the singlet state is optically allowed, thus long-ranged dipole interaction plays a role in the scattering process. However, as was the case for formamide in chapter 3, we did not perform the Born-closure procedure and, therefore, the electronically inelastic DCSs for the singlet state are expected to be

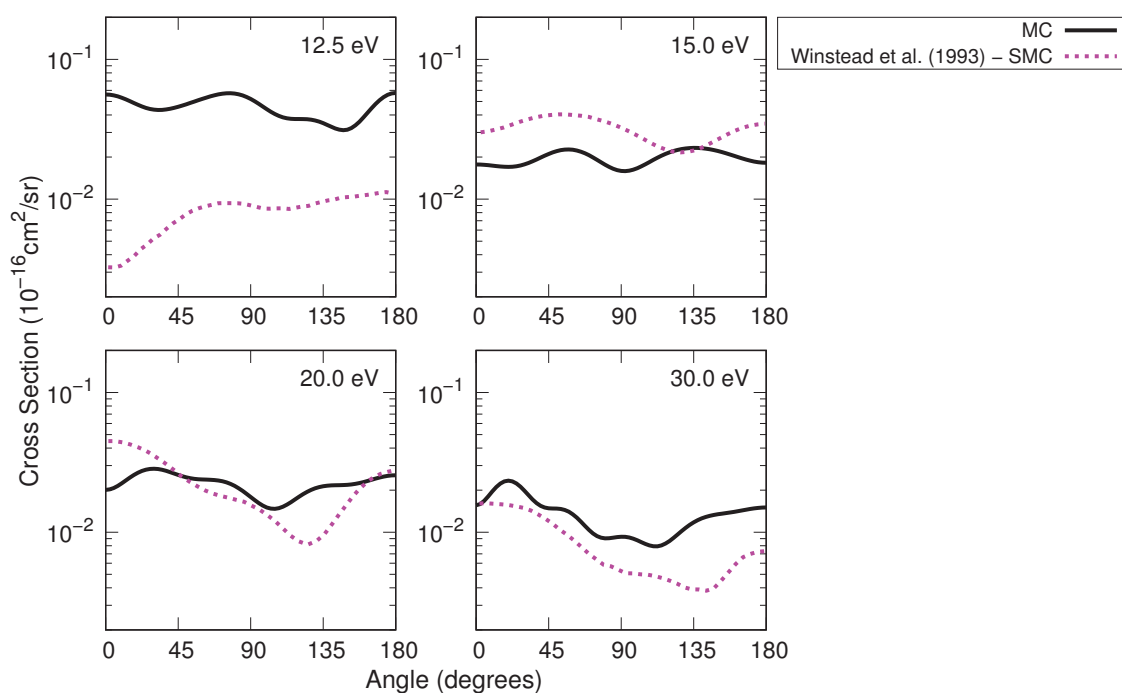


Figure 4.11 – Differential cross sections for the excitation of methane from the ground state to the 1^3T_2 electronically excited state at selected impact energies. Full black line, present MC results; and dotted magenta line, Winstead *et al.* (SMC) [71].

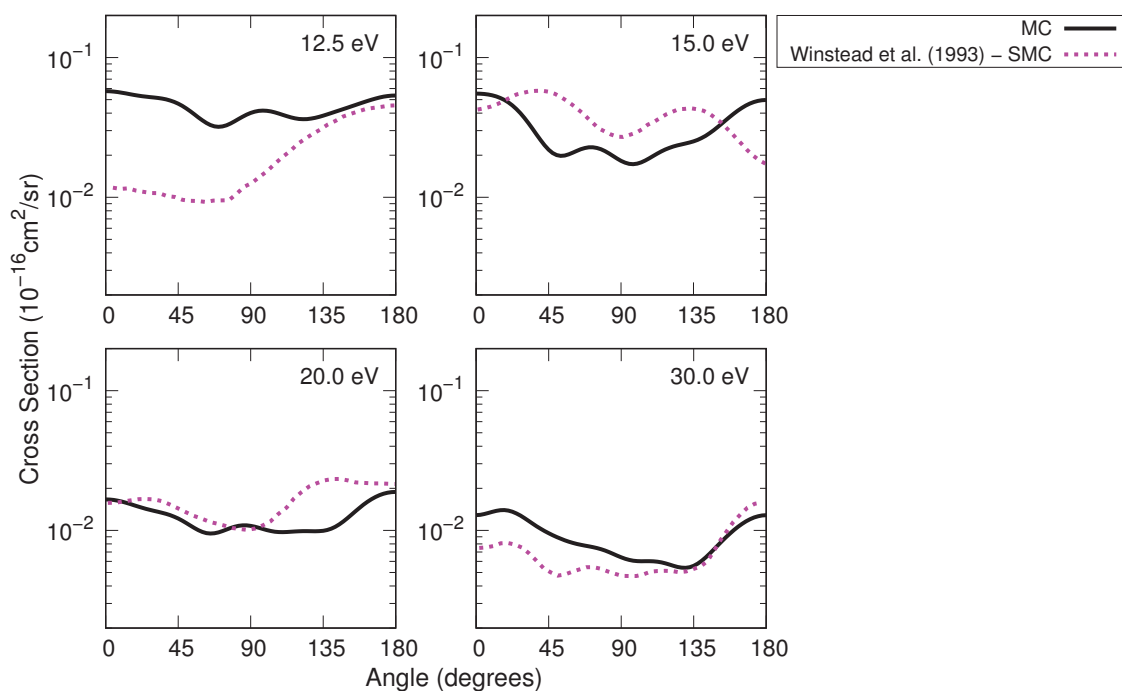


Figure 4.12 – Same as in Fig. 4.11, except that these are for the 1^1T_2 electronically excited state.

underestimated at the forward scattering angles. We also present in Figs. 4.11 and 4.12 the 7-channel results without Born-closure from Winstead *et al.* [71] for comparison. A surprisingly good quantitative agreement is found that once again may be related to the use of the SVD procedure by the authors [71].

To the best of our knowledge, only Vušković and Trajmar [70] have reported measurements of the electronically inelastic electron scattering cross sections for unresolved bands of methane. In Fig. 4.13 we compare the DCS computed by summing all electronically inelastic MC DCSs for channels whose threshold lie below 15 eV with the reported cross sections of Vušković and Trajmar [70] for energy losses between 7.5 and 15 eV. Our results overestimate the experimental measurements for most scattering angles, except for the forward scattering region. In this region, the long-range interactions, which are not well described by the SMC method, dominate the scattering process. Although our agreement with the experimental data is far from satisfactory, it is worth noting the normalization of the measured elastic DCSs conducted by Vušković and Trajmar [70] based on the early work of Tanaka *et al.* [121] discussed in the introduction of this section. These elastic DCSs were used to obtain the electronically inelastic DCSs, and thus, any error introduced by an improper normalization would carry over to the inelastic channels. Given the sensitivity of the electronic excitation cross sections, errors

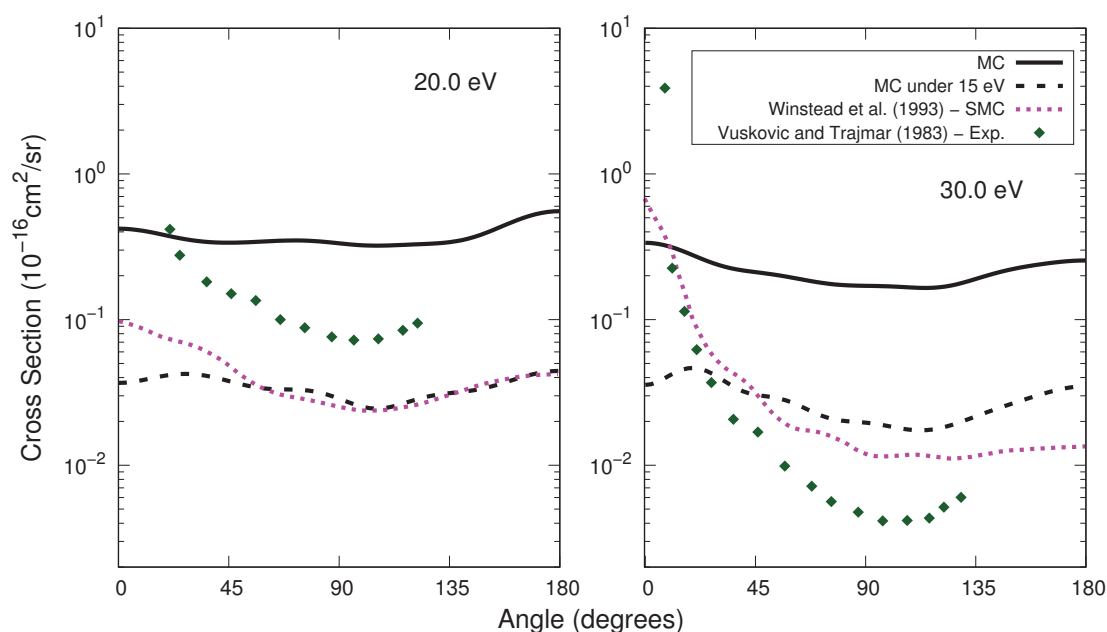


Figure 4.13 – Differential cross sections for the excitation of methane. Full black line, present MC results including all accessible electronically inelastic channels under 15 eV; dashed black line, MC with only the 1^3T_2 and 1^1T_2 electronic excitation cross sections; dotted magenta line, summed 1^3T_2 and 1^1T_2 excitation differential cross sections from Winstead *et al.* (SMC + Born-closure) [71]; dark-green diamonds, Vušković and Trajmar (Experimental) [70]. for energy losses of 7.5 to 15 eV.

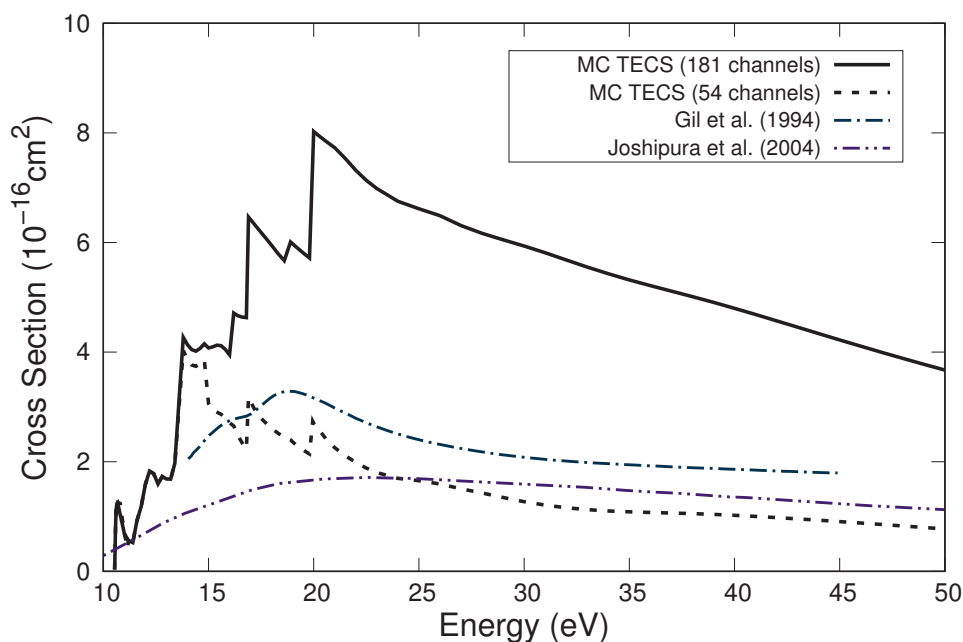


Figure 4.14 – Total excitation cross section of methane. Full black line, present MC results calculated with all 180 electronically inelastic cross sections; dashed black line, MC results considering only the first 54 electronically inelastic cross sections; dash-dotted dark blue line, Gil *et al.* (CKVM) [72]; and dash-dot-dotted indigo line, Joshipura *et al.* [74].

would be greatly amplified in the electronically inelastic channels. Hence, we take the disagreement between our current calculations and the measured data with a grain of salt. Additionally, the DCS computed as the sum of only the 1^3T_2 and 1^1T_2 excitation DCSs and the results from Winstead *et al.* [71], which were also obtained by the sum of these two electronically inelastic channels, are also presented in Fig. 4.13. Once again, the good agreement for higher energies was not expected, and is probably an effect of the SVD procedure used by the authors [71]. For low scattering angles, the lack of the Born-closure procedure in our calculations leads to the disagreement with the work of Winstead *et al.* [71].

In Fig. 4.14 we report the total excitation cross section (TECS) of methane alongside results from the literature [72, 74]. As is the case for the ICSs, the present TECS presents structures for impact energies below 20 eV that are attributed to pseudo-resonances and threshold effects, while for higher energies the cross section is smooth and free from structures. Our calculation overestimates the previous results from the literature [72, 74]. The discrepancy between our results and those from Gil *et al.* [72] can be explained by the number of inelastic channels considered in the TECS computation. Gil *et al.* [72] accounted for 54 electronically inelastic channels, whereas our TECS considers 180 inelastic channels. In order to investigate this point, we restrict the TECS computation to include only the first 54 electronically inelastic channels and

the result obtained with this procedure is shown as the dashed black line in Fig. 4.14. The difference between the present MC cross section and the one reported by Gil *et al.* [72] decreases, although in this case we underestimate their results. This latter underestimation is probably related to the higher competition for the flux that defines each individual cross section in our scattering calculations, which include 181 open channels, in comparison to the one from Gil *et al.* [72], performed with a total of 55 open channels. The higher competition for the flux results in smaller individual electronically inelastic cross sections, which leads to a smaller total excitation cross section. Note also that due to different channel coupling schemes used by Gil *et al.* [72] not all 55 channels are treated as open simultaneously. Additionally, it is worth mentioning that the TECS results presented by Joshipura *et al.* [74] are estimations rather than direct calculations, which leads to the disagreements found between our calculations and their results.

4.4 Total Ionization Cross Section

In Fig. 4.15 the TICS calculated with the BEB model is presented alongside representative results from the literature [57, 58, 122, 123]. The present calculations do not agree very well with the recommended cross sections [57, 58], which is expected. Due to the Jahn-Teller distortion on the cationic state of methane, the vertical and

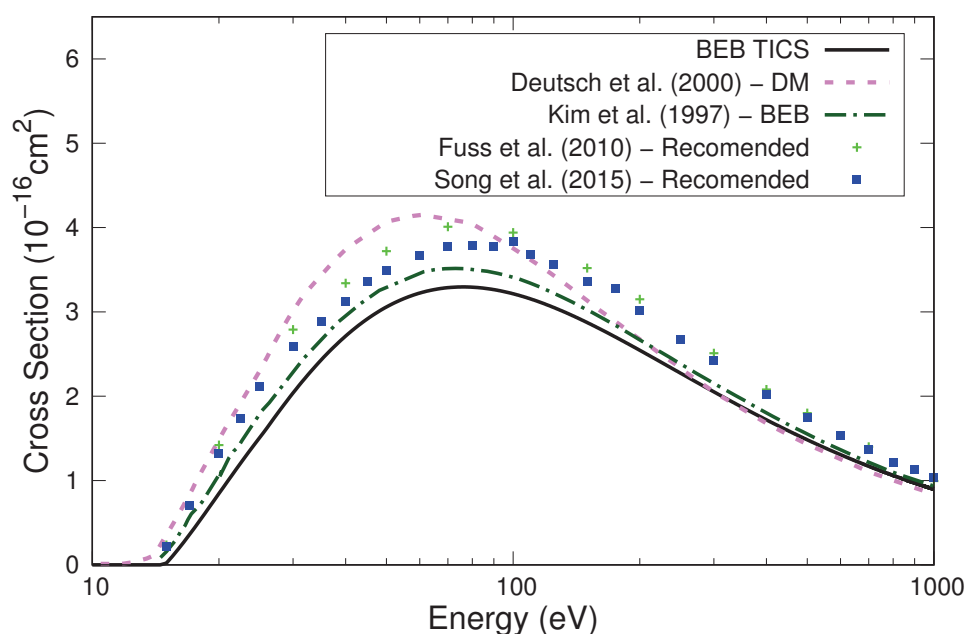


Figure 4.15 – Total ionization cross section for electron scattering by methane. Full black line, present BEB calculation; green crosses, Fuss *et al.* (recommended) [57]; blue squares, Song *et al.* (recommended) [58]; dash-dotted dark green line, Kim *et al.* (BEB) [122]; and dashed violet line, Deutsch *et al.* (DM) [123].

adiabatic ionization energies are quite different. Kim and coworkers [122] showed that cross sections calculated with the BEB model are sensitive to the choice of which kind of ionization energy is used, especially for molecules whose adiabatic and vertical ionization energies differ by 1 eV or more. Thus, we did not expect to obtain an excellent agreement with the recommended data [57, 58].

4.5 Total Cross Section

In Fig. 4.16 we present the total cross section (TCS) for the scattering of electrons by methane. The present results are obtained by summing the elastic MC ICS (Fig. 4.4), the TECS (Fig. 4.10) and the TICS obtained with the present BEB calculation (Fig. 4.15). The TCS depicts the same qualitative behaviour as the elastic ICS, that is, it shows the RT minimum and the shape resonance for low-impact energies, pseudoresonances and threshold effects for the intermediate impact energy regime and a smooth behaviour for energies above the last excitation threshold (20.549 eV). When comparing the present results to the recommended cross sections of Fuss *et al.* [57] and Song *et al.* [58] we find a relatively good agreement. However, our calculations tend to overestimate the recommended cross sections at higher impact energies. This discrepancy could potentially be attributed to the absence of the ionization channel in the SMC method, since it would compete for the flux that defines the elastic and electronic

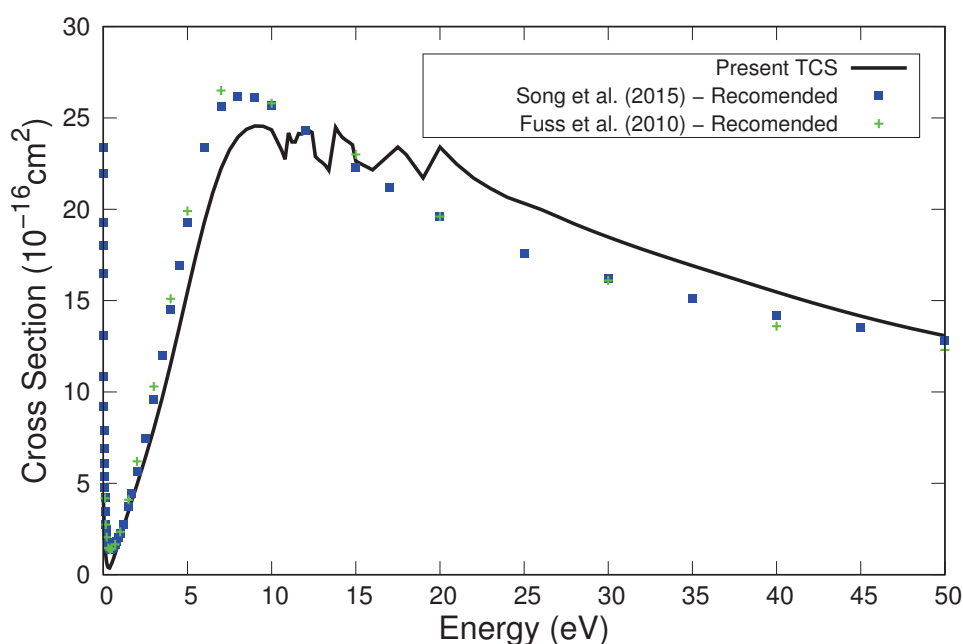


Figure 4.16 – Total cross section for electron scattering by methane. Full black line, present results; green crosses, recommended data from Fuss *et al.* [57]; and blue squares, recommended data from Song *et al.* [58].

excitation cross section lowering their magnitudes. Furthermore, if the ionization channel were included in the SMC calculations, the elastic and electronically inelastic channels would compete for the flux that defines the ionization cross section itself, lowering the magnitude of the total ionization cross section as well.

4.6 Conclusion

In this chapter, the elastic and electronically inelastic electron scattering cross sections by methane were presented. These cross sections were obtained through the SMCPP method within the MOB-SCI approach with up to 181 open channels. When multichannel coupling effects are considered, the elastic cross sections agree well with previous results from the literature [33, 57, 58, 61, 62, 64–70, 75], both in the low- and high-energy regimes. This agreement indicates that the polarization effects and the multichannel coupling effect are well described by our scattering calculations. Another evidence that supports this claim is the well characterized RT minimum observed in our results. On the other hand, as is the case for formamide, the comparison between our electronically inelastic ICSs and the ones reported in the literature [71–73, 75] is far from satisfactory. This is due to the large amount of pseudoresonances and threshold effects that appear in our results and the sensitivity of the electronically inelastic scattering cross sections to these structures. Additionally, the TICS and TCS for the electron scattering by methane were also presented.

CHAPTER 5

Conclusion

The scattering of low energy electrons by formamide and methane was studied. The Schwinger Multichannel method implemented with *norm-conserving* pseudopotentials (SMCPP) was used with the minimal orbital basis for single-configuration interaction (MOB-SCI) approach to calculate the elastic and electronically inelastic electron scattering cross sections, while the Binary-Encounter-Bethe (BEB) model was employed to obtain the total ionization cross section (TICS). From these, the total cross sections (TCS) for the electron scattering by formamide and methane were estimated.

The elastic and electronically inelastic ICSs and DCSs for the scattering of electrons by formamide were calculated with the SMCPP method within the MOB-SCI approach with up to 179 open channels. The multichannel coupling effect was observed in all cross sections. The comparison between the elastic DCSs and the ones found in the literature is far from satisfactory [43, 45–47], but these differences are averaged out when looking at the elastic ICS [39, 42, 43, 45, 47, 49]. The DCSs and ICSs for the excitation from the ground state to the first four low-lying electronically excited states of formamide were also reported. The comparison with results from the literature [43, 46] is poor due to pseudoresonances and threshold effects that are present in the current ICSs. The TICS and TCS tend to agree well with results from the literature [44, 45]. Unfortunately, the lack of experimental data hampers our ability to scrutinize these differences.

As was done for formamide, the elastic and electronically inelastic ICSs and DCSs for methane were calculated with the SMCPP method within the MOB-SCI approach. An additional calculation using all molecular orbitals to construct the basis set

for the scattering calculations was also performed. This additional calculation showed that the polarization effects are being well described by the MOB-SCI approach. The elastic ICS and DCSs agree really well throughout all impact energies with previous results from the literature [33, 57, 58, 61, 62, 64–70, 75] when the multichannel coupling effect is included in the scattering calculations. Once again, the comparison between the available results results for the electronically inelastic channels is far from satisfactory [70–73, 75]. Due to the Jahn-Teller distortion of the cationic state of methane our TICS do not agree very well with the recommended data [57, 58]. Nevertheless, the TCS presents an overall good agreement with the literature [57, 58].

The present dissertation sheds light on a contrasting picture regarding the theoretical treatment of electron scattering cross sections by molecules. On one hand, electron scattering phenomena observed in the elastic channel can be well characterized, such as is the case of shape resonances and the Ramsauer-Townsend minimum. Additionally, most often than not, the elastic cross sections tend to agree well with results from the literature. On the other hand, the agreement between the electronically inelastic cross sections remains unsatisfactory. The sensitivity of these cross sections to pseudoresonances and threshold effects hampers our ability to characterize core-excited and Feshbach resonances. Additionally, the lack of experimental data for the molecules studied poses a significant obstacle to further theoretical development. To bridge the gap between these two worlds and fully grasp the nature of these intricate processes, further theoretical and experimental investigations focusing on the electron-impact electronic excitation of molecules are needed.

BIBLIOGRAPHY

- 1 MASON, N. J. Future studies on electron scattering; a renaissance. **Journal of Physics: Conference Series**, v. 565, n. 1, p. 012001, 2014. Cit. on p. 22.
- 2 SANZ, A. G.; FUSS, M. C.; MUÑOZ, A.; BLANCO, F.; LIMÃO-VIEIRA, P.; BRUNGER, M. J.; BUCKMAN, S. J.; GARCIA, G. Modelling low energy electron and positron tracks for biomedical applications. **International Journal of Radiation Biology**, Taylor & Francis, v. 88, n. 1-2, p. 71–76, 2012. Cit. on pp. 22, 25.
- 3 WICIAK-PAWŁOWSKA, K.; WINIARSKA, A.; TAIOLI, S.; DAPOR, M.; FRANZ, M.; FRANZ, J. The Role of Molecular Structure in Monte Carlo Simulations of the Secondary Electron Yield and Backscattering Coefficient from Methacrylic Acid. **Molecules**, MDPI, v. 28, n. 3, p. 1126, 2023. Cit. on p. 22.
- 4 HITCHON, W. N. G. **Plasma processes for semiconductor fabrication**. Cambridge: Cambridge University Press, 1999. Cit. on p. 22.
- 5 LIEBERMAN, M. A.; LICHTENBERG, A. J. **Principles of plasma discharges and materials processing**. Hoboken, New Jersey: John Wiley & Sons, Inc., 2005. Cit. on p. 22.
- 6 HUTH, M.; PORRATI, F.; DOBROVOLSKIY, O. V. Focused electron beam induced deposition meets materials science. **Microelectronic Engineering**, Elsevier, v. 185, p. 9–28, 2018. Cit. on p. 22.
- 7 THORMAN, R. M.; RAGESH KUMAR, T. P.; FAIRBROTHER, D. H.; INGÓLF-

- SSON, O. The role of low-energy electrons in focused electron beam induced deposition: four case studies of representative precursors. **Beilstein Journal of Nanotechnology**, Beilstein-Institut, v. 6, n. 1, p. 1904–1926, 2015. Cit. on p. 23.
- 8 BOYER, M. C.; RIVAS, N.; TRAN, A. A.; VERISH, C. A.; ARUMAINAYAGAM, C. R. The role of low-energy (≤ 20 eV) electrons in astrochemistry. **Surface Science**, Elsevier, v. 652, p. 26–32, 2016. Cit. on p. 23.
- 9 PILLING, S.; ANDRADE, D. P.; NETO, A. C.; RITTNER, R.; NAVES DE BRITO, A. DNA nucleobase synthesis at Titan atmosphere analog by soft X-rays. **The Journal of Physical Chemistry A**, ACS Publications, v. 113, n. 42, p. 11161–11166, 2009. Cit. on p. 23.
- 10 SHULENBERGER, K. E.; ZHU, J. L.; TRAN, K.; ABDULLAHI, S.; BELVIN, C.; LUKENS, J.; PEELER, Z.; MULLIKIN, E.; CUMBERBATCH, H. M.; HUANG, J., et al. Electron-induced radiolysis of astrochemically relevant ammonia ices. **ACS Earth and Space Chemistry**, ACS Publications, v. 3, n. 5, p. 800–810, 2019. Cit. on pp. 23, 24.
- 11 JEILANI, Y. A.; NGUYEN, H. T.; NEWALLO, D.; DIMANDJA, J.-M. D.; NGUYEN, M. T. Free radical routes for prebiotic formation of DNA nucleobases from formamide. **Physical Chemistry Chemical Physics**, Royal Society of Chemistry, v. 15, n. 48, p. 21084–21093, 2013. Cit. on pp. 23, 28, 60.
- 12 ALBERTS, B.; JOHNSON, A.; LEWIS, J.; MORGAN, D.; RAFF, M.; ROBERTS, K.; WALTER, P.; WILSON, J.; HUNT, T. **Biologia Molecular da Célula**. Porto Alegre, Rio Grande do Sul: Artmed Editora, 2017. Cit. on p. 24.
- 13 BOUDAÏFFA, B.; CLOUTIER, P.; HUNTING, D.; HUELS, M. A.; SANCHE, L. Resonant formation of DNA strand breaks by low-energy (3 to 20 eV) electrons. **Science**, American Association for the Advancement of Science, v. 287, n. 5458, p. 1658–1660, 2000. Cit. on pp. 24–26.
- 14 BACCARELLI, I.; BALD, I.; GIANTURCO, F. A.; ILLENBERGER, E.; KOPYRA, J. Electron-induced damage of DNA and its components: Experiments and theoretical models. **Physics Reports**, Elsevier, v. 508, n. 1-2, p. 1–44, 2011. Cit. on p. 25.
- 15 MEISSNER, R.; KOČIŠEK, J.; FEKETEOVÁ, L.; FEDOR, J.; FÁRNÍK, M.; LIMÃO-

- VIEIRA, P.; ILLENBERGER, E.; DENIFL, S. Low-energy electrons transform the nimorazole molecule into a radiosensitizer. **Nature Communications**, Nature Publishing Group UK London, v. 10, n. 1, p. 2388, 2019. Cit. on p. 25.
- 16 WANG, H.; MU, X.; HE, H.; ZHANG, X.-D. Cancer radiosensitizers. **Trends in pharmacological sciences**, Elsevier, v. 39, n. 1, p. 24–48, 2018. Cit. on p. 25.
- 17 SAQIB, M.; IZADI, F.; ISIERHIENRHIEN, L. U.; ONČÁK, M.; DENIFL, S. Decomposition of triazole and 3-nitrotriazole upon low-energy electron attachment. **Physical Chemistry Chemical Physics**, Royal Society of Chemistry, v. 25, n. 20, p. 13892–13901, 2023. Cit. on p. 25.
- 18 SCHULZ, G. J. Resonances in electron impact on diatomic molecules. **Reviews of Modern Physics**, APS, v. 45, n. 3, p. 423, 1973. Cit. on p. 25.
- 19 LOZANO, A. I.; KOSSOSKI, F.; BLANCO, F.; LIMÃO-VIEIRA, P.; VARELLA, M. T. d. N.; GARCÍA, G. Observation of Transient Anions That Do Not Decay through Dissociative Electron Attachment: New Pathways for Radiosensitization. **The Journal of Physical Chemistry Letters**, ACS Publications, v. 13, n. 30, p. 7001–7008, 2022. Cit. on pp. 26, 27, 54.
- 20 SANCHE, L. Beyond radical thinking. **Nature**, Nature Publishing Group UK London, v. 461, n. 7262, p. 358–359, 2009. Cit. on p. 26.
- 21 GALLUP, G. A.; BURROW, P. D.; FABRIKANT, I. I. Electron-induced bond breaking at low energies in HCOOH and glycine: The role of very short-lived σ^* anion states. **Physical Review A**, APS, v. 79, n. 4, p. 042701, 2009. Cit. on p. 27.
- 22 RESCIGNO, T. N.; TREVISAN, C. S.; OREL, A. E. Dynamics of low-energy electron attachment to formic acid. **Physical Review Letters**, APS, v. 96, n. 21, p. 213201, 2006. Cit. on p. 27.
- 23 RESCIGNO, T.; TREVISAN, C.; OREL, A. Comment on “electron-induced bond breaking at low energies in HCOOH and glycine: The role of very short-lived σ^* anion states”. **Physical Review A**, APS, v. 80, n. 4, p. 046701, 2009. Cit. on p. 27.
- 24 GALLUP, G. A.; BURROW, P. D.; FABRIKANT, I. I. Reply to “Comment on ‘Electron-induced bond breaking at low energies in HCOOH and glycine: The role of very short-lived σ^* anion states’”. **Physical Review A**, APS, v. 80, n. 4,

- p. 046702, 2009. Cit. on p. 27.
- 25 BARRIOS, R.; SKURSKI, P.; SIMONS, J. Mechanism for damage to DNA by low-energy electrons. **The Journal of Physical Chemistry B**, ACS Publications, v. 106, n. 33, p. 7991–7994, 2002. Cit. on p. 27.
- 26 SIMONS, J. How do low-energy (0.1– 2 eV) electrons cause DNA-strand breaks? **Accounts of Chemical Research**, ACS Publications, v. 39, n. 10, p. 772–779, 2006. Cit. on p. 27.
- 27 LUO, X.; ZHENG, Y.; SANCHE, L. DNA strand breaks and crosslinks induced by transient anions in the range 2-20 eV. **The Journal of Chemical Physics**, AIP Publishing, v. 140, n. 15, 2014. Cit. on p. 27.
- 28 DAVIS, D.; KUNDU, S.; PRABHUDESAI, V. S.; SAJEEV, Y.; KRISHNAKUMAR, E. Formation of CO₂ from formic acid through catalytic electron channel. **The Journal of Chemical Physics**, AIP Publishing, v. 149, n. 6, 2018. Cit. on p. 27.
- 29 LOUPAS, A.; REGETA, K.; ALLAN, M.; GORFINKIEL, J. D. Shape and core-excited resonances in thiophene. **The Journal of Physical Chemistry A**, ACS Publications, v. 122, n. 4, p. 1146–1155, 2018. Cit. on p. 27.
- 30 RESCIGNO, T.; OREL, A. Theoretical study of excitation of the low-lying electronic states of water by electron impact. **Physical Review A**, APS, v. 88, n. 1, p. 012703, 2013. Cit. on p. 27.
- 31 TAKATSUKA, K.; MCKOY, V. Extension of the Schwinger variational principle beyond the static-exchange approximation. **Physical Review A**, APS, v. 24, n. 5, p. 2473, 1981. Cit. on pp. 27, 34, 39.
- 32 TAKATSUKA, K.; MCKOY, V. Theory of electronically inelastic scattering of electrons by molecules. **Physical Review A**, APS, v. 30, n. 4, p. 1734, 1984. Cit. on pp. 27, 34.
- 33 CHO, H.; PARK, Y.; CASTRO, E. y; DE SOUZA, G.; IGA, I.; MACHADO, L.; BRESCANSIN, L.; LEE, M. A comparative experimental–theoretical study on elastic electron scattering by methane. **Journal of Physics B: Atomic, Molecular and Optical Physics**, IOP Publishing, v. 41, n. 4, p. 045203, 2008. Cit. on pp. 27, 29, 79, 87, 88, 90, 92, 100, 102.

- 34 BLANCO, F.; ELLIS-GIBBINGS, L.; GARCÍA, G. Screening corrections for the interference contributions to the electron and positron scattering cross sections from polyatomic molecules. **Chemical Physics Letters**, Elsevier, v. 645, p. 71–75, 2016. Cit. on p. 27.
- 35 BODE, B. M.; GORDON, M. S. MacMolPlt: a graphical user interface for GAMESS. **Journal of Molecular Graphics and Modelling**, Elsevier, v. 16, n. 3, p. 133–138, 1998. Cit. on pp. 28, 29, 59, 78, 123.
- 36 CLOUTIER, P.; SICARD-ROSELLI, C.; ESCHER, E.; SANCHE, L. Low-Energy (3–24 eV) Electron Damage to the Peptide Backbone. **The Journal of Physical Chemistry B**, ACS Publications, v. 111, n. 7, p. 1620–1624, 2007. Cit. on pp. 28, 59.
- 37 RUBIN, R.; SWENSON JR, G.; BENSON, R.; TIGELAAR, H.; FLYGARE, W. Microwave detection of interstellar formamide. **The Astrophysical Journal**, v. 169, p. 139, 1971. Cit. on pp. 28, 60.
- 38 HOLLIS, J.; LOVAS, F. J.; REMIJAN, A. J.; JEWELL, P.; ILYUSHIN, V. V.; KLEINER, I. Detection of acetamide (CH_3CONH_2): The largest interstellar molecule with a peptide bond. **The Astrophysical Journal**, IOP Publishing, v. 643, n. 1, p. 125, 2006. Cit. on pp. 28, 60.
- 39 SEYDOU, M.; MODELLI, A.; LUCAS, B.; KONATE, K.; DESFRANÇOIS, C.; SCHERMANN, J. Electron attachment to strongly polar clusters: Formamide molecule and clusters. **The European Physical Journal D-Atomic, Molecular, Optical and Plasma Physics**, Springer, v. 35, p. 199–205, 2005. Cit. on pp. 28, 60, 69–71, 101.
- 40 HAMANN, T.; EDTBAUER, A.; DA SILVA, F. F.; DENIFL, S.; SCHEIER, P.; SWIDEREK, P. Dissociative electron attachment to gas-phase formamide. **Physical Chemistry Chemical Physics**, Royal Society of Chemistry, v. 13, n. 26, p. 12305–12313, 2011. Cit. on pp. 28, 60, 69, 71.
- 41 LI, Z.; RYSZKA, M.; DAWLEY, M. M.; CARMICHAEL, I.; BRAVAYA, K. B.; PTASIŃSKA, S. Dipole-supported electronic resonances mediate electron-induced amide bond cleavage. **Physical Review Letters**, APS, v. 122, n. 7, p. 073002, 2019. Cit. on pp. 28, 60.

- 42 BETTEGA, M. H. Collisions of low-energy electrons with formamide. **Physical Review A**, APS, v. 81, n. 6, p. 062717, 2010. Cit. on pp. 28, 60, 61, 64, 69–71, 101, 125.
- 43 WANG, Y.-F.; TIAN, S. X. Low-energy electron collisions with formamide using the R-matrix method. **Physical Review A**, APS, v. 85, n. 1, p. 012706, 2012. Cit. on pp. 28, 60, 62, 63, 66–71, 73–75, 77, 101.
- 44 GUPTA, D.; NAGHMA, R.; ANTONY, B. Electron impact total ionisation cross sections for simple bio-molecules: a theoretical approach. **Molecular Physics**, Taylor & Francis, v. 112, n. 8, p. 1201–1209, 2014. Cit. on pp. 28, 60, 75, 76, 101.
- 45 HOMEM, M.; IGA, I.; SOUZA, G. de; ZANELATO, A.; MACHADO, L.; FERRAZ, J.; SANTOS, A. dos; BRESCANSIN, L.; LUCCHESI, R.; LEE, M.-T. Electron collisions with ammonia and formamide in the low-and intermediate-energy ranges. **Physical Review A**, APS, v. 90, n. 6, p. 062704, 2014. Cit. on pp. 28, 60, 66–71, 75–77, 101.
- 46 VINODKUMAR, M.; LIMBACHIYA, C.; DESAI, H.; VINODKUMAR, P. Electron impact rotationally elastic total cross section for formamide. **Journal of Applied Physics**, AIP Publishing LLC, v. 116, n. 12, p. 124702, 2014. Cit. on pp. 28, 60, 62, 63, 66–71, 73–77, 101.
- 47 SILVA, M. O.; MOREIRA, G. M.; BETTEGA, M. H.; SANCHEZ, S. d. Electron and Positron Scattering by the Formamide Molecule. **The Journal of Physical Chemistry A**, ACS Publications, v. 124, n. 29, p. 6009–6015, 2020. Cit. on pp. 28, 60, 61, 64, 66–71, 77, 101.
- 48 SILVA, M. O.; MOREIRA, G. M.; BETTEGA, M. H.; SANCHEZ, S. d. Effect of single and double methylation on the position of the π^* shape resonance of formamide and acetamide. **Chemical Physics**, Elsevier, v. 555, p. 111432, 2022. Cit. on pp. 28, 60, 61, 69, 71.
- 49 GOUMANS, T.; GIANTURCO, F.; SEBASTIANELLI, F.; BACCARELLI, I.; RIVAIL, J. Dissociative electron attachment to formamide: Direct and indirect pathways from resonant intermediates. **Journal of Chemical Theory and Computation**, ACS Publications, v. 5, n. 1, p. 217–221, 2009. Cit. on pp. 28, 61, 69–71, 101.
- 50 GALLUP, G. Stable negative ions and shape resonances in a series of organic

- molecules. **The Journal of Chemical Physics**, American Institute of Physics, v. 139, n. 10, p. 104308, 2013. Cit. on pp. 28, 61, 69, 71, 75.
- 51 RANDI, P.; MOREIRA, G.; BETTEGA, M. Electron scattering by formamide: Elastic and electronically inelastic cross sections up to 179 energetically open states. **Physical Review A**, APS, v. 107, n. 1, p. 012806, 2023. Cit. on pp. 28, 47, 54, 59.
- 52 FRANCESCHINI, D.; FREIRE JR, F.; ACHETE, C.; MARIOTTO, G. Hard amorphous hydrogenated carbon-nitrogen films obtained by PECVD in methane-ammonia atmospheres. **Diamond and related materials**, Elsevier, v. 5, n. 3-5, p. 471–474, 1996. Cit. on pp. 28, 78.
- 53 MOTTA, E.; PEREYRA, I. Amorphous hydrogenated carbon-nitride films prepared by RF-PECVD in methane–nitrogen atmospheres. **Journal of Non-Crystalline Solids**, Elsevier, v. 338, p. 525–529, 2004. Cit. on pp. 28, 78.
- 54 MOUSIS, O.; CHASSEFIERE, E.; HOLM, N. G.; BOUQUET, A.; WAITE, J. H.; GEPPERT, W. D.; PICAUD, S.; AIKAWA, Y.; ALI-DIB, M.; CHARLOU, J.-L., et al. Methane clathrates in the solar system. **Astrobiology**, Mary Ann Liebert, Inc. 140 Huguenot Street, 3rd Floor New Rochelle, NY 10801 USA, v. 15, n. 4, p. 308–326, 2015. Cit. on pp. 28, 78.
- 55 QASIM, D.; FEDOSEEV, G.; CHUANG, K.-J.; HE, J.; IOPPOLO, S.; DISHOECK, E. van; LINNARTZ, H. An experimental study of the surface formation of methane in interstellar molecular clouds. **Nature Astronomy**, Nature Publishing Group UK London, v. 4, n. 8, p. 781–785, 2020. Cit. on pp. 28, 78.
- 56 HOUGHTON, J. Global warming. **Reports on Progress in Physics**, IOP Publishing, v. 68, n. 6, p. 1343, 2005. Cit. on pp. 28, 79.
- 57 FUSS, M.; MUÑOZ, A.; OLLER, J.; BLANCO, F.; HUBIN-FRANSKIN, M.-J.; ALMEIDA, D.; LIMÃO-VIEIRA, P.; GARCÍA, G. Electron–methane interaction model for the energy range 0.1–10 000 eV. **Chemical Physics Letters**, Elsevier, v. 486, n. 4-6, p. 110–115, 2010. Cit. on pp. 29, 79, 80, 87–89, 98–100, 102.
- 58 SONG, M.-Y.; YOON, J.-S.; CHO, H.; ITIKAWA, Y.; KARWASZ, G. P.; KOKOOLINE, V.; NAKAMURA, Y.; TENNYSON, J. Cross sections for electron collisions with methane. **Journal of Physical and Chemical Reference Data**, AIP Publishing, v. 44, n. 2, 2015. Cit. on pp. 29, 79, 80, 87–90, 92, 98–100, 102.

- 59 GADOUM, A.; BENYOUCEF, D. Set of the electron collision cross sections for methane molecule. **IEEE Transactions on Plasma Science**, IEEE, v. 47, n. 3, p. 1505–1513, 2018. Cit. on pp. 29, 79, 80.
- 60 GIANTURCO, F.; THOMPSON, D. The Ramsauer-Townsend effect in methane. **Journal of Physics B: Atomic and Molecular Physics**, IOP Publishing, v. 9, n. 12, p. 1383, 1976. Cit. on pp. 29, 79.
- 61 LENGFIELD III, B.; RESCIGNO, T.; MCCURDY, C. Ab initio study of low-energy electron-methane scattering. **Physical Review A**, APS, v. 44, n. 7, p. 4296, 1991. Cit. on pp. 29, 79, 87–90, 100, 102.
- 62 NESTMANN, B. M.; PFINGST, K.; PEYERIMHOFF, S. D. R-matrix calculation for electron-methane scattering cross sections. **Journal of Physics B: Atomic, Molecular and Optical Physics**, IOP Publishing, v. 27, n. 11, p. 2297, 1994. Cit. on pp. 29, 55, 79, 87–89, 100, 102.
- 63 GIANTURCO, F.; RODRIGUES-RUIZ, J.; SANNA, N. The Ramsauer minimum of methane. **Journal of Physics B: Atomic, Molecular and Optical Physics**, IOP Publishing, v. 28, n. 7, p. 1287, 1995. Cit. on pp. 29, 79.
- 64 ALTHORPE, S.; GIANTURCO, F.; SANNA, N. Calculation of integral cross sections for vibrationally inelastic electron-methane scattering. **Journal of Physics B: Atomic, Molecular and Optical Physics**, IOP Publishing, v. 28, n. 18, p. 4165, 1995. Cit. on pp. 29, 79, 87–89, 100, 102.
- 65 BETTEGA, M. H. F.; VARELLA, M. d. N.; LIMA, M. A. P. Polarization effects in the elastic scattering of low-energy electrons by XH_4 ($X = C, Si, Ge, Sn, Pb$). **Physical Review A**, APS, v. 68, n. 1, p. 012706, 2003. Cit. on pp. 29, 79, 80, 87, 88, 90, 100, 102.
- 66 VINODKUMAR, M.; LIMBACHIYA, C.; JOSHIPURA, K.; MASON, N. Electron impact calculations of total elastic cross sections over a wide energy range—0.01 eV to 2 keV for CH_4 , SiH_4 and H_2O . **The European Physical Journal D**, Springer, v. 61, p. 579–585, 2011. Cit. on pp. 29, 79, 87–89, 100, 102.
- 67 SOHN, W.; KOCHER, K.-H.; SCHEUERLEIN, K.-M.; JUNG, K.; EHRHARDT, H. Elastic electron scattering from CH_4 for collision energies between 0.2 and 5 eV. **Journal of Physics B: Atomic and Molecular Physics**, IOP Publishing, v. 19,

- n. 21, p. 3625, 1986. Cit. on pp. 29, 79, 87–90, 92, 100, 102.
- 68 SHYN, T.; CRAVENS, T. E. Angular distribution of electrons elastically scattered from CH₄. **Journal of Physics B: Atomic, Molecular and Optical Physics**, IOP Publishing, v. 23, n. 2, p. 293, 1990. Cit. on pp. 29, 79, 87, 88, 90, 92, 100, 102.
- 69 BOESTEN, L.; TANAKA, H. Elastic DCS for e⁺ CH₄ collisions, 1.5–100 eV. **Journal of Physics B: Atomic, Molecular and Optical Physics**, IOP Publishing, v. 24, n. 4, p. 821, 1991. Cit. on pp. 29, 79, 80, 87, 88, 90, 92, 100, 102.
- 70 VUŠKOVIC, L.; TRAJMAR, S. Electron impact excitation of methane. **The Journal of Chemical Physics**, American Institute of Physics, v. 78, n. 8, p. 4947–4951, 1983. Cit. on pp. 29, 80, 87, 88, 96, 100, 102.
- 71 WINSTEAD, C.; SUN, Q.; MCKOY, V.; LINO, J. L.; LIMA, M. A. Electronic excitation of CH₄ by low-energy electron impact. **The Journal of chemical physics**, American Institute of Physics, v. 98, n. 3, p. 2132–2137, 1993. Cit. on pp. 29, 45, 80, 82, 83, 92–97, 100, 102.
- 72 GIL, T. J.; LENGFIELD, B. H.; MCCURDY, C. W.; RESCIGNO, T. N. Ab initio complex Kohn calculations of dissociative excitation of methane: Close-coupling convergence studies. **Physical Review A**, APS, v. 49, n. 4, p. 2551, 1994. Cit. on pp. 29, 45, 80, 82, 83, 92–94, 97, 98, 100, 102.
- 73 BETTEGA, M.; FERREIRA, L.; LIMA, M. Electronic excitation of XH₄ (X= C, Si, Ge, Sn, Pb) by electron impact. **Physical Review A**, APS, v. 57, n. 6, p. 4987, 1998. Cit. on pp. 29, 45, 80–83, 92–94, 100, 102.
- 74 JOSHIPURA, K.; VINODKUMAR, M.; LIMBACHIYA, C.; ANTONY, B. Calculated total cross sections of electron-impact ionization and excitations in tetrahedral (XY₄) and SF₆ molecules. **Physical Review A**, APS, v. 69, n. 2, p. 022705, 2004. Cit. on pp. 29, 80, 97, 98.
- 75 ZIÓŁKOWSKI, M.; VIKÁR, A.; MAYES, M. L.; BENCSURA, Á.; LENDVAY, G.; SCHATZ, G. C. Modeling the electron-impact dissociation of methane. **The Journal of Chemical Physics**, AIP Publishing, v. 137, n. 22, 2012. Cit. on pp. 29, 80, 82, 83, 87–89, 92–94, 100, 102.
- 76 JOACHAIN, C. J. **Quantum Collision Theory**. Mineola, New York: Dover Publica-

- tion, 1975. Cit. on pp. 30–35, 54, 55.
- 77 SZABO, A.; OSTLUND, N. S. **Modern Quantum Chemistry: Introduction to Advanced Electronic Structure Theory**. Amsterdam, The Netherlands: North-Holland, 1996. Cit. on pp. 33, 45–47.
- 78 COSTA, R. F. da; VARELLA, M. T. d. N.; BETTEGA, M. H.; LIMA, M. A. Recent advances in the application of the Schwinger multichannel method with pseudopotentials to electron-molecule collisions. **The European Physical Journal D**, Springer, v. 69, p. 1–24, 2015. Cit. on pp. 34, 140.
- 79 VARELLA, M. O método multicanal de Schwinger aplicado ao espalhamento de elétrons: aspectos formais. **Physicae**, v. 1, n. 1, p. 45–53, 2000. Cit. on pp. 34, 39, 41.
- 80 BARBOSA, A. S. Espalhamento elástico de elétrons e pósitrons por moléculas cíclicas. Tese de doutorado, Pós-Graduação em Física, Universidade Federal do Paraná, Curitiba, 2017. Cit. on p. 34.
- 81 MOREIRA, G. M. Espalhamento de elétrons e pósitrons por moléculas: espalhamento elástico, acoplamento multicanal e microssolvatação. Tese de doutorado, Pós-Graduação em Física, Universidade Federal do Paraná, Curitiba, 2020. Cit. on p. 34.
- 82 SCHWINGER, J. A variational principle for scattering problems. **Physical Review**, v. 72, n. 8, p. 742–742, 1947. Cit. on p. 34.
- 83 GELTMAN, S. **Topics in Atomic Collision Theory**. New York, New York: New York: Academic Press, 1969. Cit. on p. 37.
- 84 LIMA, M. A.; MCKOY, V. Aspects of the Schwinger multichannel variational formulation. **Physical Review A**, APS, v. 38, n. 1, p. 501, 1988. Cit. on pp. 38, 39.
- 85 LIMA, M. A.; BRESCANSIN, L. M.; SILVA, A. J. da; WINSTEAD, C.; MCKOY, V. Applications of the Schwinger multichannel method to electron-molecule collisions. **Physical Review A**, APS, v. 41, n. 1, p. 327, 1990. Cit. on p. 40.
- 86 BACHELET, G. B.; HAMANN, D. R.; SCHLÜTER, M. Pseudopotentials that work:

- From H to Pu. **Physical Review B**, APS, v. 26, n. 8, p. 4199, 1982. Cit. on pp. 40, 125, 142.
- 87 BETTEGA, M.; FERREIRA, L.; LIMA, M. Transferability of local-density norm-conserving pseudopotentials to electron-molecule-collision calculations. **Physical Review A**, APS, v. 47, n. 2, p. 1111, 1993. Cit. on pp. 40, 142.
- 88 BETTEGA, M. H. F. Espalhamento de Elétrons por Moléculas através de Pseudopotenciais Local Density. Tese de doutorado, Instituto de Física Gleb-Wataghin, Universidade Estadual de Campinas, Campinas, 1993. Cit. on p. 40.
- 89 SANTOS, J. S. d.; COSTA, R. F. da; VARELLA, M. T. d. N. Low-energy electron collisions with glycine. **The Journal of Chemical Physics**, AIP Publishing, v. 136, n. 8, 2012. Cit. on p. 40.
- 90 TAŃSKA, N.; RANDI, P. A.; STEFANOWSKA-TUR, S.; MOREIRA, G. M.; PTASIŃSKA-DENGA, E.; BETTEGA, M. H.; SZMYTKOWSKI, C.; MOŻEJKO, P. Joint experimental and theoretical study on electron scattering from titanium tetrachloride (TiCl₄) molecule. **The Journal of Chemical Physics**, AIP Publishing, v. 157, n. 15, 2022. Cit. on p. 43.
- 91 SILVA, M. O.; MOREIRA, G. M.; COSTA, R. F. da; BETTEGA, M. H. Elastic Electron Scattering by Diborane (6) and Diborane (4) Molecules. **The Journal of Physical Chemistry A**, ACS Publications, v. 126, n. 38, p. 6710–6718, 2022. Cit. on p. 43.
- 92 KOSSOSKI, F.; BETTEGA, M. Low-energy electron scattering from the azaderivatives of pyrrole, furan, and thiophene. **The Journal of Chemical Physics**, AIP Publishing, v. 138, n. 23, 2013. Cit. on pp. 43, 125.
- 93 COSTA, R. F. da; PAIXAO, F. J. da; LIMA, M. A. Cross sections for electron-impact excitation of the H₂ molecule using the MOB-SCI strategy. **Journal of Physics B: Atomic, Molecular and Optical Physics**, IOP Publishing, v. 38, n. 24, p. 4363, 2005. Cit. on pp. 45, 46, 61, 82.
- 94 DUNNING JR, T.; HUNT, W.; GODDARD III, W. The theoretical description of the ($\pi\pi^*$) excited states of ethylene. **Chemical Physics Letters**, Elsevier, v. 4, n. 3, p. 147–150, 1969. Cit. on pp. 45, 46, 61, 81, 125.

- 95 MOREIRA, G.; BETTEGA, M.; COSTA, R. da. Elastic and electronically inelastic electron collisions by the thiophene molecule. **Journal of Applied Physics**, AIP Publishing, v. 129, n. 20, 2021. Cit. on pp. 47, 54.
- 96 RANDI, P. A.; MOREIRA, G. M.; BETTEGA, M. H. Electron collisions with formic acid. **The European Physical Journal D**, Springer, v. 75, n. 12, p. 306, 2021. Cit. on pp. 47, 54.
- 97 FALKOWSKI, A. G.; BETTEGA, M. H.; LIMA, M. A.; FERREIRA, L. G. A model potential for computing total ionization cross sections of atoms and molecules by electron impact. **The European Physical Journal D**, Springer, v. 75, p. 1–7, 2021. Cit. on p. 51.
- 98 KIM, Y.-K.; RUDD, M. E. Binary-encounter-dipole model for electron-impact ionization. **Physical Review A**, APS, v. 50, n. 5, p. 3954, 1994. Cit. on pp. 51, 61.
- 99 LOUPAS, A.; REGETA, K.; ALLAN, M.; GORFINKIEL, J. D. Shape and core-excited resonances in thiophene. **The Journal of Physical Chemistry A**, ACS Publications, v. 122, n. 4, p. 1146–1155, 2018. Cit. on p. 54.
- 100 FALKOWSKI, A. G. Excitação eletrônica do etanol por impacto de elétrons de baixa energia. **Dissertação de mestrado**, 2020. Cit. on p. 56.
- 101 COSTA, R. F. da; BETTEGA, M. H.; VARELLA, M. T. d. N.; OLIVEIRA, E. M. de; LIMA, M. A. Electron collisions with ethylene: The role of multichannel-coupling effects. **Physical Review A**, APS, v. 90, n. 5, p. 052707, 2014. Cit. on p. 57.
- 102 WIGNER, E. P. On the behavior of cross sections near thresholds. **Physical Review**, APS, v. 73, n. 9, p. 1002, 1948. Cit. on p. 57.
- 103 NEWTON, R. G. **Scattering Theory of Waves and Particles**. Mineola, New York: Unabridge Dover, 2002. Cit. on p. 57.
- 104 ČÍŽEK, M.; HORÁČEK, J.; ALLAN, M.; DOMCKE, W. Resonances and threshold phenomena in low-energy electron collisions with hydrogen halides: new experimental and theoretical results. **Czechoslovak Journal of Physics**, Springer, v. 52, p. 1057–1070, 2002. Cit. on p. 57.

- 105 BARCA, G. M.; BERTONI, C.; CARRINGTON, L.; DATTA, D.; DE SILVA, N.; DEUSTUA, J. E.; FEDOROV, D. G.; GOUR, J. R.; GUNINA, A. O.; GUIDEZ, E., et al. Recent developments in the general atomic and molecular electronic structure system. **The Journal of Chemical Physics**, AIP Publishing, v. 152, n. 15, 2020. Cit. on pp. 61, 65, 86, 125, 148.
- 106 DUNNING JR, T. H. Gaussian basis functions for use in molecular calculations. I. Contraction of (9s5p) atomic basis sets for the first-row atoms. **The Journal of Chemical Physics**, American Institute of Physics, v. 53, n. 7, p. 2823–2833, 1970. Cit. on pp. 61, 81, 125.
- 107 EMRICH, K. An extension of the coupled cluster formalism to excited states (I). **Nuclear Physics A**, Elsevier, v. 351, n. 3, p. 379–396, 1981. Cit. on pp. 62, 82.
- 108 SEKINO, H.; BARTLETT, R. J. A linear response, coupled-cluster theory for excitation energy. **International Journal of Quantum Chemistry**, Wiley Online Library, v. 26, S18, p. 255–265, 1984. Cit. on pp. 62, 82.
- 109 STANTON, J. F.; BARTLETT, R. J. The equation of motion coupled-cluster method. A systematic biorthogonal approach to molecular excitation energies, transition probabilities, and excited state properties. **The Journal of Chemical Physics**, American Institute of Physics, v. 98, n. 9, p. 7029–7039, 1993. Cit. on pp. 62, 82.
- 110 BARTLETT, R. J. Coupled-cluster theory and its equation-of-motion extensions. **Wiley Interdisciplinary Reviews: Computational Molecular Science**, Wiley Online Library, v. 2, n. 1, p. 126–138, 2012. Cit. on pp. 62, 82.
- 111 SMITH, D. G.; BURNS, L. A.; SIMMONETT, A. C.; PARRISH, R. M.; SCHIEBER, M. C.; GALVELIS, R.; KRAUS, P.; KRUSE, H.; DI REMIGIO, R.; ALENAIZAN, A., et al. PSI4 1.4: Open-source software for high-throughput quantum chemistry. **The Journal of Chemical Physics**, AIP Publishing, v. 152, n. 18, 2020. Cit. on pp. 62, 82.
- 112 CHONG, D. P. Density functional theory study of the electron spectra of formamide vapor. **Journal of Electron Spectroscopy and Related Phenomena**, Elsevier, v. 184, n. 3-6, p. 164–169, 2011. Cit. on pp. 62, 63.
- 113 HIRST, J. D.; HIRST, D. M.; BROOKS, C. L. Ab initio calculations of the excited states of formamide. **The Journal of Physical Chemistry**, ACS Publications,

- v. 100, n. 32, p. 13487–13491, 1996. Cit. on pp. 62, 63.
- 114 GINGELL, J.; MASON, N.; ZHAO, H.; WALKER, I.; SIGGEL, M. VUV optical-absorption and electron-energy-loss spectroscopy of formamide. **Chemical Physics**, Elsevier, v. 220, n. 1-2, p. 191–205, 1997. Cit. on pp. 62, 63.
- 115 STALEY, R. H.; HARDING, L. B.; GODDARD III, W. A.; BEAUCHAMP, J. Triplet states of the amide group. Trapped electron spectra of formamide and related molecules. **Chemical Physics Letters**, Elsevier, v. 36, n. 5, p. 589–593, 1975. Cit. on pp. 62, 63.
- 116 BASCH, H.; ROBIN, M. B.; KUEBLER, N. Electronic states of the amide group. **The Journal of Chemical Physics**, American Institute of Physics, v. 47, n. 4, p. 1201–1210, 1967. Cit. on pp. 62, 63.
- 117 NELSON, R. D.; LIDE, D. R.; MARYOTT, A. A., et al. **Selected values of electric dipole moments for molecules in the gas phase**. Washington, D.C: US National Bureau of Standards Washington, 1967. v. 10. Cit. on p. 65.
- 118 MOREIRA, G.; BETTEGA, M.; COSTA, R. da. Elastic and electronically inelastic electron collisions by the thiophene molecule. **Journal of Applied Physics**, AIP Publishing, v. 129, n. 20, 2021. Cit. on p. 73.
- 119 RANDI, P. A.; MOREIRA, G. M.; BETTEGA, M. H. Electron collisions with formic acid. **The European Physical Journal D**, Springer, v. 75, n. 12, p. 306, 2021. Cit. on p. 73.
- 120 FALKOWSKI, A. G.; COSTA, R. F. da; KOSSOSKI, F.; BRUNGER, M. J.; LIMA, M. A. Electronic excitation of benzene by low energy electron impact and the role of higher lying Rydberg states. **The European Physical Journal D**, Springer, v. 75, n. 12, p. 310, 2021. Cit. on p. 73.
- 121 TANAKA, H.; OKADA, T.; BOESTEN, L.; SUZUKI, T.; YAMAMOTO, T.; KUBO, M. Differential cross sections for elastic scattering of electrons by CH₄ in the energy range of 3 to 20 eV. **Journal of Physics B: Atomic and Molecular Physics**, IOP Publishing, v. 15, n. 18, p. 3305, 1982. Cit. on pp. 80, 96.
- 122 KIM, Y.-K.; HWANG, W.; WEINBERGER, N.; ALI, M.; RUDD, M. E. Electron-impact ionization cross sections of atmospheric molecules. **The Journal of chemical**

- physics**, American Institute of Physics, v. 106, n. 3, p. 1026–1033, 1997. Cit. on pp. 80, 98, 99.
- 123 DEUTSCH, H.; BECKER, K.; MATT, S.; MÄRK, T. Theoretical determination of absolute electron-impact ionization cross sections of molecules. **International Journal of Mass Spectrometry**, Elsevier, v. 197, n. 1-3, p. 37–69, 2000. Cit. on pp. 80, 98.
- 124 MEBEL, A. M.; LIN, S.-H.; CHANG, C.-H. Theoretical study of vibronic spectra and photodissociation pathways of methane. **The Journal of chemical physics**, American Institute of Physics, v. 106, n. 7, p. 2612–2620, 1997. Cit. on pp. 82, 83.
- 125 HARSHBARGER, W. R.; LASSETTRE, E. N. On the electron impact spectra of CH₄ and CF₄. **The Journal of Chemical Physics**, American Institute of Physics, v. 58, n. 4, p. 1505–1513, 1973. Cit. on pp. 82, 83.
- 126 DILLON, M.; WANG, R.-G.; SPENCE, D. Electron impact spectroscopy of methane and methane-d 4. **The Journal of Chemical Physics**, American Institute of Physics, v. 80, n. 11, p. 5581–5588, 1984. Cit. on pp. 82, 83.
- 127 BRONGERSMA, H.; OOSTERHOFF, L. Singlet-triplet excitation of saturated hydrocarbons by low-energy electron impact. **Chemical Physics Letters**, Elsevier, v. 3, n. 6, p. 437–440, 1969. Cit. on pp. 82, 83.
- 128 CHIARI, L.; ZECCA, A.; BLANCO, F.; GARCÍA, G.; BRUNGER, M. Experimental and theoretical cross sections for positron scattering from the pentane isomers. **The Journal of Chemical Physics**, AIP Publishing LLC, v. 144, n. 8, p. 084301, 2016. Cit. on p. 124.
- 129 RANDI, P. A.; SILVA, M. O.; MOREIRA, G. M.; COSTA, R. F. da; BETTEGA, M. H. Methylation and isomerization effects on the elastic electron scattering cross sections by H₂O₂ and C₂H₆O₂. **The European Physical Journal D**, Springer, v. 77, n. 6, p. 120, 2023. Cit. on pp. 124, 128.
- 130 HOLLIS, J. M.; LOVAS, F. J.; JEWELL, P. R.; COUDERT, L. Interstellar antifreeze: ethylene glycol. **The Astrophysical Journal**, IOP Publishing, v. 571, n. 1, p. l59, 2002. Cit. on p. 124.
- 131 KNOP, K.; HOOGENBOOM, R.; FISCHER, D.; SCHUBERT, U. S. Poly (ethylene

- glycol) in drug delivery: pros and cons as well as potential alternatives. **Angewandte Chemie International Edition**, Wiley Online Library, v. 49, n. 36, p. 6288–6308, 2010. Cit. on p. 124.
- 132 CHOI, C.; HWANG, I.; CHO, Y.-L.; HAN, S. Y.; JO, D. H.; JUNG, D.; MOON, D. W.; KIM, E. J.; JEON, C. S.; KIM, J. H., et al. Fabrication and characterization of plasma-polymerized poly (ethylene glycol) film with superior biocompatibility. **ACS Applied Materials & Interfaces**, ACS Publications, v. 5, n. 3, p. 697–702, 2013. Cit. on p. 124.
- 133 SAKTHI KUMAR, D.; FUJIOKA, M.; ASANO, K.; SHOJI, A.; JAYAKRISHNAN, A.; YOSHIDA, Y. Surface modification of poly (ethylene terephthalate) by plasma polymerization of poly (ethylene glycol). **Journal of Materials Science: Materials in Medicine**, Springer, v. 18, p. 1831–1835, 2007. Cit. on p. 124.
- 134 ARAÚJO, N. F.; LARA, T. F.; SOUZA, G. L. de. Electron interactions with C₂H₆O₂ isomers. **Journal of Electron Spectroscopy and Related Phenomena**, Elsevier, v. 245, p. 147012, 2020. Cit. on pp. 124, 126–133, 135, 136, 139.
- 135 SAKURAI, J. J.; NAPOLITANO, J. **Modern Quantum Mechanics**. 3rd. Cambridge: Cambridge University Press, 2021. Cit. on p. 143.

Appendix

APPENDIX A

Scientific contributions

During the pursue for my master's degree I was fortunate enough to work with renowned scientists in the field. The combination between these contributions and hard work provided many scientific crops. Evidently, this would not be possible without my supervisor professor Márcio Henrique Franco Bettega, who had an incalculable impact on my development as a scientist. I am eternally grateful for his mentorship and friendship during the past few years.

As mentioned throughout the main body of the dissertation itself professor Giseli Maria Moreira also participated in many of the projects I worked on. From these contributions, the following paper was published:

- Randi, P. A. S.; Moreira, G. M.; Bettega, M. H. F. Electron scattering by formamide: Elastic and electronically inelastic cross sections up to 179 energetically open states. **Physical Review A**, v. 107, n. 1, p. 012806, 2023.

DOI: <https://doi.org/10.1103/PhysRevA.107.012806>

Besides that, I also had the opportunity to collaborate with Professor Romarly Fernandes da Costa and Dr. Murilo de Oliveira da Silva. Their contributions were fundamental to my scientific development, and I learned a great deal from them. Our collaborative efforts resulted in the publication of the following work:

- Randi, P. A. S.; Silva, M. O.; Moreira, G. M.; da Costa, R. F.; Bettega, M. H. F. Methylation and isomerization effects on the elastic electron scattering cross sections by H_2O_2 and $\text{C}_2\text{H}_6\text{O}_2$. **The European Physical Journal D**, v. 77, n. 6, p. 120, 2023.

DOI: <https://doi.org/10.1140/epjd/s10053-023-00697-3>

Additionally, I presented an oral contribution entitled "Elastic and electronically inelastic scattering of electrons by molecular targets" in the Brazilian Physics Society Autumn Meeting, which took place in Ouro Preto, MG from May 21 to 25, 2023. In the same event, I also presented the poster "Elastic and electronically inelastic electron scattering by methane", which was given the award of best poster in the thematic area "Atomic and Molecular Collisions" and was amongst the three selected best poster overall by IOP. Also, in the IV Workshop of the Postgraduate Program in Physics of UFPR I presented the poster "ELECTRONIC EXCITATION OF FORMAMIDE BY ELECTRON IMPACT", and in the V Workshop of the Postgraduate Program in Physics of UFPR the poster "Elastic and electronically inelastic scattering of electrons by methane". At the XV WFME (Workshop em Física Molecular e Espectroscopia) 2023, which took place in São Paulo between 17 and 20 of octobere I also presented two posters: "Elastic and electronically inelastic scattering of electrons by methane" and "Elastic low-energy electron collisions with the tetramethyltin molecule".

I also had the opportunity and honor to closely work with professor Paulo Limão-Vieira from the Universidade Nova de Lisboa, Portugal, in the characterization of the photoabsorption spectra of formic acid, 2-fluorotoluene and 2-chlorotoluene. This valuable experience was proportioned by professor Alessandra Souza Barbosa, who played a direct role in these projects. I am immensely grateful to her. These projects not only provided an enjoyable and enriching experience for me but also contributed significantly to my academical development. My role in these projects was to perform state-of-art electronic structure calculations for the electronically excited states of the molecules under investigation. These results assisted in the characterization of the photoabsorption spectra measured by professor Paulo and his collaborators in Europe. From these joint efforts, the following papers were published:

- Randi, P. A. S.; Pastega, D. F.; Bettega, M. H. F.; Jones, N. C.; Hoffmann, S. V.; Eden, S.; Souza Barbosa, A.; Limão-Vieira, P. Electronically excited states of formic acid investigated by theoretical and experimental methods. **Spectrochimica Acta Part A: Molecular and Biomolecular Spectroscopy**, v 289, p. 122237, 2023.

DOI: <https://doi.org/10.1016/j.saa.2022.122237>

- Randi, P. A. S.; Kumar, S.; Lozano, A. I.; Bettega, M. H. F.; Hoffman, S. V.; Jones, N. C.; Souza Barbosa, A.; Limão-Vieira, P. Valence and Rydberg excitations of 2-fluorotoluene in the 4.4–10.8 eV photoabsorption energy region. **Journal of Quantitative Spectroscopy and Radiative Transfer**, v. 303, p. 108597, 2023.

DOI: <https://doi.org/10.1016/j.jqsrt.2023.108597>

Furthermore, during my undergraduation I performed calculations on the elastic electron scattering by titanium tetrachloride. This project grew up to be an international collaboration with professor Paweł Możejko and his research group from Poland. They measured the total cross section for the scattering of electrons by titanium tetrachloride and calculated the elastic integral cross section using the R-Matrix method. This contribution yielded the work published during the first year of my master's program:

- Tańska, N.; Randi, P. A. S.; Stefanowska-Tur, S.; Moreira, G. M.; Ptasińska-Denga, E.; Bettega, M. H. F.; Szmytkowski, C.; Możejko, P. Joint experimental and theoretical study on electron scattering from titanium tetrachloride (TiCl_4) molecule. **The Journal of Chemical Physics**, v. 157, n. 15, 2022.

DOI: <https://doi.org/10.1063/5.0116713>

APPENDIX B

Dimethyl Peroxide and Ethylene Glycol

From an academical perspective, another interesting subject is the effect that small changes in the molecular structure, such as methylation, isomerization, halogenation and others have on electron scattering cross sections. More specifically, isomerization effects on electron scattering cross sections have been a topic of discussion in the literature, that is, how the rearrangement of atoms that compose a molecule affect its interaction with LEEs. A thorough survey of the literature on this subject can be found in the introduction of the work where Brunger and collaborators investigated positron scattering by isomers of pentane through a joint experimental and theoretical

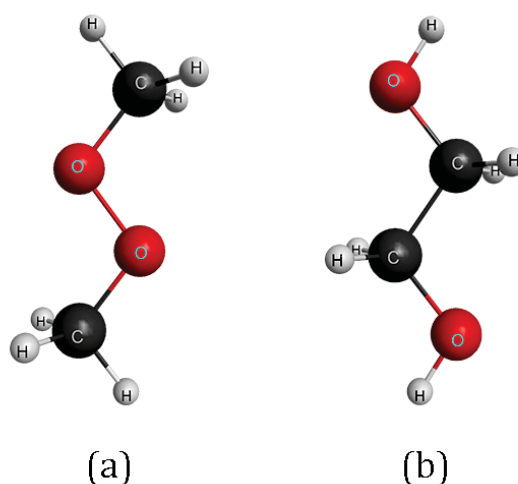


Figure B.1 – Ball and stick model of the chemical structure of (a) dimethyl peroxide and (b) ethylene glycol (generated with MacMolPlt [35]).

effort [128]. The overall consensus on this matter is that differences in the cross sections for isomers are more appreciable at low scattering energies. Broadly stating, in the low-energy regime, the de Broglie wavelength associated to the incident electron is comparable to the size of the target molecule and, as a consequence, small changes in its structure become apparent to the projectile. For instance, the de Broglie wavelength of an electron that collides with benzene at an energy of 1 eV is around 12 Å, while the distance from opposing hydrogen atoms in the benzene ring is approximately 5 Å. As the incident electron energy increases, the de Broglie wavelength decreases, and the details of the molecular structure are not distinguishable to the incident electron anymore. At 50 eV, the de Broglie wavelength of the incident electron becomes 1.7 Å. Thus, significant differences in cross sections for isomers should be observed in the low energy regime and, as the impact energy increases, the cross sections become similar.

In this appendix we will present the cross sections for the elastic electron scattering by the isomers dimethyl peroxide (DMP) and ethylene glycol (ETG) (Figure B.1). These calculations were part of a broader collaboration involving Dr. Murilo de Oliveira Silva, professor Giseli Maria Moreira and professor Romarly Fernandes da Costa, where we investigated the methylation and isomerization effects on the elastic scattering cross sections of hydrogen peroxide, DMP and ETG. Since Murilo was responsible for calculating the cross sections for hydrogen peroxide and this dissertation concerns my contributions, here we restrain the discussion to the cross sections calculated by myself. The complete work, including Murilo's contributions and all analysis, can be found in the literature [129]. Nevertheless, the collaboration with esteemed researchers has undoubtedly enriched the depth and quality of the results and discussions presented here and throughout all this dissertation.

ETG is a molecule that has been detected in the interstellar medium [130] and it is the building block of Poly(ethylene glycol), which is a bio-compatible polymer used in polymer-based drug delivery in a variety of applications in pharmaceuticals [131]. This polymer can be manufactured and improved using techniques that involves low-temperature plasma processing [132, 133]. As a consequence, understanding how this molecule interacts with low-energy electrons (LEEs) has direct consequences to applications in astrophysics and technology. Although DMP does not present any direct applications involving its interaction with low-energy electrons, from the academical point of view, to understand how LEEs interact with DMP and ETG enables us to investigate how the different arrangements of atoms in the molecule affect the cross sections.

Only one work reported electron scattering cross sections for DMP and ETG in the literature [134]. In their work, Araújo *et al.* calculated the differential (DCS), integral (ICS), momentum transfer (MTCS), total absorption and total cross sections up to 500 eV using the molecular complex optical potential (MCOP) method combined

with the Padé approximation technique. The authors found a narrow well localized B_u resonance at 5 eV for DMP, assigned to the O-O bond, having a σ^* character. For ETG, a broad resonance was observed at around 10 eV with contributions from the A_u and B_u symmetries.

Here, we performed calculations for the elastic electron scattering by DMP and ETG. The cross sections were calculated with the SMCPP method in SE and SEP approximations for incident electrons energies up to 30 eV. Additionally, interesting isomerization effects were also observed in the present results.

B.1 Computational Details

The geometries of the molecules were optimized at the second order Møller-Plesset perturbation theory (MP2) with the aug-cc-pVDZ basis set using the computational package GAMESS [105], in the C_{2h} point group. As discussed in chapter 2, in the SMCPP method, the ground state of the molecular target is described within the Hartree-Fock approximation. For the O and C atoms the core electrons were replaced by the norm-conserving pseudopotentials of Bachelet, Hamann and Schlüter [86] and the basis set used for the valence electrons contains $5s$, $5p$ and $3d$ CG functions and was taken from Bettega [42]. For the H atoms, the $4s/3s$ basis set of Dunning [106] with one additional p -type function with exponent 0.75 was used.

In the SE approximation, the virtual orbitals obtained from the Hartree-Fock calculation were used as scattering orbitals, while in the SEP approximation improved virtual orbitals (IVOs) [94] were used as particle and scattering orbitals. These IVOs were generated with triplet spin coupling using the highest occupied molecular orbital of a_g symmetry as the hole orbital. Two distinct strategies were employed to select the hole-particle pairs used to construct the configuration space in the SEP calculation. For the B_u symmetry of both molecules we have adopted the energy cutoff strategy. In this strategy, the single excitations are selected according to relation: $\varepsilon_{\text{part}} - \varepsilon_{\text{hole}} + \varepsilon_{\text{scat}} < \Delta$ [92], where $\varepsilon_{\text{part}}$ is the particle orbital energy, $\varepsilon_{\text{hole}}$ is the hole orbital energy, $\varepsilon_{\text{scat}}$ is the scattering orbital energy, and Δ is the energy cutoff, which we use the value of 2.7 hartree. We used the same Δ value for both molecules and considered singlet- and triplet-coupled excitations. This strategy was chosen for this symmetry in order to provide an equivalent description of the polarization effects in the calculations for DMP and hydrogen peroxide (not shown here), since one of the goals of the project was to understand how the low-energy resonance of hydrogen peroxide would behave when methyl groups are added to the molecule. To have a balanced comparison between the calculated cross sections, polarization effects needed to be equivalently described in both calculations, leading to the choice of using the energy cut-off strategy for this symmetry. For the

Table B.1 – Number of configuration state functions per symmetry used in the static-exchange plus polarization approximation calculation for each molecule.

Symmetry	DMP	ETG
A_g	15 934	15 934
A_u	14 209	14 209
B_g	14 211	14 211
B_u	15 859	15 902

remaining symmetries we used all 13 occupied orbitals as hole orbitals and the first 68 unoccupied IVOs as particle and scattering orbitals to construct the configuration space used in the SEP calculations. The number of CSFs per symmetry is presented in Tab. B.1.

B.2 Dimethyl Peroxide

The ICS and MTCS calculated in both SE and SEP approximations and the results from Araújo *et al.* [134] for DMP are presented in Fig. B.2. In the SE approximation two broad overlapping structures are seen centered around 6.5 eV and 10 eV. These structures shift towards lower energies when polarization effects are included in the calculations, such that in the SEP approximation the first structure appears as a distinct sharp peak centred at 2.1 eV, while the second one is a very broad structure centered around 8.5 eV. The low-energy behaviour of the cross section also changes expressively as the polarization effects are included: from an increasingly larger cross section as the energy tends to zero in the SE approximation, to a small cross section in the SEP approximation. These changes are expected and are related to the relevance of the polarization effects in the low-energy regime, as discussed in chapter 2. At higher energies magnitude of the cross sections calculated in both approximations are similar and the main difference is that in the SEP approximation pseudoresonances appear due to closed channels.

When comparing the present ICS and MTCS to the ones from Araújo *et al.* [134] an overall good agreement is found. Both structures seen by the authors are also observed in our results, although in different energies: the structures are shifted towards higher energies in the SE approximation and towards lower energies in the SEP approximation. This is a consequence of the different treatment of the polarization effects in the calculations. In the SE approximation, the effective potential felt by the incoming electron is the least attractive due to the absence of polarization effects, leading to a higher position of these structures. When polarization effects are included in the calculation the effective potential becomes more attractive, lowering the position of the structures in the cross sections. Araújo *et al.* [134] performed the calculation using a model potential to

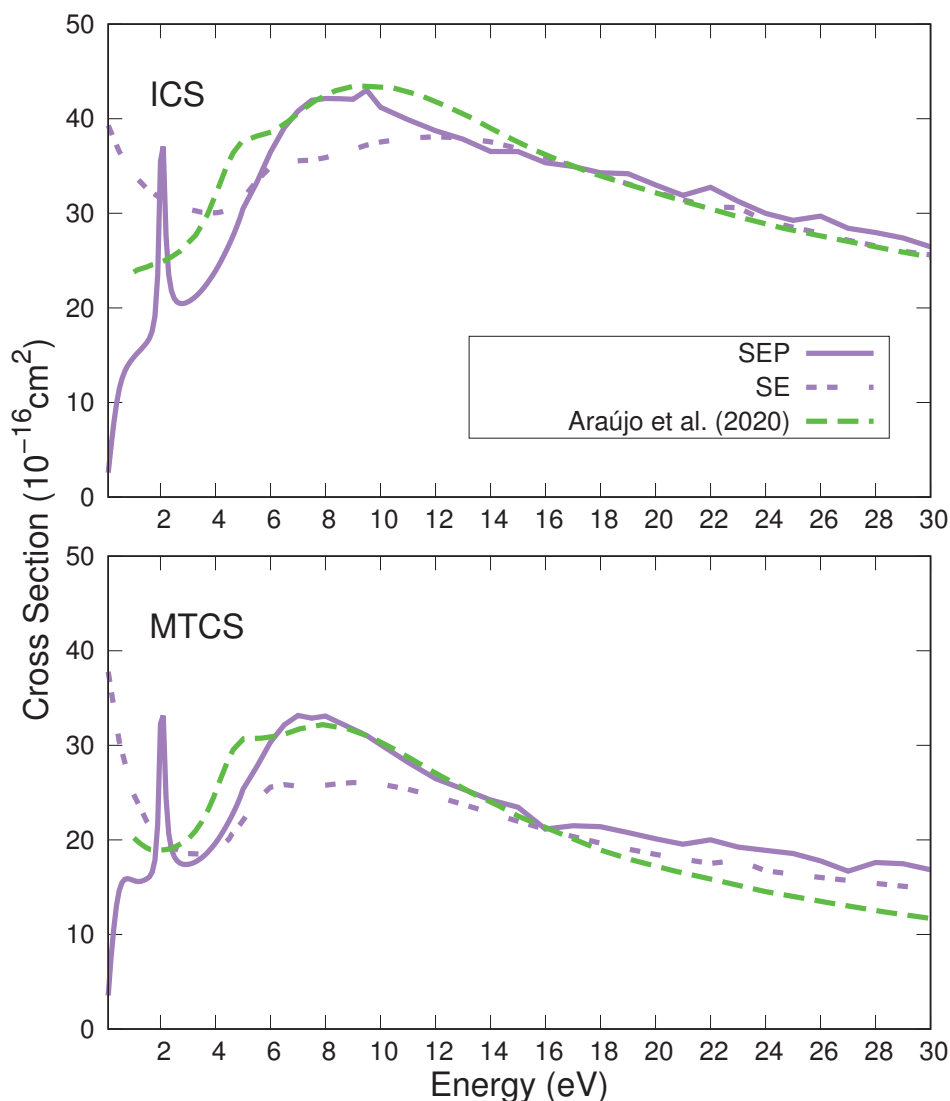


Figure B.2 – Upper panel: ICS for the electrons scattering by DMP Lower panel: MTCS for the electron scattering by DMP. For both panels: full purple line, SEP results; double-dotted purple line, SE results; dashed green line, results from Araújo *et al.* [134].

describe the interaction between the incident electron and the molecular target. Based on the position of the structures in the cross sections, this treatment seems to lead to an effective potential that is not as attractive as the one in the present SEP calculation, since the structures seen by Araújo *et al.* [134] are at higher energies than the ones in the SEP ICS. Unfortunately, the lack of experimental data in the literature inhibits any further analysis regarding these discrepancies. At higher energies, where polarization effects are not as relevant, all cross sections agree well.

To shed more light on the features observed in the ICSs we present in Fig. B.3 the symmetry decomposition of the ICSs calculated in both SE and SEP approximations according to the C_{2h} point group. For comparison, we also included in Fig. B.3 the results

from Araújo *et al.* [134]. According to our results, the low-energy structure that appears in the SEP ICS centered at 2.1 eV arises from the B_u symmetry¹, while the higher energy structure has contributions from all symmetries. To further analyze the origin of these structures and assign possible resonances we diagonalized the scattering Hamiltonian in the configuration space used in the SEP calculation. In Fig. B.4 the resonant orbitals generated from the diagonalization of the scattering Hamiltonian, through equation (2.73), are presented. We found a resonant eigenstate with an energy eigenvalue of 1.70 eV in the B_u symmetry. The orbital generated from this eigenstate has a component in the O-O bond. Thus, this resonance may be associated with the σ^* resonance of hydrogen peroxide [129]. The high-energy broad structure that appears in the SEP ICS is a superposition of three wide resonances belonging to A_g , A_u and B_u symmetries. The A_g resonance is seen in the SEP cross section as a small bump centered at 6.0 eV and the H_{N+1} eigenstate corresponding to this resonance has an energy eigenvalue of 6.28 eV, with a C-O and C-H components in the corresponding orbital. The A_u and B_u resonances are centered at 8.0 eV and 7.5 eV in the cross section and the corresponding resonant H_{N+1} eigenstates have eigenvalues of 6.36 eV and 6.64 eV, respectively. The orbitals corresponding to these eigenstates are located at the C-H bonds. The diagonalization of the scattering Hamiltonian did not indicate a resonant state of B_g symmetry. Thus, the wide structure that appears in the B_g cross sections depicted in Fig. B.3 is due to a non-resonant background. Another interesting feature that shows up in the symmetry decomposition of the SEP ICS is a small structure in the B_u symmetry below 1 eV. Since this do not have a corresponding structure in the SE approximation it cannot be assigned to resonance. Thus, an angular momentum barrier effects gives rise to the low-energy structure observed in the B_u SEP ICS.

In addition to the anylis of the last paragraph, in Fig. B.5 the partial wave decomposition of the cross sections of each symmetry of DMP, along the respective eigenphase sum, are presented. The low-energy structure in the B_u cross section has contributions from partial waves with $\ell = 1$ and 3. Furthermore, the jump in the eigenphase sum around the energy of this structure is a signature of resonant behaviour. The sharp and very pronounced structure in the ICS, the resonant eigenstate of the scattering Hamiltonian and the signature in the eigenphase sum makes for a straightforward assignment of this resonance. In contrast, the higher lying broad resonances are trickier to characterize. The signature in the eigenphase sum around the higher resonance of B_u symmetry (7.5 eV) together with the presence of resonant eigenstates of the scattering Hamiltonian close to this energy led to the resonance characterization. Note also that this resonance has contributions from the $\ell = 1$ and 3 partial waves. There is no evidence that supports a B_g symmetry resonance: neither a Lorentzian peak

¹ The structure around 2.1 eV in the A_g symmetry is due to the $l = 0$ wave as shown in Fig. B.5. Thus, the resonance seen in the SEP ICS around this energy is only associated with the B_u symmetry.

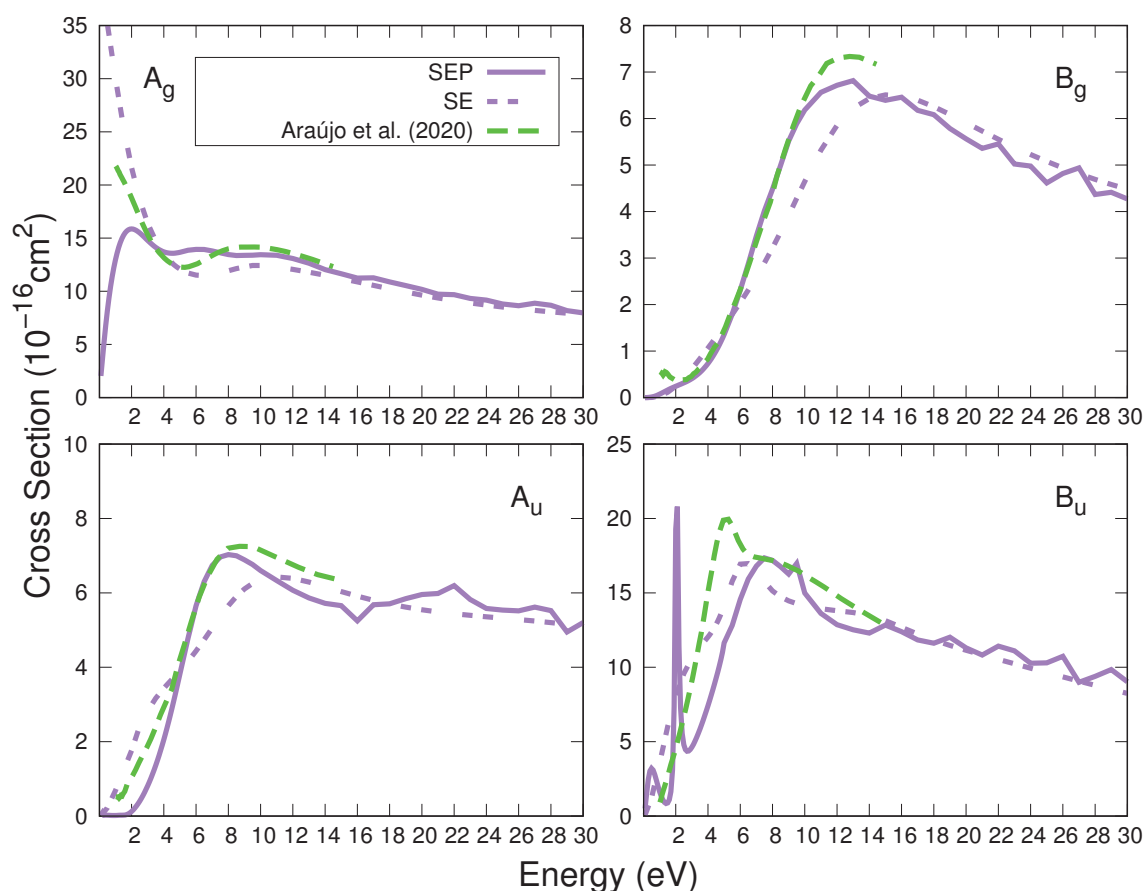


Figure B.3 – Symmetry decomposition of the ICS for the electron scattering by DMP. For both panels: full purple line, SEP results; double-dotted purple line, SE results; dashed green line, results from Araujo *et al.* [134].

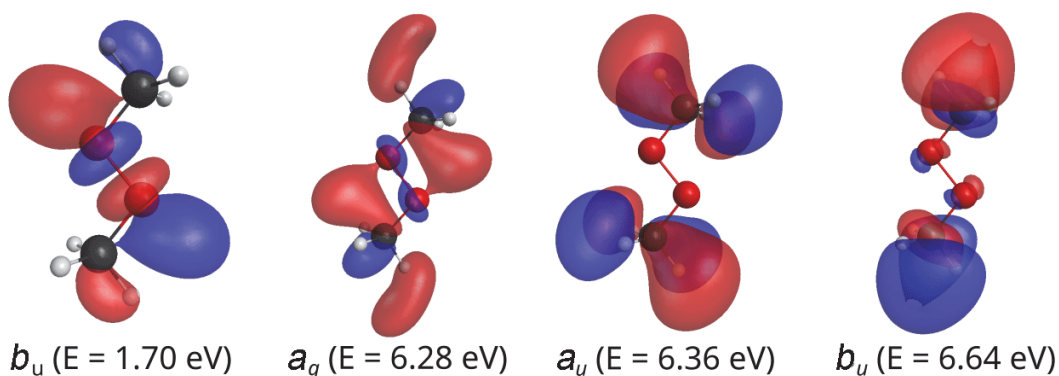


Figure B.4 – Resonant orbitals obtained from the diagonalization of the scattering Hamiltonian in the CSF space used in the SEP calculation for DMP.

is seen in the cross section, nor a resonant eigenstate of the scattering Hamiltonian or a signature in the eigenphase sum are observed. For the A_g and A_u symmetries the predominance of the $\ell = 2$ and $\ell = 3$ partial waves, respectively, together with the presence of resonant eigenstates of the scattering Hamiltonian around the peaks in the cross sections lead to the resonance assignment, although the resonance signature in the eigenphase sum of these symmetries is most likely suppressed by the background

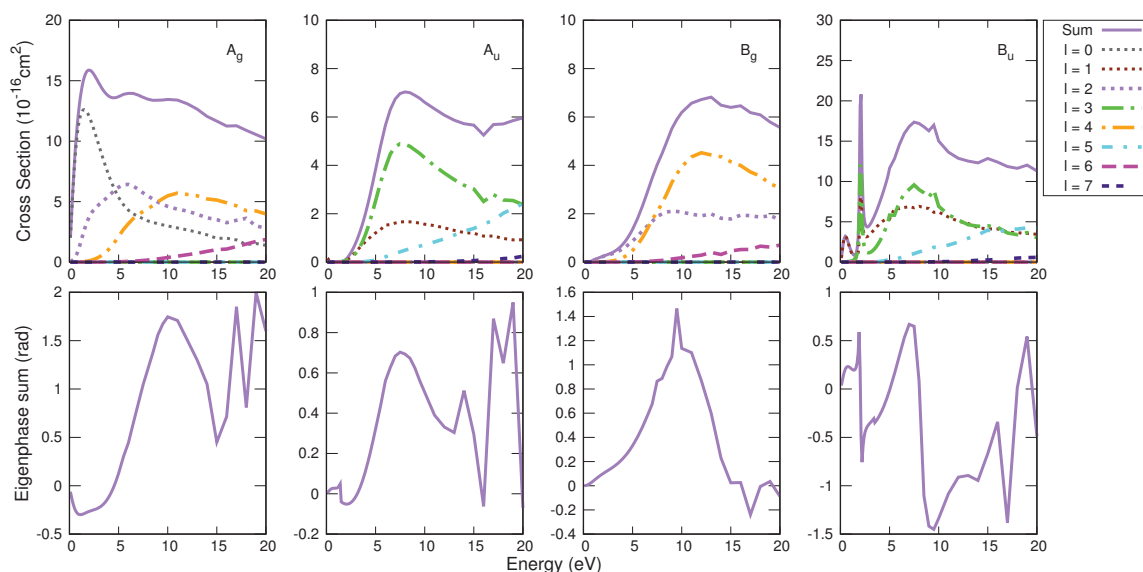


Figure B.5 – Upper row: partial wave decomposition of the SEP ICS for DMP. Only the partial waves with a relevant contribution are shown. Lower row: eigenphase sum.

scattering and the broad width of the structures. Another interesting observation is the effect of pseudoresonances in the eigenphase sum, that lead to the ill behaviour in the high-energy regime (Fig. B.5).

Once again, the comparison between the present symmetry decomposition of the SEP ICS and the one performed by Araújo *et al.* [134] is overall good (Fig. B.3). The main differences arise in the low-energy behaviour of the A_g cross section and the position of the resonant structures of B_u symmetry due to distinct polarization schemes used in each calculation. Although our results corroborate with the assignment of Araújo *et al.* [134] regarding the O-O character of the low-energy resonance of B_u symmetry, we disagree with their characterization of the high energy structure. According to the authors, the high-energy structure that appear in the ICS is due purely to the continuum arising from the B_g cross section, while our results indicate that in addition to the B_g background, three resonances of A_g , A_u and B_u symmetry also contribute to the structure that appears in the ICS, as discussed in the previous paragraph. Further independent theoretical work needs to be done in order to investigate this structure to a greater extend.

The DCSs calculated at both SE and SEP approximations and the DCSs from Araújo *et al.* [134] are shown in Fig. B.6 for impact energies of 5, 9, 10, 15, 20 and 30 eV. Our DCSs calculated at 9 and 10 eV present two minima, indicating the prevalence of the d -wave in the scattering process. However, since these are higher impact energies other partial waves with a higher angular momentum also participate in the scattering process. At 5.0 eV a good qualitative agreement is found between our SE DCS and the one from Araújo *et al.* [134], while an excellent qualitative and quantitative agreement is

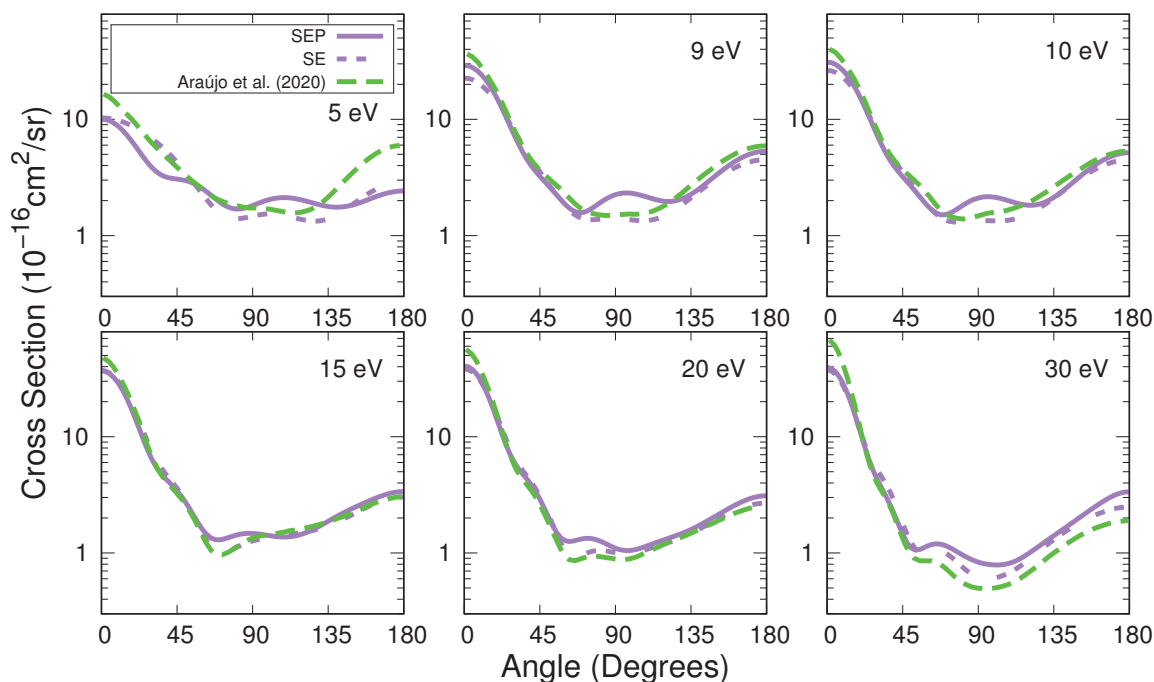


Figure B.6 – DCSs for the electron scattering by DMP for selected energies. Full purple line, SEP results; double-dotted purple line, SE results; dashed green line, results from Araujo *et al.* [134].

found at higher energies.

B.3 Ethylene Glycol

The ICS calculated within the SE and SEP approximations for ETG are presented in the upper panel of Fig. B.7, along with the results from Araujo *et al.* [134]. In the SE approximation the cross section presents a broad structure around 14 eV and a valley at 7 eV. Due to the inclusion of polarization effects in the SEP approximation this broad structure shifts towards lower energies to around 9.1 eV, as expected. The behaviour of the cross section at lower energies also changes dramatically from the SE to the SEP approximation. In the former the ICS exhibits a considerably high magnitude while in the latter the cross section diminishes abruptly as the energy tends to zero due to an angular momentum barrier effect, as will be seen latter. At higher impact energies pseudoresonances can be seen in the SEP ICS due to channels included in the configuration space that are energetically accessible but treated as closed in the elastic approximation. The MTCS calculated at both approximations is presented in the lower panel of Fig. B.7 and is qualitatively analogous to the ICS. The low energy structure that appear in the SEP MTCS is due to an angular momentum barrier effect.

An overall good agreement between the present calculations and the results from Araujo *et al.* [134] is found (Fig. B.7). Once again, the main differences can be

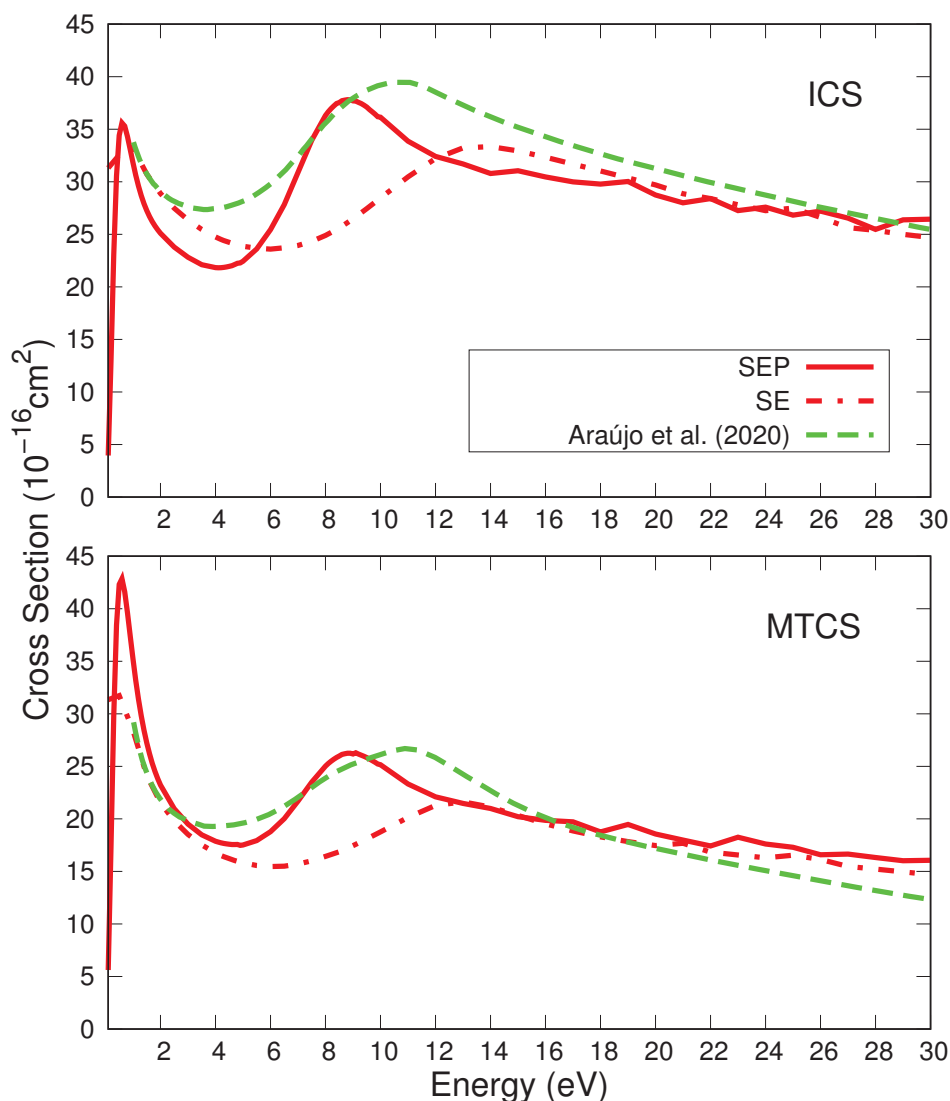


Figure B.7 – Upper panel: ICS for the electrons scattering by ETG. Lower panel: MTCS for the electron scattering by ETG. For both panels: full red line, SEP results; dash-dot red line, SE results; dashed green line, results from Araújo *et al.* [134].

seen in the low-energy regime due to the distinct treatment of the polarization effects in each calculation. The structure reported by Araújo *et al.* [134] is broader and centered at slightly higher energies than the one found in the present SEP calculation, and at lower energies than the one found in the SE results. Since Araújo *et al.* [134] performed their calculation for energies above 1 eV the angular momentum barrier effect was not observed in their results. The comparison between the present MTCSs and the one from Araújo *et al.* [134] is analogous to the ICSs comparison.

As was done for DMP, to further assess the origin of the structures that appear in the ICSs, we performed a symmetry decomposition of the cross sections allied to the diagonalization of the scattering Hamiltonian in the CSF space of the SEP calculation.

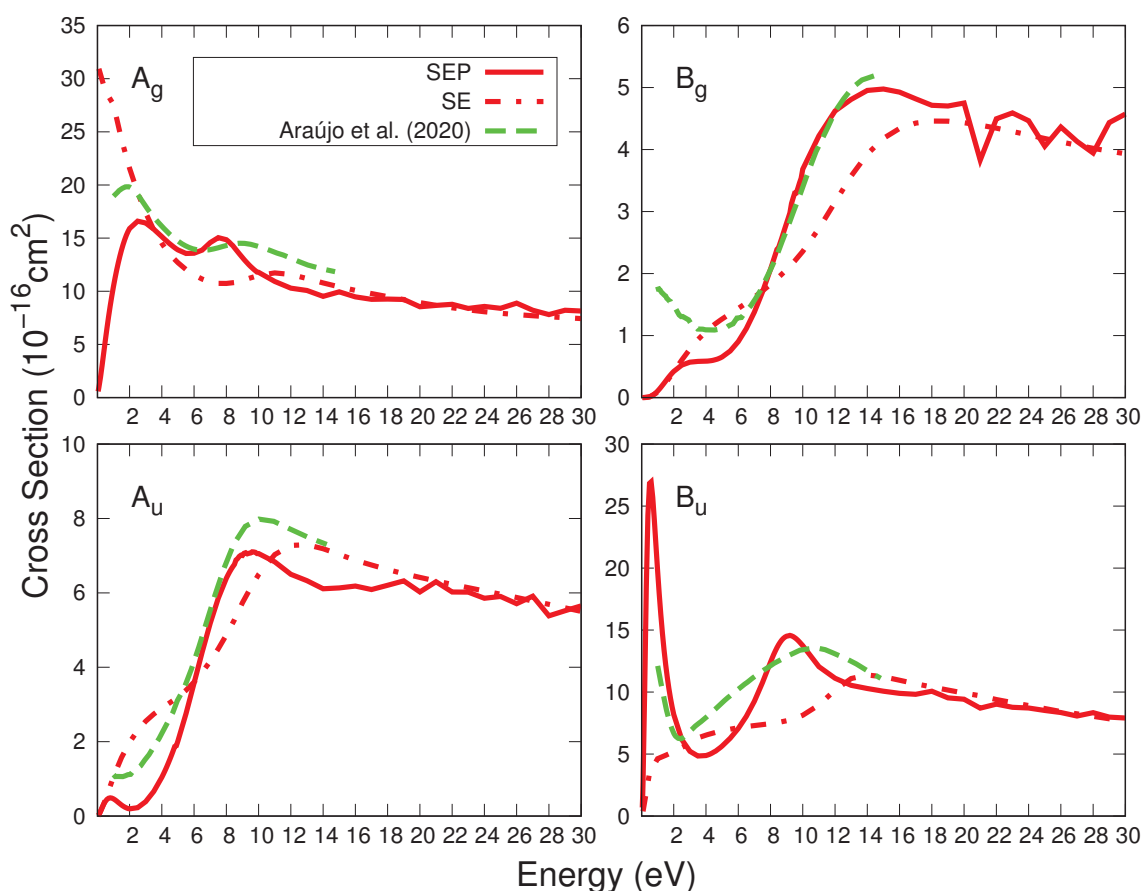


Figure B.8 – Symmetry decomposition of the ICS for the electron scattering by ETG. For both panels: full red line, SEP results; dash-dot red line, SE results; dashed green line, results from Araujo *et al.* [134].

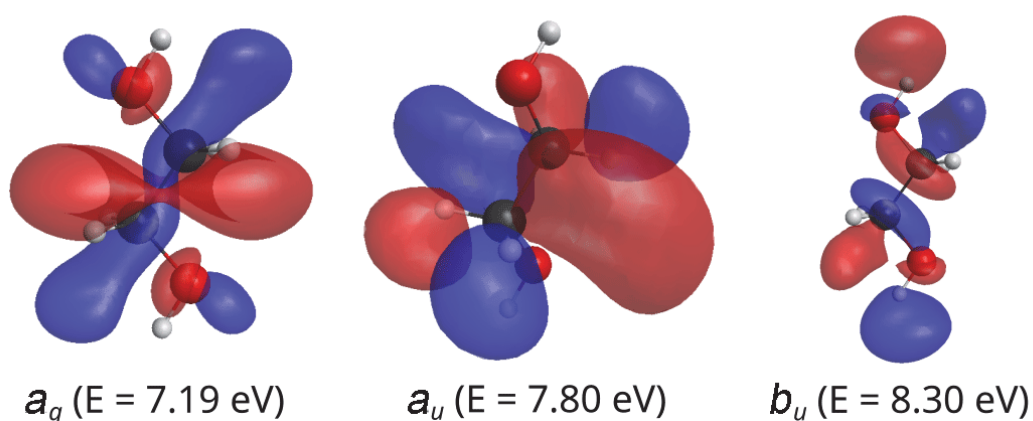


Figure B.9 – Resonant orbitals obtained from the diagonalization of the scattering Hamiltonian in the CSF space used in the SEP calculation for ETG.

The symmetry decomposition of the ICSs are present in Fig. B.8 alongside the results from Araujo *et al.* [134], while the resonant orbitals generated from the H_{N+1} eigenstates are depicted in Fig. B.9. Since the low-energy (below 1 eV) structures that appear in the A_u and B_u SEP cross sections do not have a corresponding structure in the SE

approximation they are assigned to an angular momentum barrier effect, which gives rise to the intense low-energy structure observed in the SEP ICS. As is the case for DMP, our calculation shows that the wide structure that appear in the high-energy regime of the SEP ICS is a superposition of resonances of A_g , A_u and B_u symmetry. The A_g resonance is seen as a small structure centered at 7.5 eV in the cross section. The diagonalization of the H_{N+1} indicates a state of A_g symmetry with eigenvalue of 7.19 eV where the corresponding resonant orbital is located at the C-O and C-H bonds of the molecule. The A_u resonance is a broad Lorentzian-profiled structure mixed with the background scattering (especially at higher impact energies) centered at 9.6 eV in the cross section and the H_{N+1} eigenvalue associated with this resonant state is 7.80 eV. The main contribution to the resonant orbital of a_u symmetry comes from the C and H atoms, with no component in the oxygen atoms. The B_u resonance is centered at 9.2 eV in the cross section and its corresponding H_{N+1} eigenstate has an eigenvalue of 8.30 eV. This resonant orbital is localized in the hydrogen atoms, with a non-bonding σ^* C-C component.

The partial wave decomposition of the ICS of each symmetry of ETG and the eigenphase sums are presented in Fig. B.10. In contrast to DMP, all three resonances of A_g , A_u and B_u symmetries of ETG leave signatures (jumps) in the eigenphase sum. Additionally, the A_g resonance presents a dominance of the d -wave ($\ell = 2$) scattering, while the A_u resonance has a f -wave ($\ell = 3$) dominance. The B_u resonance is mainly due to the $\ell = 3$ partial wave scattering, although the $\ell = 1$ partial wave also has a relevant contribution around the resonance energy. Interestingly, note that these are the same dominant partial waves of the higher lying resonances of DMP in each respective

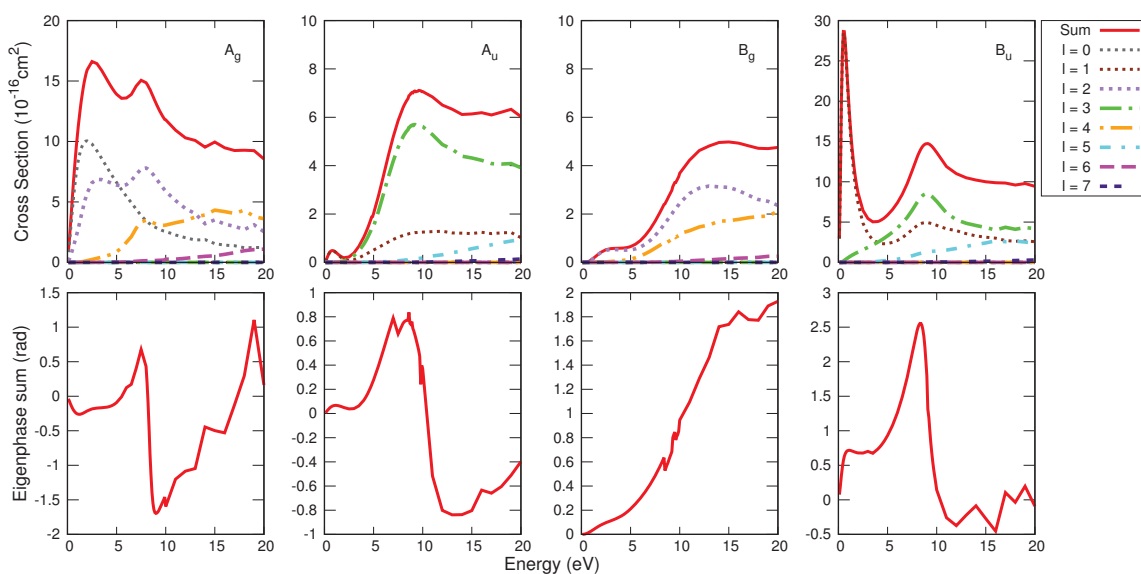


Figure B.10 – Upper row: partial wave decomposition of the SEP ICS for ETG. Only the partial waves with a relevant contribution are shown. Lower row: eigenphase sum.

Table B.2 – Resonances positions for DMP and ETG obtained at the SE and SEP levels of approximation and energy eigenvalues of the resonant states of the scattering Hamiltonian (H_{N+1}). Results from Araújo *et al.* [134] are also shown for comparison. All values are in eV.

Molecule	Symmetry	SE	SEP	H_{N+1}	Ref. [134]
DMP	A_g	10.0	6.0	6.28	-
	A_u	11.0	8.0	6.36	-
	B_u	6.5, 13.0	2.1, 7.5	1.70, 6.64	5, -
ETG	A_g	11.0	7.5	7.19	10
	A_u	13.0	9.5	7.80	-
	B_u	14.0	9.2	8.30	10

symmetry. As is the case for DMP no evidence supports a resonance of B_g symmetry.

Once again, the agreement between the SEP cross sections and the ones from Araújo *et al.* [134] is good (Fig. B.8). The main differences are the position and width of the B_u resonance that, one more time, is a result of the distinct treatment of the polarization effects in the scattering calculations. According to Araújo *et al.* [134] the structure that appears in the ICS is a superposition of resonances of A_u and B_u symmetries. In contrast, our calculation shows an additional A_g resonance besides the two A_u and B_u resonances seen by Araújo *et al.* [134]. In Tab. B.2 a summary of the position of the resonances found for both DMP and ETG is given.

The DCSs at impact energies of 5, 9, 10, 15, 20 and 30 eV calculated at both SE

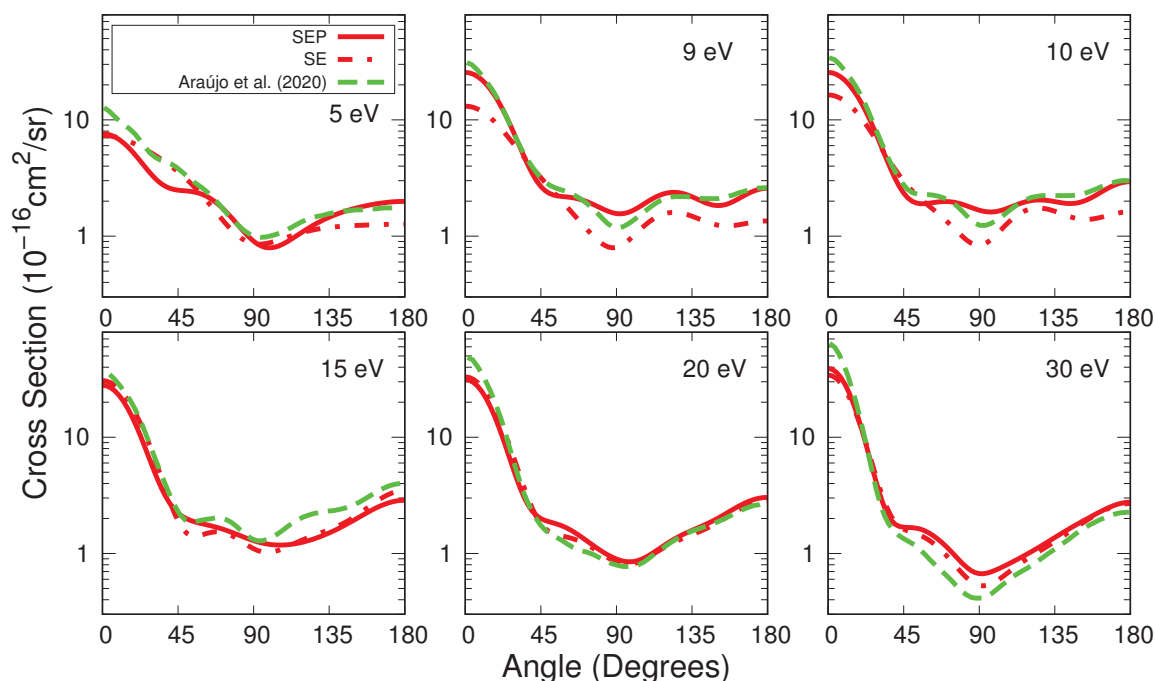


Figure B.11 – DCSs for the electron scattering by ETG for selected energies. Full red line, SEP results; dash-dot red line, SE results; dashed green line, results from Araújo *et al.* [134].

and SEP approximations and the ones from Araújo *et al.* [134] are presented in Fig. B.11. For energies below 15 eV a good agreement between the oscillatory behaviour of the SEP DCSs and the ones from Araújo *et al.* [134] is observed, while at higher energies the SE DCSs are in better agreement with the results from Araújo *et al.* [134]. The small discrepancies between the SEP DCSs and the ones from Araújo *et al.* [134] may be a consequence of the different polarization strategies used in the calculations and the pseudoresonances that appear in the high energy regime of the SEP ICS. At 9, 10 and 15 eV three minima in the SEP DCSs are observed, indicating the predominance of the f -wave scattering. Once again it is important to note that these are relatively high-impact energies. Thus, more than one partial wave are relevant for the scattering process.

B.4 Comparison

In Fig. B.12 we present the comparison between the ICSs of DMP and ETG calculated in the SE and SEP approximations. In the SE approximation the magnitude of the cross section of DMP is bigger than the cross section of ETG over the entire range of energies considered here. However, the difference is much more significant in the low-energy regime and, as the energy of the incident electron increases, the cross sections for DMP and ETG become similar, depicting a clear example of the isomerization effect in the cross sections. As discussed before, this is a consequence of the relation between the de Broglie wavelength of the incident electron and the molecular size. In the low-energy regime, the de Broglie wavelength of the incident electron is comparable to the size of the target molecule and, as a consequence, small changes in its structure become apparent to the projectile. For higher impact energies the de Broglie wavelength decreases, and the details of the molecular structure are not distinguishable to the incident electron anymore, leading to similar cross sections. In addition, the presence of the low-energy resonance in the case of DMP further enhances the differences between the ICS of DMP and ETG in the low-energy regime.

As the polarization effects are included in the scattering calculations the difference between the cross sections of the two molecules increases, specially at lower energies, as can be seen in Fig. B.12. This discrepancy is mainly due to the narrow B_u resonance of DMP and to the intense angular momentum barrier effect in the ETG cross section. This effect makes the cross section for ETG larger than the cross section for DMP for energies below 4 eV, except near to the resonance in the DMP ICS. For energies higher than 4 eV the cross section of DMP is bigger than the cross section of ETG. As is expected for isomers, the SEP ICS for both molecules become similar as the incident electron energy increases. The SEP ICS curves indicate that only DMP

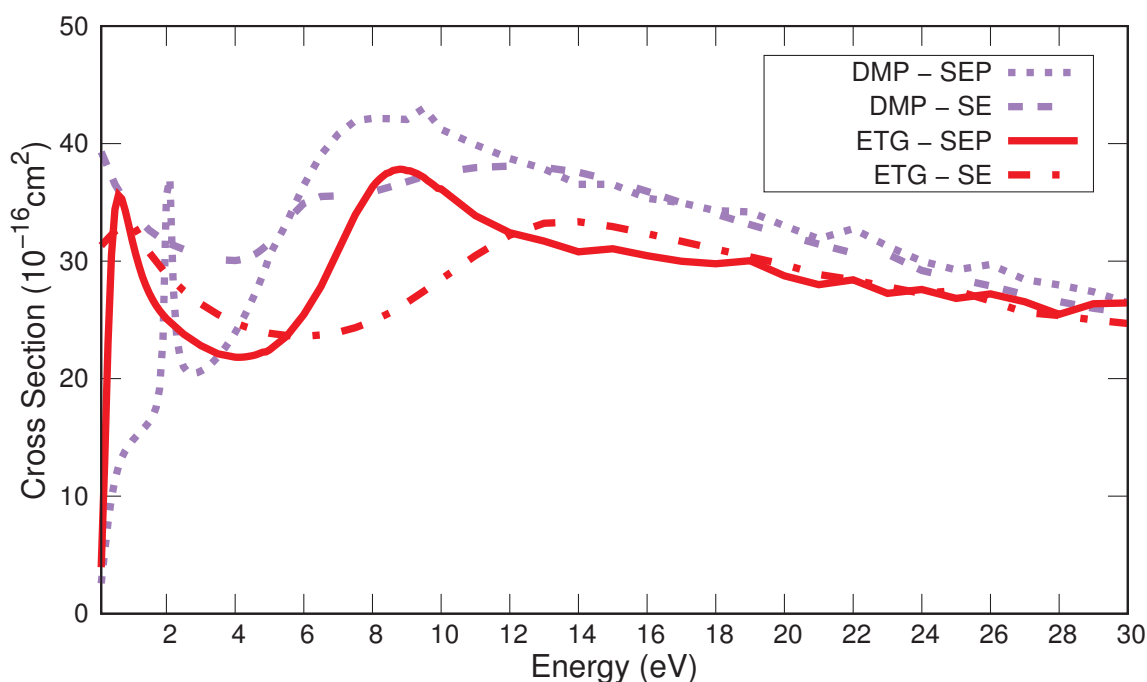


Figure B.12 – ICSs for electron scattering by DMP and ETG. Dotted purple line, SEP DMP; double-dotted purple line, SE DMP; full red line, SEP ETG; and dash-dot red line, SE ETG.

has a low-energy resonance, while both molecules have the high-energy large resonant structure. This is expected, since ETG do not have a O-O bond and therefore structurally cannot support the low-energy resonance associated with the O-O bond in DMP.

The cross section for the resonant symmetries and the resonant orbitals associated with the high-energy broad resonances of both molecules are presented in Fig. B.13. The three resonances of ETG are located at slightly higher energies as compared to the three resonances of DMP. This can also be seen in Tab. B.2. The character of two of these resonances presents similarities in both molecules: the A_g resonance has a σ^* character located in the C-O and C-H bonds, and the A_u resonance has a σ^* character and is located along the H atoms. Furthermore, even though the B_u resonance for ETG has a C-C component, which would be impossible for DMP due to the absence of a C-C bond, the resonant orbitals for DMP and ETG are similar in the sense that both of them are located at the hydrogen and carbon atoms of the molecule.

The DCSs for DMP and ETG are compared in Fig. B.14 and basically all comments performed in the analysis of the ICS results apply here too. Strictly speaking, the differences (both in magnitude and oscillatory pattern) in the DCSs for DMP and ETG are meaningful in the low-energy regime, while for higher energies the cross sections behave in a similar way. As mentioned before, this can be understood by comparing the de Broglie wavelength of the incident electron and the molecular size, quantities which

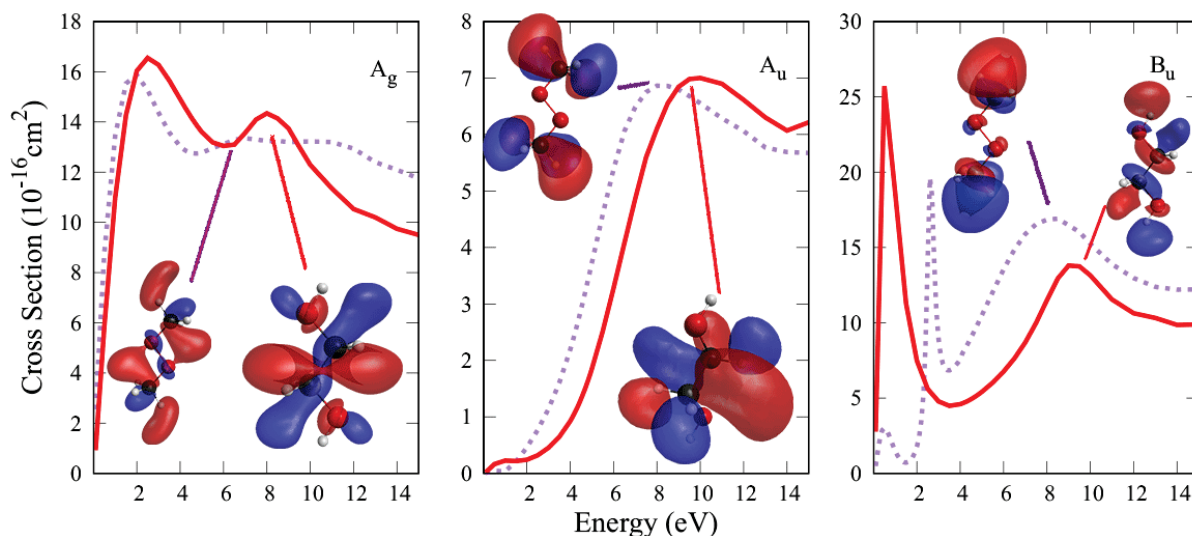


Figure B.13 – Symmetry decomposition of the ICS of DMP and ETG. Only the resonant symmetries in the SEP approximation are presented. Dotted purple line, SEP DMP; and full red line, SEP ETG.

are similar in the low-energy regime and distinct for higher impact energies. Thus, the isomerization effect is also reflected in the DCSs. Another interesting feature is that, in the region around the high-energy broad resonance, the SEP DCSs of both molecules display a different oscillatory behaviour, with two and three minima present in the DCSs for DMP and ETG, respectively.

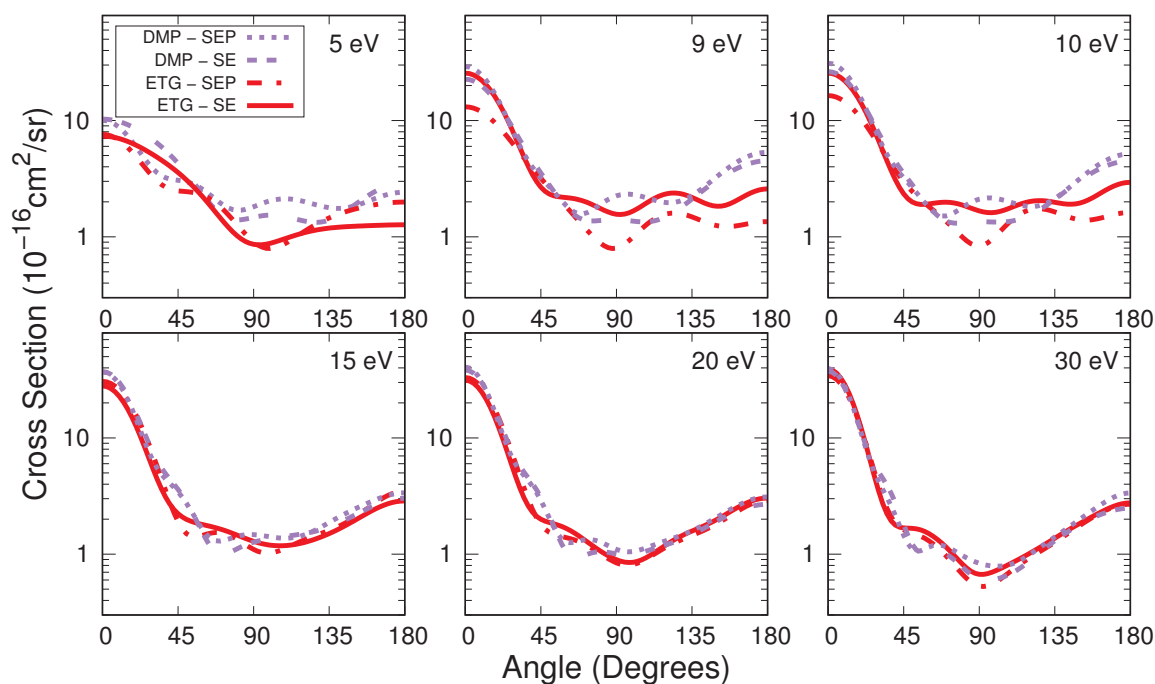


Figure B.14 – DCS for the electron scattering by DMP and ETG. Dotted purple line, SEP DMP; double-dotted purple line, SE DMP; full red line, SEP ETG; and dash-dot red line, SE ETG.

B.5 Conclusion

In this appendix the elastic electrons scattering cross sections for both DMP and ETG were presented. These cross sections were calculated with the SMCPP method in both the SE and SEP approximations. For DMP a narrow resonance of B_u symmetry was characterized as a σ^* resonance along the O-O bond around 2.1 eV. While this low-lying resonance was also seen in the results from Araújo *et al.* [134], we identify three additional large shape resonances of A_g , A_u and B_u symmetry at higher impact energies that were not reported by the authors for this molecule. For ETG only a higher-lying structure was found in the ICS, which according to our results is a superposition of three shape resonances of A_g , A_u and B_u symmetry. This was also observed by Araújo *et al.* [134], however the authors only attributed contributions from A_u and B_u resonances in their calculations. When comparing the cross sections of both isomers, we found that the most striking differences are observed in the low-energy regime, while for higher impact energies the cross sections are similar, as expected.

APPENDIX C

Additional theoretical details

C.1 The Born-closure procedure

In the SMC method, the scattering wave function is expanded using a basis set comprised of CG functions that are square integral functions. As previously mentioned, this approach provides computational advantages because the integrals required to calculate the scattering amplitude (as given in equation (2.53)) become analytical in this basis set. However, while these functions are effective in describing close-ranged interactions between the incident electron and the molecular target, they are not suitable for representing the long-ranged interactions. Therefore, when applied to polar molecules, the SMC method falls short in its ability to accurately capture the long-ranged dipole interactions that are involved in the scattering process. In the elastic channel these interactions are especially important for low impact energies and small scattering angles.

To rectify this problem, the Born-closure procedure is employed [78]. The main idea is that the long-ranged dipole interactions are described within the first Born approximation (FBA) for the scattering of an electron by the permanent dipole of the molecule, while the SMC method remains describing the close-range interactions. In the FBA, the scattering amplitude for the scattering of an electron by a electric dipole moment is given as

$$f^{\text{FBA}}(\vec{k}_f, \vec{k}_i) = 2i \frac{\vec{D} \cdot (\vec{k}_i - \vec{k}_f)}{|\vec{k}_i - \vec{k}_f|^2} \quad (\text{C.1})$$

where \vec{D} is the permanent dipole moment of the incident molecular target and $\vec{k}_{i,f}$

are the initial and final linear momenta of the incident electron. Then, the amplitudes calculated using the first Born approximation (f^{FBA}) and the SMC method (f^{SMC}) are expanded in terms of spherical harmonics and the final scattering amplitude is given by

$$f(\vec{k}_f, \vec{k}_i) = f^{FBA}(\vec{k}_f, \vec{k}_i) + \sum_{l=0}^{l_{SMC}} \sum_{m=-l}^l [f_{lm}^{SMC}(k_f, \vec{k}_i) - f_{lm}^{FBA}(k_f, \vec{k}_i)] Y_l^m(\hat{k}_f), \quad (C.2)$$

where f_{lm} are the expansion coefficients of the respective amplitudes in the spherical harmonics basis set and l_{SMC} is a angular momentum cut-off that will be discussed in the next paragraph. With this procedure, the information about the long-ranged scattering are better described in the calculations, enabling the study of interactions between electrons and polar molecules.

Upon closer inspection of equation (C.2), we can observe that for partial waves with angular momentum l below a certain threshold given by l_{SMC} the scattering amplitudes obtained through the SMC method are used. For partial waves with higher angular momentum ($l > l_{SMC}$), the scattering amplitudes obtained with the first Born approximation are used. The reasoning behind this can be understood through a semi-classical picture of the scattering problem.

Consider the scattering of a particle by a solid sphere of radius R . The incident particle hits the sphere with an impact parameter b and is scattered at an angle θ , as illustrated in Figure C.1. As the impact parameter increases, the scattering angle decreases. Now, consider that the magnitude of the angular momentum L can be written as

$$L = rp \sin \gamma \quad (C.3)$$

where r and p are the magnitudes of the position and linear momentum vectors, respectively, and γ is the angle between them. From Figure C.1, one may find that $b = r \sin \gamma$, such that

$$L = bp. \quad (C.4)$$

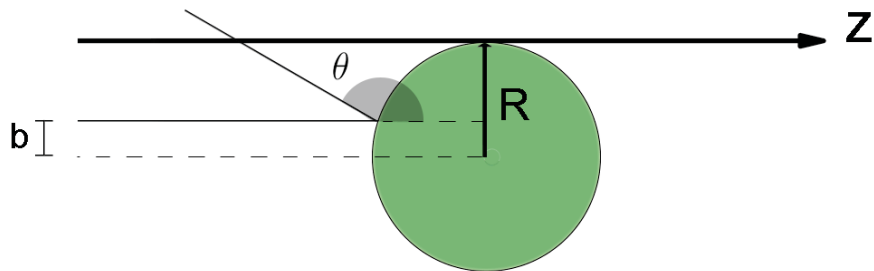


Figure C.1 – Representation of the scattering of a particle by a rigid sphere of radius R . The incident particle has an impact parameter b and is scattered in the direction defined by the angle θ .

Now, using the quantization rules for the angular momentum ($\sqrt{l(l+1)}\hbar$) and for the linear momentum ($k\hbar$) we obtain

$$b = \frac{\sqrt{l(l+1)}\hbar}{k\hbar} \sim \frac{l}{k} \quad (\text{C.5})$$

such that, as the impact parameter increases, the angular momentum quantum number l also increases. That is, as the particle is scattered by a long-ranged potential (high b), partial waves with a higher angular momentum are relevant in the scattering process (high l).

C.2 Pseudopotentials

One of the difficulties found in calculating the scattering amplitude given in equation (2.53) is that for a molecule with a large number of electrons an increasingly larger basis set is necessary to properly describe the scattering process. As a consequence, the number of two-electron integrals that have to be evaluated for each pair of electrons increase rapidly, making the calculation computationally unfeasible.

Since our main interest is in the scattering of low-energy electrons (< 50 eV) by molecules, the incident electron interacts more intensely with the valence electrons of the target, while the core electrons and the nuclei do not influence the scattering in a relevant way. Therefore, one efficient way of overcoming the problem presented in the previous paragraph is to represent the core electrons and the nuclei of the molecule by pseudopotentials, while the valence electrons are explicitly represented by molecular orbitals. In such manner, we reduce the number of basis functions necessary to describe the molecule, while maintaining a good description of the scattering process itself.

In the SMC method, norm-conserving pseudopotentials of Bachelet, Hamann and Schlüter (BHS) [86] are used to represent the core electrons and the nuclei of the molecule. These pseudopotentials have the form

$$\hat{V}_{PP} = \hat{V}_{\text{Ion}} + \hat{V}_{\text{Nuc}} \quad (\text{C.6})$$

where

$$\hat{V}_{\text{Nuc}} = -\frac{Z_v}{r} \sum_{i=1}^2 c_i \text{erf}[r\sqrt{\rho_i}] \quad (\text{C.7})$$

and

$$\hat{V}_{\text{Ion}} = \sum_{n=0}^1 \sum_{\ell=0}^2 \sum_{j=1}^3 A_{nj\ell} r^{2n} e^{-\sigma_{j\ell} r^2} \sum_{m=-\ell}^{+\ell} |\ell m\rangle \langle \ell m| \quad (\text{C.8})$$

where the parameters $A_{nj\ell}$, $\sigma_{j\ell}$, c_i and ρ_i are given in Ref. [86]. The implementation of these pseudopotentials was done by Bettega *et al.* [87], and the method itself is now

denominated by Schwinger Multichannel Method implemented with pseudopotentials (SMCPP). This version of the method was used in all calculations presented in this work.

C.3 Frame transformation

The scattering amplitude given in equation (2.53) is calculated in the reference frame of the molecule, also called body-frame. In this way the symmetries of the molecular target can be exploited in order to lower the computational cost of the scattering calculations. However, to provide a comparable result to the one found experimentally it is necessary to perform a transformation of the scattering amplitude from the body-frame to the laboratory-frame. This is done through a rotation from the coordinates of the body-frame (x, y, z) to the coordinates of the laboratory-frame (x', y', z') , where the axis z' is chosen to be in the same direction of the incident electron \vec{k}_i . To achieve this, Wigner rotation matrices $D_{m,m'}^{(l)}(\phi_i, \theta_i, 0)$ [135], where ϕ_i and θ_i are the azimuthal and polar angles associated with axis z , that rotate spherical harmonics as

$$Y_l^{m'}(\hat{k}_f) = \sum_m D_{m,m'}^{(l)}(\phi_i, \theta_i, 0) Y_l^m(\hat{k}_f), \quad (\text{C.9})$$

are used.

Firstly, the body-frame scattering amplitude (f^B) is expanded in spherical harmonics as

$$f^B(\vec{k}_f, \vec{k}_i) = \sum_{l=0}^{l_{max}} \sum_{m=-l}^l f_{lm}(\hat{k}_f, \vec{k}_i) Y_l^m(\hat{k}_f) \quad (\text{C.10})$$

where the coefficients $f_{lm}(\hat{k}_f, \vec{k}_i)$ are

$$f_{lm}(\hat{k}_f, \vec{k}_i) = \int d\hat{k}_f Y_l^{m*}(\hat{k}_f) f^B(\vec{k}_f, \vec{k}_i). \quad (\text{C.11})$$

Then, the the inverse of equation (C.9) is used in expression (C.10), such that the scattering amplitude written in the laboratory-frame (f^L) is

$$f^L(\vec{k}'_f, \vec{k}_i) = \sum_{l,m,m'} f_{lm}(\hat{k}_f, \vec{k}_i) D_{m,m'}^{(l)*}(\phi_i, \theta_i, 0) Y_l^{m'}(\hat{k}'_f). \quad (\text{C.12})$$

From the scattering amplitude written in the laboratory-frame the differential cross sections is calculated as

$$\frac{d\sigma}{d\Omega}(\theta_f, \phi_f; k_i, k_f) = \frac{1}{4\pi} \frac{k_f}{k_i} \int d\hat{k}_i |f^L(\vec{k}'_f, \vec{k}_i)|^2 \quad (\text{C.13})$$

where θ_f and ϕ_f are defined in respect to the laboratory-frame. The integration with respect to \hat{k}_i is done to account for all possible directions of the incident beam, which is

equivalent of account for all different orientation of the molecule in the experimental gas. Thus, the cross sections calculated through equation (C.13) are directly comparable to the experimental measurements.

C.4 Example of the MOB-SCI procedure

In chapter 2 the MOB-SCI procedure was presented and discussed. This is the procedure used to obtain the electronically excited states were be used in the scattering calculations performed with the SMCPP method. Briefly, the MOB-SCI procedure consists of three steps: (i) generating a set of IVOS, (ii) performing a FSCI calculation and (iii) selecting the relevant Slater determinants from the FSCI results to perform the MOB-SCI calculation. Although this is a direct pathway to obtain the electronically excited states, it involves many tests and considerations along the way, which makes it not as straightforward as one may think. Thus, to illustrate the MOB-SCI procedure more explicitly, in this appendix we shall walk the path to obtain the electronically excited states of methane used in the calculations presented in chapter 4.

The first step is to obtain a set of IVOs to perform the calculations. The electronic configuration of methane's ground state according to the C_{2v} point group is $(core)^2(1a_1)^2(2a_1)^2(1b_1)^2(1b_2)^2$, where the three highest molecular orbitals are degenerated (t_2 symmetry). Thus, the IVOs must be generated using the first valence orbital $1a_1$ in order to preserve degeneracy.

The second step is to perform FSCI calculations to determine which basis set is the most cost effective to perform the subsequent scattering calculations. In this step we perform different FSCI calculations varying the basis set used in each atom or extra center. Evidently, for each basis set a new set of IVOs must be generated. Some of the tests that we perform for methane are presented in table C.1. In this table we present the results obtained from the more robust EOM-CCSD/aug-cc-pVDZ calculation, results from an FSCI/aug-cc-pVDZ all-electron calculation ($FSCI_{all-e}$) and from FSCI calculations performed with pseudopotentials and a different number of extra centers and basis sets. In the table, the number of Cartesian Gaussian (CG) functions used in the central carbon atom is presented followed by the number of CGs used in the extra centers. For instance, the $FSCI_{ce_3}$ calculation used $6s$, $4p$ and $3d$ CG functions in the carbon atom and $3s$, $3p$ and $2d$ CG functions on the extra centers. Calculation $FSCI_{ce_1}$, $FSCI_{ce_2}$ and $FSCI_{ce_3}$ used 4 extra centers that together with the hydrogen atoms form a cube around the central carbon atom. Calculations $FSCI_{ce_4}$ and $FSCI_{ce_5}$ used not only this 4 extra centers, but also 8 additional extra centers that form a larger cube around the methane molecule itself. These extra centers distributions are presented in Fig. C.2. As a precaution, the electronically excited states depicted in table C.1 are

Table C.1 – Vertical excitation energy of the electronically excited states of methane. See text for a detailed discussion.

Estado	EOMCCSD	FSCI _{all-e}	FSCI ₆₅₃	FSCI _{ce1}	FSCI _{ce2}	FSCI _{ce3}	FSCI _{ce4}	FSCI _{ce5}
T_d C_{2v}	aug-cc-pVDZ	aug-cc-pVDZ	653	643+3	643+33	643+332	643+3+3	643+33+33
1^3A_1	10.163	10.344	10.396	10.409	10.334	10.329	10.370	10.321
1^3T_2 1^3B_1	10.163	10.344	10.396	10.409	10.334	10.329	10.370	10.321
1^3B_2	10.163	10.344	10.396	10.409	10.334	10.329	10.370	10.321
1^1A_1	10.566	11.082	11.154	11.171	11.102	11.101	11.145	11.096
1^1T_2 1^1B_1	10.566	11.082	11.154	11.171	11.102	11.101	11.145	11.096
1^1B_2	10.566	11.082	11.154	11.171	11.102	11.101	11.145	11.096
1^3A_1 2^3A_1	11.133	11.090	11.443	11.519	11.051	11.042	11.277	11.009
3^3A_1	11.732	12.243	12.696	12.731	12.211	12.207	12.540	12.191
2^3T_2 2^3B_1	11.732	12.243	12.696	12.731	12.211	12.207	12.540	12.191
2^3B_2	11.732	12.243	12.696	12.731	12.211	12.207	12.540	12.191
2^1A_1	11.852	12.439	13.323	13.836	12.370	12.369	13.381	12.357
2^1T_2 2^1B_1	11.852	12.439	13.323	13.836	12.370	12.369	13.381	12.357
2^1B_2	11.852	12.439	13.323	13.836	12.370	12.369	13.381	12.357
1^3E 5^3A_1	11.882	12.420	13.307	13.974	12.262	12.255	13.501	12.246
1^3A_2	11.882	12.420	13.307	13.974	12.262	12.255	13.501	12.246
1^1E 3^1A_1	11.962	12.554	13.555	14.220	12.354	12.350	13.686	12.340
1^1A_2	11.962	12.554	13.555	14.220	12.354	12.350	13.686	12.340
2^1A_2	11.998	12.597	13.618	14.158	12.373	12.368	13.706	12.358
1^1T_1 3^1B_1	11.998	12.597	13.618	14.158	12.373	12.368	13.706	12.358
3^1B_2	11.998	12.597	13.618	14.158	12.373	12.368	13.706	12.358
2^3A_2	12.006	12.594	13.452	13.745	12.345	12.334	13.452	12.321
1^3T_1 4^3B_1	12.006	12.594	13.452	13.745	12.345	12.334	13.452	12.321
4^3B_2	12.006	12.594	13.452	13.745	12.345	12.334	13.452	12.321
2^3A_1 4^3A_1	12.201	12.926	13.291	13.893	12.598	12.593	13.458	12.563
6^3A_1	12.663	12.969	13.400	13.794	12.560	12.547	13.524	12.511
3^3T_2 3^3B_1	12.663	12.969	13.400	13.794	12.560	12.547	13.524	12.511
3^3B_2	12.663	12.969	13.400	13.794	12.560	12.547	13.524	12.511
7^3A_1	13.673	13.246	13.553	14.240	13.277	13.270	13.788	13.233
4^3T_2 5^3B_1	13.673	13.246	13.553	14.240	13.277	13.270	13.788	13.233
5^3B_2	13.673	13.246	13.553	14.240	13.277	13.270	13.788	13.233
4^1A_1	13.588	14.258	13.742	14.506	13.128	13.306	13.986	13.248
3^1T_2 4^1B_1	13.588	14.258	13.742	14.506	13.128	13.306	13.986	13.248
4^1B_2	13.588	14.258	13.742	14.506	13.128	13.306	13.986	13.248

presented according to the C_{2v} point group in order to ensure that nothing is wrong with the degeneracy of the excited states that should be degenerated.

From the tests presented in table C.1 (and other tests not shown here), we concluded that the most cost effective basis set and extra centers arrangement to perform the scattering calculations is the FSCI_{ce2} result. With this calculation we were able to reproduce well the results from the EOM-CCSD/aug-cc-pVDZ calculation. Beyond that, the extra d -type function from calculation FSCI_{ce3} and the extra centers from calculations FSCI_{ce4} and FSCI_{ce5} doesn't seem to affect the description of the first few electronically excited states in a relevant way. Thus, the best spectrum obtained with the least computational effort is the one from the FSCI_{ce2} calculation.

The final step of the MOB-SCI procedure is to select the Slater determinants that contribute the most for the description of the first few electronically excited states obtained through the FSCI calculation. As one should expect by now, we also perform

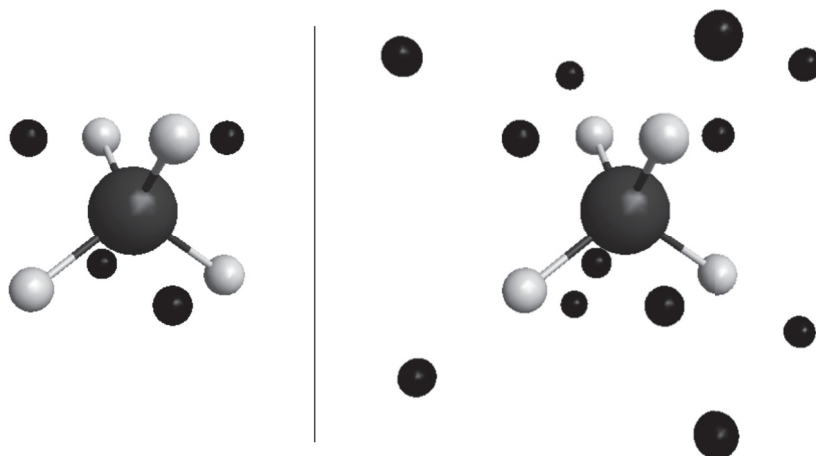


Figure C.2 – Different arrangements of extra centers used in the tests presented in table C.1. The arrangement of the left was used for the $FSCI_{ce_1}$, $FSCI_{ce_2}$ and $FSCI_{ce_3}$ calculations, while the one on the right was used for the $FSCI_{ce_4}$ and $FSCI_{ce_5}$ calculations.

many tests selecting different numbers of Slater determinants to choose the optimal set of Slater determinants that will be used in the following scattering calculations. In the case of methane, some of these tests are presented in table C.2. In the table, for each test, we indicate the number of hole-particle pairs used, the cut-off value used to select the coefficients, and the energy of the highest electronically excited state of interest obtained in the FSCI calculation. For instance, to perform the MOB- SCI_2 calculation we looked at every electronically excited state obtained through the $FSCI_{ce_2}$ calculation whose vertical excitation energy lies below 15 eV. For these excited states, we selected the Slater determinants whose modulus square of the coefficient in the FSCI expansion were larger than 0.2. That is, for a state Γ , $|c_a^{r,\Gamma}|^2 > 0.2$. This procedure leads to 57 Slater determinants being selected from the 416 used in the $FSCI_{ce_2}$ calculation. With these 57 Slater determinants we perform a MOB- SCI calculation, resulting in the vertical excitation energies presented in table C.2.

From our tests the most cost effective set of Slater determinants is the one from the MOB- SCI_5 calculation. For this calculation we looked at every electronically excited state obtained through the $FSCI_{ce_2}$ calculation whose vertical excitation energy is below 20 eV, and selected the Slater determinants whose coefficients modulus squared is larger than 0.05. This procedure selected 90 Slater determinants that were able to reproduce well the $FSCI_{ce_2}$ calculation. Beyond that, this set of Slater determinants would lead to a scattering calculation with 181 open channels, which is computationally feasible, and a CSF space with a number of configurations that is sufficiently large to describe the polarization effects. If the results obtained through the MOB- SCI_2 calculation would be chosen, we would risk not having a large enough CSF space to describe the polarization effects in the scattering calculations. Inversely, if we choose the spectrum obtained with the MOB- SCI_6 calculation, the following scattering calculations

Table C.2 – Vertical excitation energy of methane obtained through the MOB-SCI approach. See text for details.

State		FSCI _{ce2}	MOB-SCI ₁	MOB-SCI ₂	MOB-SCI ₃	MOB-SCI ₄	MOB-SCI₅	MOB-SCI ₆
T _d	C _{2v}	416 pairs	30 pairs	57 pairs	60 pairs	90 pairs	90 pairs	159 pairs
		-	0.2	0.2	0.1	0.1	0.05	0.05
		-	13.5 eV	15.0 eV	15.0 eV	20.0 eV	20.0 eV	30.0 eV
1 ³ T ₂	1 ³ A ₁	10.334	10.587	10.539	10.539	10.535	10.535	10.401
	1 ³ B ₁	10.334	10.587	10.539	10.539	10.535	10.535	10.401
	1 ³ B ₂	10.334	10.587	10.539	10.539	10.535	10.535	10.401
1 ³ A ₁	2 ³ A ₁	11.051	11.578	11.533	11.533	11.532	11.532	11.129
1 ¹ T ₂	1 ¹ A ₁	11.102	11.206	11.200	11.178	11.147	11.147	11.113
	1 ¹ B ₁	11.102	11.206	11.200	11.178	11.147	11.147	11.113
	1 ¹ B ₂	11.102	11.206	11.200	11.178	11.147	11.147	11.113
2 ³ T ₂	3 ³ A ₁	12.211	12.283	12.274	12.271	12.258	12.258	12.240
	2 ³ B ₁	12.211	12.283	12.274	12.271	12.258	12.258	12.240
	2 ³ B ₂	12.211	12.283	12.274	12.271	12.258	12.258	12.240
1 ³ E	5 ³ A ₁	12.262	12.305	12.300	12.300	12.297	12.297	12.273
	1 ³ A ₂	12.262	12.305	12.300	12.300	12.297	12.297	12.273
1 ³ T ₁	2 ³ A ₂	12.345	12.378	12.368	11.178	12.357	12.357	12.350
	3 ³ B ₁	12.345	12.378	12.368	11.178	12.357	12.357	12.350
	3 ³ B ₂	12.345	12.378	12.368	11.178	12.357	12.357	12.350
1 ¹ E	3 ¹ A ₁	12.354	12.401	12.385	12.385	12.381	12.381	12.357
	1 ¹ A ₂	12.354	12.401	12.385	12.385	12.381	12.381	12.357
2 ¹ T ₂	2 ¹ A ₁	12.370	12.456	12.411	12.410	12.404	12.404	12.377
	2 ¹ B ₁	12.370	12.456	12.411	12.410	12.404	12.404	12.377
	2 ¹ B ₂	12.370	12.456	12.411	12.410	12.404	12.404	12.377
1 ¹ T ₁	2 ¹ A ₂	12.373	12.401	12.388	12.388	12.383	12.383	12.374
	3 ¹ B ₁	12.373	12.401	12.388	12.388	12.383	12.383	12.374
	3 ¹ B ₂	12.373	12.401	12.388	12.388	12.383	12.383	12.374
3 ³ T ₂	6 ³ A ₁	12.560	12.753	12.737	12.731	12.672	12.672	12.619
	4 ³ B ₁	12.560	12.753	12.737	12.731	12.672	12.672	12.619
	4 ³ B ₂	12.560	12.753	12.737	12.731	12.672	12.672	12.619
2 ³ A ₁	4 ³ A ₁	12.598	12.870	12.836	12.836	12.824	12.824	12.732
3 ¹ T ₂	4 ¹ A ₁	13.128	13.529	13.357	13.355	13.342	13.342	13.318
	4 ¹ B ₁	13.128	13.529	13.357	13.355	13.342	13.342	13.318
	4 ¹ B ₂	13.128	13.529	13.357	13.355	13.342	13.342	13.318
2 ³ T ₁	3 ³ A ₂	12.937	13.122	13.035	13.035	13.014	13.014	12.973
	5 ³ B ₁	12.937	13.122	13.035	13.035	13.014	13.014	12.973
	5 ³ B ₂	12.937	13.122	13.035	13.035	13.014	13.014	12.973

would have 319 open channels. The benefits from having the extra Slater determinants would not weight out the extra computational cost of these scattering calculations. Thus, the best balance between a good description of the electronically excited states, the number of CSF that would be generated from these Slater determinants in the scattering calculations and the computational cost of the scattering calculations themselves was obtained in the MOB-SCI₅ calculation.

APPENDIX D

Geometry and BEB parameters

In this appendix the optimized geometry and the parameters obtained for the BEB calculations are going to be listed in tables for each molecule. All these results were obtained through the computational package GAMESS [105] at distinct levels of theory.

Dimethyl peroxide:

Table D.1 – Cartesian coordinates of the atoms in the optimized geometry of dimethyl peroxide at the MP2/aug-cc-pVDZ level of theory. All units are in Bohr.

Atom	x	y	z
C	-0.7986904216	-3.2060415691	0.0000000000
C	0.7986904216	3.2060415691	0.0000000000
O	0.8739775702	-1.0956378687	0.0000000000
O	-0.8739775702	1.0956378687	0.0000000000
H	-0.4565418792	4.8617811487	0.0000000000
H	0.4565418792	-4.8617811487	0.0000000000
H	1.9882461298	3.2046240549	1.7084194757
H	-1.9882461298	-3.2046240549	-1.7084194757
H	1.9882461298	3.2046240549	-1.7084194757
H	-1.9882461298	-3.2046240549	1.7084194757

Ethylene glycol:

Table D.2 – Cartesian coordinates of the atoms in the optimized geometry of ethylene glycol at the MP2/aug-cc-pVDZ level of theory. All units are in Bohr.

Atom	x	y	z
C	0.8330818827	1.1686536656	0.0000000000
C	-0.8330818827	-1.1686536656	0.0000000000
O	-0.8470657672	3.3012911283	0.0000000000
O	0.8470657672	-3.3012911283	0.0000000000
H	-0.1641410261	-4.8204149365	0.0000000000
H	0.1641410261	4.8204149365	-0.0000000000
H	-2.0470284578	-1.1546883444	1.6958694810
H	2.0470284578	1.1546883444	-1.6958694810
H	-2.0470284578	-1.1546883444	-1.6958694810
H	2.0470284578	1.1546883444	1.6958694810

Formamide:

Table D.3 – Cartesian coordinates of the atoms in the optimized geometry of formamide at the MP2/aug-cc-pVDZ level of theory. All units are in Bohr.

Atom	x	y	z
O	2.4676097598	-2.0975033086	0.0000000000
N	-1.3241618777	0.0239410394	0.0000000000
C	1.2568931923	-0.1169005069	0.0000000000
H	2.1680762983	1.7734705335	0.0000000000
H	-2.3485379734	-1.5920037050	0.0000000000
H	-2.2198793994	1.7089959478	0.0000000000

Table D.4 – Parameters for the BEB model for formamide obtained through a HF/aug-cc-pVDZ calculation at the optimized geometry. All orbitals are doubly occupied. Energies are in Hartree.

Orbital	B_i	U_i
1a'	-20.5429	29.19935638
2a'	-15.6081	22.11926685
3a'	-11.3728	16.03099351
4a'	-1.3827	2.59903961
5a'	-1.2207	2.06427064
6a'	-0.8536	1.64350407
7a'	-0.7503	1.39098231
8a'	-0.6744	1.77459428
9a'	-0.6084	2.03621598
1a''	-0.5679	1.52708963
10a'	-0.4375	2.17495972
11a''	-0.4212	1.85650228

Methane:

Table D.5 – Parameters for the BEB model for methane obtained through a HF/aug-cc-pVQZ according to the T_d point group (note that the orbital $1t_2$ is triply-degenerated). Energies are in Hartree.

Orbital	Occupancy	B_i	U_i
$1a_1$	2	-11.2026	16.01910331
$2a_1$	2	-0.9454	1.21522962
$1t_2$	6	-0.5466	0.95733691